ULSAN NATIONAL INSTITUTE OF
SCIENCE AND TECHNOLOGY

Doctoral Thesis

Ruthenium oxide nanocluster as a 4-in-1 electrocatalyst for hydrogen and oxygen electrochemistry

Han-Saem Park

Department of Energy Engineering

Graduate School of UNIST

2018

Ruthenium oxide nanocluster as a 4-in-1 electrocatalyst for hydrogen and oxygen electrochemistry

Han-Seam Park

Department of Energy Engineering

Graduate School of UNIST

Ruthenium oxide nanocluster as a 4-in-1 electrocatalyst for hydrogen and oxygen electrochemistry

A thesis/dissertation
submitted to the Graduate School of UNIST
in partial fulfillment of the
requirements for the degree of
Doctor of Philosophy

Han-Saem Park

12. 15. 2017

Approved by

Advisor
Hyun-Kon Song

ULSAN NATIONAL INSTITUTE OF
SCIENCE AND TECHNOLOGY

Ruthenium oxide nanocluster as a 4-in-1 electrocatalyst for hydrogen and oxygen electrochemistry

Han-Saem Park

This certifies that the thesis/dissertation of Han-Saem Park is approved.

12. 15. 2017

Advisor: Hyun-Kon Song

Jong-Beom Baek: Thesis Committee Member #1

Young S Kim.

Youngsik Kim: Thesis Committee Member #2

Sang Hoon Joo

Sang Hoon Joo: Thesis Committee Member #3

Shin Kyoung Hee

Kyoung-Hee Shin: Thesis Committee Member #4

Abstract

Ruthenium oxide (RuO_2) is the best oxygen evolution reaction (OER) electrocatalyst. Herein, we demonstrated that RuO_2 can be also efficiently used as an oxygen reduction reaction (ORR) electrocatalyst, thereby serving as a bifunctional material for rechargeable Zn–air batteries. We found two forms of RuO_2 (i.e. hydrous and anhydrous, respectively *h*-RuO_2 and *ah*-RuO_2) to show different ORR and OER electrocatalytic characteristics. Thus, *h*-RuO_2 required large ORR overpotentials, although it completed the ORR via a 4e process. In contrast, *h*-RuO_2 triggered the OER at lower overpotentials at the expense of showing very unstable electrocatalytic activity. To capitalize on the advantages of *h*-RuO_2 while improving its drawbacks, we designed a unique structure (RuO_2@C) where *h*-RuO_2 nanoparticles were embedded in a carbon matrix. A double hydrophilic block copolymer-templated ruthenium precursor was transformed into RuO_2 nanoparticles upon formation of the carbon matrix via annealing. The carbon matrix allowed for overcoming the limitations of *h*-RuO_2 by improving its poor conductivity and protecting the catalyst from dissolution during OER. The bifunctional RuO_2@C catalyst demonstrated a very low potential gap ($\Delta E_{\mathrm{OER\text{-}ORR}}$ = ca. 1.0 V) at 20 mA cm^{-2}. The Zn||RuO_2@C cell showed an excellent stability (i.e. no overpotential was observed after more than 40 h).

Additionally, partially hydrous RuO_2 nanocluster embedded in carbon matrix (*x*-RuO_2@C with *x* = hydration degree = *0.27* or *0.27*@C) was presented as a bifunctional catalyst of hydrogen evolution reaction (HER) and oxygen evolution reaction (OER) for water splitting. Symmetric water electrolyzers based on *0.27*-RuO_2@C for both electrodes showed smaller potential gaps between HER and OER at pH 0, pH 14 and even pH 7 than conventional asymmetric electrolyzers based on two different catalysts (Pt/C || Ir/C) that have been known as the best catalysts for HER and OER respectively. Moreover, *0.27*-RuO_2@C showed another bifunctional electroactivity for fuel cell electrochemistry including hydrogen oxidation reaction (HOR) and oxygen reduction reaction (ORR) that are backward reactions of HER and OER respectively. Pt-level HOR electroactivity was obtained while its ORR activity was inferior to that of Pt with 200 mV higher overpotential required. The tetra-functionality of *0.27*-RuO_2@C issued the possibility of single-catalyst regenerative fuel cells.

Contents

List of figures

Figure 1.9. Schematic representation of the structure and operation principle of a metal–air battery and the liquid-gas-solid (catalyst) interface in the air electrode.

Figure 1.10. Schematic of an AEMFC as compared to a PEMFC.

Figure 1.11. Schematic of the operating principle of an alkaline and PEM water electrolysis cell.

Figure 1.12. Schematic representation of an AEM-URFC as an energy storage device for vehicular and grid applications. The AEM-URFC stores renewable energy as H_2 while in electrolyzer mode and then uses that H_2 to produce electric energy on-demand when in fuel cell mode.

Figure 2.1. RuO_2@C nanoclusters. (**a**) Schematic. (**b** and **c**) TEM images.

Figure 2.2. Scanning transmission electron microscopy (STEM) image, energy-dispersive X-ray spectroscopy (EDS) mapping of Ru, O and C and line mapping.

Figure 2.3. XRD patterns. (a) RuO_2@PEO-*b*-PAA. **(b** to **f)** RuO_2@C obtained after annealing RuO_2@PEO-*b*-PAA. The annealing temperatures were indicated. **(g)** *h*-RuO_2 = hydrous RuO_2 (x = high in $RuO_2{\cdot}xH_2O$). **(h)** *x*-RuO_2 = *h*-RuO_2 thermally treated at 400 °C. **(i)** *ah*-RuO_2 = anhydrous RuO_2 (x approaching 0 in $RuO_2{\cdot}xH_2O$). Note the hkl number in the bracket in represent the peak matching to *ah*-RuO_2.

Figure 2.4. X-ray photoelectron spectra. Abscissa = binding energy (eV), ordinate = intensity in arbitrary unit. (**a** and **b**) O1s **(a)** and Ru3d + C1s **(b)** spectra of RuO_2@PEO-*b*-PAA after drying. (**c** and **d**) O1s **(c)** and Ru3d + C1s **(d)** spectra of RuO_2@C obtained by annealing RuO_2@PEO-*b*-PAA at 400 °C. 3 component spectra were used for deconvoluting O1s spectra: lattice oxygen (O^{2-}) at 530.4 eV; hydroxyl group (OH^-) at 531.2 eV; and surface-bound water (H_2O) at 532.5 eV. 6 component spectra were used for deconvoluting Ru3d and C1s spectra: Ru (IV) indicating RuO_2 at 281.0 and 285.5 eV; Ru(III) of hydrous Ru(III)-OH at 281.7 and 286.4 eV; C 1s at 284.6 and 288.5 eV. (**e** and **f**) O1s **(e)** and Ru3d + C1s **(f)** spectra of RuO_2@PEO-*b*-PAA, RuO_2@C, *ah*-RuO_2, *h*-RuO_2 and *x*-RuO_2.

Figure 2.5. Hydration degree (*x*). The x values of *ah*-RuO_2 and *h*-RuO_2 were assumed to be

0.0 and 1.0, respectively. The peak area ratios of OH^- to O^{2-} or Ru^{3+} to Ru^{4+} was used as a measure of the hydration degree. The x values of other ruthenium oxide samples were estimated from the ratios by interpolating the pre-fixed two points of the XPS peak ratio versus x.

Figure 2.6. ORR in O_2-saturated 0.1 M KOH (aq). (**a**) ORR polarization curves at 1600 rpm and 10 mV s^{-1}. (**b**) Electron transfer number (n). (**c**) Tafel plots. Mass-transfer-corrected currents (i_K) were used. Tafel slopes (b) were indicated in mV dec^{-1}. (**d**) Chronoamperometric stability of ORR at +0.4 V_{RHE}. Initial currents were indicated next to catalyst names.

Figure 2.7. ORR in O_2-saturated 0.1 M KOH (aq). (**a**) ORR polarization curves at 1600 rpm and 10 mV s^{-1}. (**b**) Electron transfer number (n). (c) Tafel plots. Mass-transfer-corrected currents (i_K) were used. Tafel slopes (b) were indicated in mV dec^{-1}.

Figure 2.8. (a) ORR polarization curves of RuO_2@C/CB at various rotating speeds. **(b)** Koutecky-Levich plots of ORR on RuO_2@C/CB at various potentials. Dashed lines indicated the lines for two and four electron transfer cases (n = 2 and 4). The data for the dashed lines were calculated by Koutecky-Levich equation with the following values of parameters: bulk concentration of oxygen (C_O*) = 1.21 mol m^{-3}, diffusivity of oxygen (D_O) = 1.87×10^{-9} $m^2\cdot s^{-1}$ and kinematic viscosity (v) = 1×10^{-6} m^2 s^{-1}.

Figure 2.9. OER in N_2-saturated 0.1 M KOH (aq). (**a**) OER polarization curves at 1600 rpm in the first potential sweep cycles at 10 mV s^{-1}. (**b**) OER current retention at 1.83 V_{RHE} during repeated cyclic voltammograms. (**c**) Chronoamperometric stability of OER at 1.73 V_{RHE} for 60 min in 0.1 M KOH. Initial currents were indicated next to catalyst names. (**d**) Chronopotentiometric stability of OER at 5 mA cm^{-2} for 40 h.

Figure 2.10. OER in N_2-saturated 0.1 M KOH (aq). OER polarization curves at 1600 rpm in the first potential sweep cycles at 10 mV s^{-1}.

Figure 2.11. IR-compensated OER polarization at 10 mV s^{-1} on 1600 rpm. (**a** to **c**) 0.1 M KOH with various percentages of IR compensation f. (**d**) 1 M KOH at f = 0 %. The potential shift corrected by the IR compensation factor f affected the current values at a fixed potential and the onset potential seriously. Therefore, we should use the IR compensation function carefully and indicate the value of f.

Figure 2.12. OER stability. (**a** to **d**) TEM images showing morphological changes of catalysts between before and after OER at 1.73 V_{RHE} for 1 h in 0.1 M KOH (aq).

Figure 2.13. ORR and OER in 0.1 M KOH. The overall polarization curves of ORR and OER.

Figure 2.14. Zn-air battery cells. (**a**) The home-made Zn-air cell. Geometric area of air electrode = 2.2 cm^2. (**b**) The ORR and OER potentials (E_{ORR} or E_{OER} in the left panel) and the potential gaps between ORR and OER ($\Delta E_{OER\text{-}ORR}$) calculated from E_{ORR} and E_{OER} as a function of current. Data were taken from Figure 4a and b. (**c**) Cell potentials during discharge and charge. Refer to Figure 4c and d for its full potential profiles. (**d**) Comparison of $\Delta E_{OER\text{-}ORR}$ between RuO_2@C in this work and other electrocatalysts in other works. The details were given in Table S2. The cells were categorized to groups in terms of fuels. 20 % and 100 % of molecular oxygen were used for Zn-air cells and Zn-O_2 cells, respectively.

Figure 2.15. Zn-air batteries. 20 wt. % carbon black was used for RuO_2@C. Pt loading of Pt/C was 20 wt. %. (**a**) Discharge rate capability at 20 mA cm^{-2} charge. ORR proceeds on air electrodes. Currents used for discharge were indicated in mA (geometric electrode area = 2.8 cm^2). (**b**) Charge rate capability at 20 mA cm^{-2} discharge. OER proceeds on air electrodes. Currents used for charge were indicated in mA (geometric electrode area = 2.8 cm^2). (**c** and **d**) Galvanostatic charge/discharge cycles at 20 mA cm^{-2}.

Figure 2.16. Galvanostatic charge/discharge cycles at 20 mA cm^{-2} in O_2 atmosphere at 1 atm.

Figure 3.1. Regenerative fuel cells for hydrogen economy. Hydrogen is produced in the water splitting mode powered by renewable energy such as solar cells. The hydrogen is used to generate electricity in the fuel cell mode. The fuel cell mode is operated by the backward reactions of the water splitting mode.

Figure 3.2. Partially hydrous ruthenium oxide embedded in carbon (*x*-RuO_2@C). (**a** to **c**) TEM images: a = *x*-RuO_2@C; b = anhydrous RuO_2 (*ah*-RuO_2); c = hydrous RuO_2 (*h*-RuO_2). (**d**) Relative hydration number of RuO_2-based catalysts. (**e**) XRD patterns of *x*-, *ah*- and *h*-RuO_2.

solution (PBS) at pH 7. HER (**a**) and OER (**b**) over potentials of this work in comparison with reported multifunctional catalysts.

Figure 3.10. HER Durability test of *0.27*-RuO$_2$@C. Catalysts were polarized repeatedly from 0.2 V$_{RHE}$ to -0.2 V$_{RHE}$ in 1 N KOH (aq). The potential was swept in 50 mV s^{-1}. Polarization curves at the 1st, 1000th, 1500th and 2000th cycle were selectively demonstrated.

Figure 3.11. In-neutral-media OER polarization comparison of *0.27*-RuO$_2$@C with reported works. Phosphate buffer solution (PBS) at pH7 was used for all electrodes. Data for polarization curves of n-Co$_2$P and N, S co-doped graphitic sheets were read from the following references, respectively: Nano Lett. 2017, 17, 578 and Adv. Mater. 2017, 1604942.

Figure 3.12. Symmetric water electrolyzer. The catalyst was loaded on nickel electrodes in 1 cm^2. (**a**) Overpotential gap between HER and OER ($\Delta E_{OER-HER}$) at 10 or 100 mA cm^{-2}. (**b**) Polarization curves of this work in comparison with reported symmetric electrolyzers. 1 = ref. 74; 2 = ref. 62; 3 = ref. 103; 4 = ref. 96. (**c**) Electrolysis time required to obtain 20 ml H$_2$. Inset photo = the symmetric electrolyzer. (**d**) A miniaturized fuel cell car driven by hydrogen generated by the *0.27*-RuO$_2$@C||*0.27*-RuO$_2$@C electrolyzer powered by a solar cell at 1.83 V. Electrolyte = 1 N KOH for **b** and **c** and 1 N H$_2$SO$_4$ for **d**.

Figure 3.13. Over potentials of HER and OER at ± 10 and ± 100 mA cm^{-2}. Three different electrolytes were used: (**a**) 1 N KOH at pH 14 ; (**b**) 1 N H$_2$SO$_4$ at pH 0; (**c**) and 1 N phosphate buffer solution (PBS) at pH 7. (**d**) Overpotential gap between HER and OER ($\Delta E_{OER-HER}$) at 10 or 100 mA cm^{-2}. 20 wt. % carbon black was used for ruthenium-oxide-based catalysts. ***h*** = *h*-RuO$_2$; ***ah*** = *ah*-RuO$_2$; ***0.27*@C** = *0.27*-RuO$_2$@C.

Figure 3.14. Photograph of water splitting cells connected with commercial batteries. *0.27*-RuO$_2$@C loaded Ni foams used in 1 cm^2 as anode and cathode at 1 N KOH electrolyte. Electrolyzers connected with one (**a**) and two (**b**) 1.5 V commercial AA batteries in series

Figure 3.15. Stability test of water splitting in 1 N KOH by a beaker-type water electrolyzer. *0.27*-RuO$_2$@C-loaded Ni foams in 1 cm^2 were used as both electrodes. Small potential fluctuation was caused by atmospheric temperature change (e.g. day and night). Internal resistances (iR) were not corrected.

Figure 3.16. Alkaline anion exchange membrane water electrolyzers (AEMWE). 1.0 mg cm^{-2} of *0.27*-RuO$_2$@C was loaded on both electrodes. 0.5 N KOH (aq) was used as electrolyte. Cells were operated at room temperature. (**a**) AEMWE. (**b**) Potentiodynamic operation on a potential sweep at 20 mV s^{-1}. (**c**) Potentiostatic operation at 1.6 V for 10 h. (**d**) Electrochemical impedance spectra obtained before and after the previous operation for 10 h. Frequencies varied from 30 kHz to 30 mHz.

Figure 3.17. HOR and ORR polarization. The plots in the left and right columns are for HOR and ORR, respectively. Two different electrolytes were used: 0.1 N KOH at pH 13 (**a** and **b**); 0.1 N HClO$_4$ at pH 1 (**c** and **d**). Rotating disk electrodes of glassy carbon in 0.1256 cm^2 were used at 1600 rpm. 20 wt. % carbon black was used for ruthenium-oxide-based catalysts. ***h*** = *h*-RuO$_2$; ***nh*** = *nh*-RuO$_2$; ***0.27*@C** = 0.27-RuO$_2$@C.

List of tables

Nomenclature

AEMFC	anion exchange membrane fuel cell
AEMFC	anion exchange membrane fuel cell
AEMWE	anion exchange membrane water electrolyzer
***ah*-RuO$_2$**	anhydrous RuO2
b	Tafel slope
C_O*	bulk concentration of oxygen
D_O	diffusivity of oxygen
$E_{1/2}$ (or $E_{L/2}$)	half-wave potential
ECSA	electrochemical active surface area
E^o	standard reduction potential
f	percentage of compensation
FCEV	fuel cell electric vehicle
GC	glassy carbon
HER	hydrogen evolution reaction
HOR	hydrogen oxidation reaction
***h*-RuO$_2$**	hydrous RuO2
i	current density
i_0	exchange current density
i_d	disk current
i_K	mass-transfer-corrected currents
i_r	ring current
i_r	limiting current
Ir/C	iridium on carbon black
N	collection efficiency
OER	oxygen evolution reaction
ORR	oxygen reduction reaction
PBS	phosphate buffer solution
PEMFC	proton exchange (or polymer electrolyte) membrane fuel cell
PEMWE	proton exchange membrane water electrolyzer
PEO-*b*-PAA	PEO$_{5000}$-*b*-PAA$_{6700}$ where the numbers indicate molecular weights of each block
Pt/C	platinum on carbon black
R_c	resistance for correction
RFC	regenerative fuel cell
RRDE	Rotating Ring Disk Electrode
R_u	uncompensated resistance between working and reference electrodes
RuO2	ruthenium oxide
SEM	scanning electron microscope
TEM	transmission electron microscopy

U^o	Equilibrium potential
URFC	unitized regenerative fuel cell
V_{RHE}	V versus RHE
XPS	X-ray photoelectron spectroscopy
XRD	X-ray diffractometer
x-RuO$_2$	degree of hydration (x) of RuO2
#@C	RuO$_2$@C with hydration degree indicated by #
ΔE	potential gap
$\Delta E_{\pm 10}$ or $\Delta E_{\pm 100}$	overpotential gap between HER and OER required to extract 10 or 100 mA cm^{-2}
$\Delta E_{OER\text{-}ORR}$	potential difference between charge and discharge
Greek symbols	
η	overpotential
v	kinematic viscosity

Chapter 1 – Introduction

1.1. Needs for research related to hydrogen and oxygen

Due to the rising the environmental problems (i.e. global warming, carbon dioxide and fine dust problems), research direction is headed for clean energy such as Li-ion batteries, metal-air batteries, water splitting and fuel-cells. Among these energy resources, existing Li-ion rechargeable batteries are faced with limitation of energy density to apply electric vehicles and long charging time problems. While metal-air batteries (i.e. lithium-oxygen, zinc-air, magnesium-air and aluminum-air batteries) and fuel-cells have higher energy densities than other commercial batteries (**Figure 1.1**).[1] It is known that the theoretical energy density of gasoline, Li-ion batteries and fuel cells are around 13,000 Wh Kg^{-1}, 200 Wh Kg^{-1} and 33,000 Wh Kg^{-1}, respectively.[1-3] Moreover fuel cells have been regarded as the most effective clean energy source.

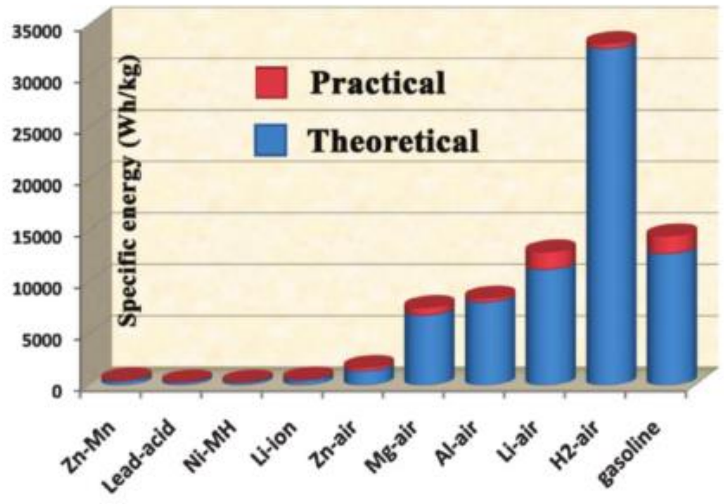

Figure 1.1. Comparison of the gravimetric energy density of some representative types of primary/rechargeable batteries, metal–air batteries, H_2–air fuel cell and gasoline. The theoretical values are calculated on the basis of thermodynamics of active materials.

On the other hand, Hydrogen production made by fossil fuels is produced as a byproduct such as carbon mono- and di-oxide. Fuel cell catalyst (i.e. platinum (Pt) which is the best oxygen reduction reaction (ORR) catalyst) suffers from a high sensitivity CO poisoning because CO adsorbs strongly on the active Pt sites, therefore it hinders the reaction of the fuel. So, hydrogen evolution reaction (HER) by the water electrolysis has attracted much attention worldwide. Although water electrolysis to produce hydrogen has advantage of producing extremely pure hydrogen, hydrogen fuel produced by water electrolysis is still high cost with low efficiencies.[4]

Moreover, Water-splitting from renewable energy sources such as solar cells and wind power is considered as the most promising pathway for carbon free, environmental and sustainable hydrogen production (**Figure 1.2**).[5] However, it is difficult to use it efficiently since the overpotential of water splitting is still high. The theoretical potential is 0 V_{RHE} for HER, and 1.23 V_{RHE} for oxygen evolution reaction (OER). However, extra energy is needed to overcome the overpotential caused by the activation energy barrier to kick start the initial reaction. So many scientists have been researching to reduce the overpotential of HER and OER with various materials at acid, alkaline as well as neutral electrolyte. **Figure 1.3** shows the summarized non-noble metal-based carbon electrocatalysts of a recent study on HER catalysts.[5]

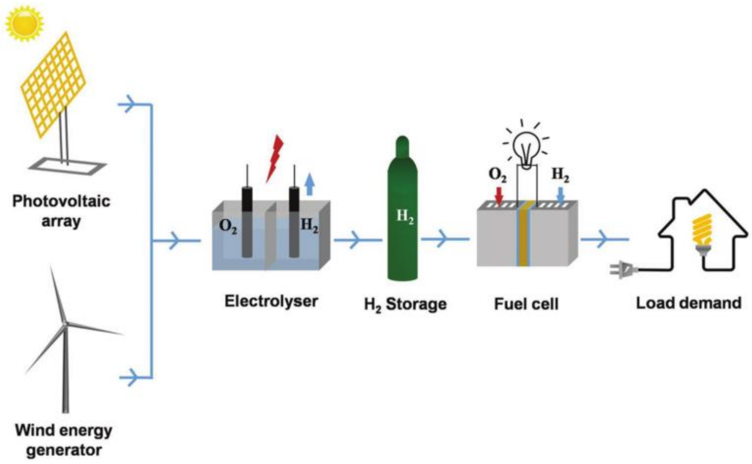

Figure 1.2. The overall concept of a hydrogen renewable energy system for distributed power generation.

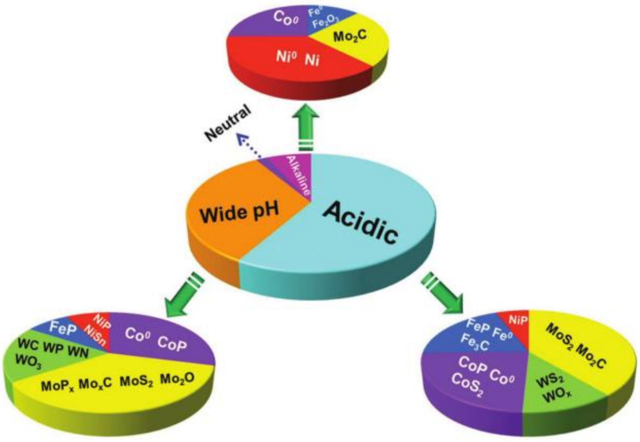

Figure 1.3. Chart for the distributions of summarized non-noble metal-based carbon electrocatalysts for HER under different pH ranges, and the distributions of different non-noble metal-based carbon composites corresponding to the pH conditions (acidic, alkaline and wide pH medium).

1.2. Hydrogen and Oxygen related energy conversion reactions

1.2.1 Principles of hydrogen and oxygen related reactions

Hydrogen and oxygen related electrochemical reactions are divided into hydrogen evolution reaction (HER), hydrogen oxidation reaction (HOR), oxygen reduction reaction (ORR) and oxygen evolution reaction (OER) according to the potentials. Namely, hydrogen and oxygen related reactions can be categorized by oxidation or reduction of hydrogen and oxygen molecules. Also, those four reactions can be categorized into two reversible reaction couples which are related to oxygen and hydrogen. Although hydrogen and oxygen reactions are reversible, polarization curve shapes of these reactions are different. **Figure 1.4** demonstrates the reaction equations at acid and polarization curves of those reactions.[6] As shown in figure 1.4, because of the mass transfer, ORR and HOR has limiting current at high overpotentials. On the other hand, HER and OER follow the Butter-Volmer equation even when being high overpotentials.

And mechanisms of these reactions are changed by hydrogen exponent(pH). **Table 1.1** shows electrochemical reaction mechanisms hydrogen and oxygen reactions following the pH. [6]

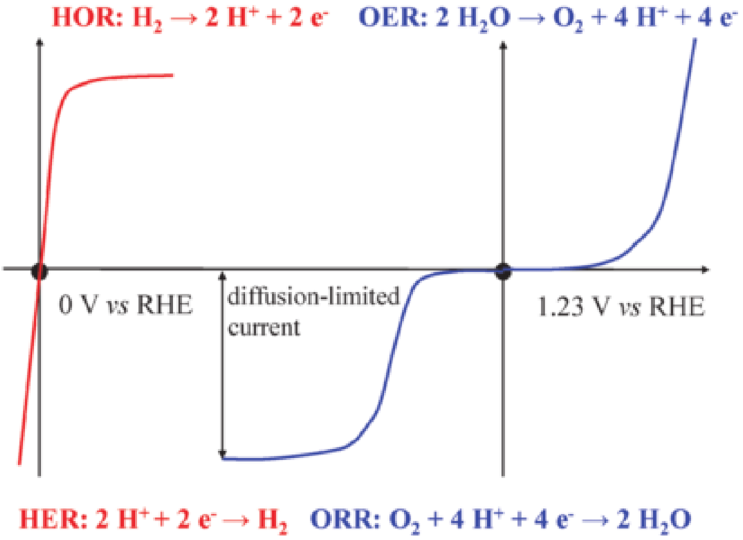

Figure 1.4 The polarization curves for two pairs of the key energy-related electrochemical reactions and their overall reaction equations. Red and blue curves refer to the hydrogen-involving and oxygen-involving reactions, respectively. The lines are not drawn to scale.

Table 1.1. Electrochemical reactions of hydrogen and oxygen related reactions at acid and base electrolytes.

	Acid	Base	Equilibrium potential (U°)
HER	$2H^+ + 2e^- \rightarrow H_2$	$2H_2O + 2e^- \rightarrow H_2 + 2OH^-$	O V vs. RHE
HOR	$H_2 \rightarrow 2H^+ + 2e-$	$H_2 + 2OH^- \rightarrow 2H_2O + 2e^-$	O V vs. RHE
ORR	$O_2 + 4H^+ + 4e^- \rightarrow 2H_2O$	$O_2 + 2H_2O + 4e^- \rightarrow 4OH^-$	1.23 V vs. RHE
OER	$2H_2O \rightarrow O_2 + 4H^+ + 4e^-$	$4OH^- \rightarrow O_2 + 2H_2O + 4e^-$	1.23 V vs. RHE

1.3. Useful notions in hydrogen and oxygen related test

1.3.1 Equilibrium potential

Equilibrium potential of hydrogen and oxygen related reaction is moved by pH value. The potential of the RHE correlates to the pH value:

$E^0 = 0.000 - 0.059 \times pH$

1.3.2 Onset potential

Onset potential indicates the potential at which current starts to rise (a reaction starts taking place) from the baseline in the voltammogram (**Figure 1.5**)[7]. In ORR, the background current (i.e. capacitive current) should be properly removed following process. [8] The current is obtained by measuring the linear voltammetry or cyclic voltammetry under O_2 and N_2 using experimental parameters such as scan rate and rotation rate. Afterward these two values subtract the curve under N_2 from that under O_2. In case of OER a previous method cannot be used because OER measurement is not affecting the kind of purging gases. The precision onset potential of OER can be observed by the Rotating Ring Disk Electrodes (RRDE) technique in N_2-saturated electrolytes.[9] When generated oxygen at the disk moved to the ring by forced convection, oxygen was reduced at the ring held constantly at 0.40 V_{RHE}. **Figure 1.5b** shows that ring currents can be used for onset potential analysis.

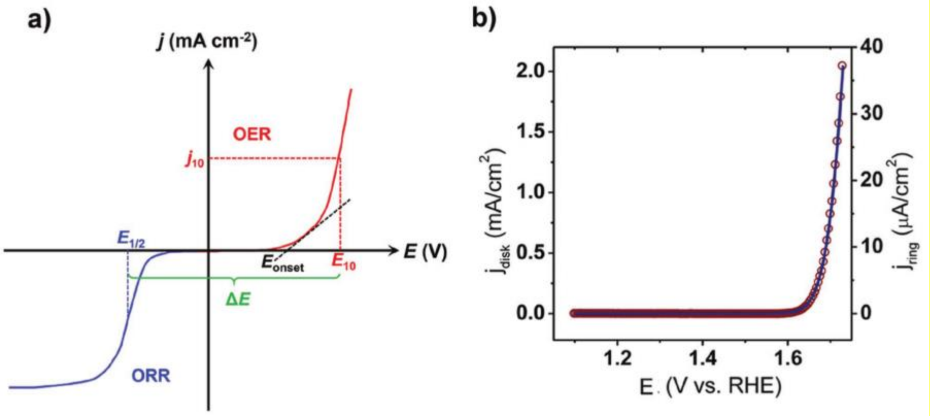

Figure 1.5. (**a**) Polarization curves for ORR and OER. (**b**) Onset potential analysis for OER using RRDE technique.

1.3.3 Current Density

The current density (*i*) is generally normalized by the surface area of the catalysts. The current density is related with production or consumption rate of oxygen or hydrogen. This parameter can be expressed as a crucial indicator on the practical performance of the catalyst.

1.3.4 Tafel Slope

Tafel slopes are obtained from polarization curves. The overpotential (η) is related to the current density (*i*) and its linear region is given by Tafel equation ($\eta = a + b \log(i)$ where *b* is Tafel slope). The Tafel slope indicates the reaction rate and the rate-determining step. When $\eta = 0$, the current density from equation is called exchange current density (i_0) which represents the intrinsic activity of the catalysts under equilibrium states. Therefore, high performance catalyst for hydrogen and oxygen has a high i_0 and a small b value.

1.3.5 Electron Transfer Number (*n*)

ORR has two different mechanisms depending on the catalysts. One is direct four-electron pathway without peroxide formation. The other is two-electron pathway with peroxide formation. Electron transfer number (n) can be calculated by the following equation: $n = 4|i_d|/(|i_d|+ i_r/N)$ from RRDE experiment, where i_d, i_r and N are a disk current, ring current and collection efficiency, respectively. HO_2^- percentage can be calculated by the following equation: $HO_2^-\ \% = 200(i_r / N) / (|i_d| + i_r / N)$.[10]

1.3.6 Potential Gap

There are some unique parameters to evaluate the performance for bifunctional ORR/OER or HER/OER catalysts. Generally, the potential gap (ΔE) between an ORR current density of −3 mA cm^{-2} and an OER current density of 10 mA cm^{-2} for ORR/OER and the potential gap (ΔE) between an HER current density of −10 mA cm^{-2} and an OER current density of 10 mA cm^{-2} for HER/OER is used as the performance evaluation indicators. The potential gap between the ORR half-wave potential ($E_{1/2}$) and OER potential (at 10 mA cm^{-2}) is sometimes used for evaluating the performances between ORR and OER. [11]

1.4 Factors affecting electrochemical reactions

While many catalysts have showed hydrogen and oxygen related energy storages such as metal-air batteries and fuel cells, difficulties still remain to develop a practical hydrogen and oxygen related energy storages with performance better than the existing Li-ion batteries. Based on our current understanding of the existing catalysts (**Figure 1.6**), we believe that the following research directions are important to the development of highly efficient catalysts for hydrogen and oxygen related energy storages.[12]

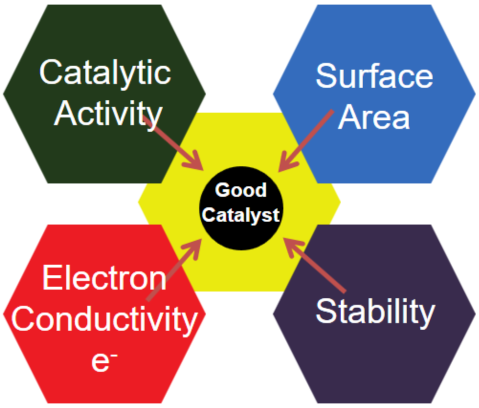

Figure 1.6. Factors that may affect the electrochemical reactions.

1.4.1 Surface area

It is necessary to enlarge the active surface area for the high performance of electronic devices. Electrochemical reaction occurs at the materials surface. Large surface areas supply more electrochemical activities. To increase surface area, nanoscale structures such as mesostructures, nanosheets and nanowires have been focused. Additionally, reasonable design of the interfaces is necessary to control the catalytic activity because both ORR and OER in an air electrode involve three-phases such as liquid, solid and gas. First of all, since the oxygen solubility liquid electrolytes is relatively low, it is critical to optimize hydrophobicity of the electrodes and the surface area of active sites.

1.4.2 Electron conductivity

Highly conductive active materials support facile electron transfer processes for efficient current collection. Insufficient electrical conductivity of catalysts must be improved by adding extra conductive materials like carbon. Furthermore, contacts between catalysts and current collectors (and/or between catalysts and catalyst) must be sufficient to guarantee seamless electron transfer.

1.4.3 Stability

Stable electrocatalysts need to keep their activity over an extended lifetime and to avoid degradation under operation because electro-catalysts may suffer a loss of the electrochemical active surface area (ECSA). A gradual loss of ECSA will lead to efficiency losses of the electrochemical cells. **Figure 1.7** shows degradation mechanisms for electrocataysts (i.e. platinum particles on a carbon support) such as dissolution, Ostwald ripening, agglomeration, particle detachment and carbon corrosion.[13] Therefore, we should design the material design as a way to reduce the degradation of electrocatalysts under operating conditions.

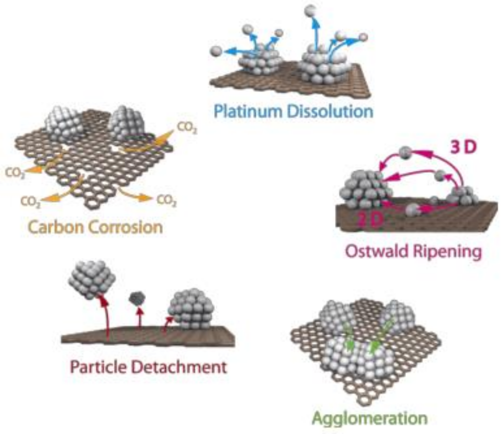

Figure 1.7. Simplified representation of suggested degradation mechanisms for platinum particles on a carbon support in fuel cells.

1.4.4 Catalytic activity of catalysts

As shown before, catalytic activity of catalysts may be influenced critically by the geometric and the electronic structures of catalysts. It is more related with the binding affinity of oxygen and hydrogen on the surface of active sites exactly. Computational quantum chemistry is helpful in predicting the catalytic activity and design of catalyst materials. **Figure 1.8** shows volcano plots regarding ORR, OER and HER. [6, 14-17]

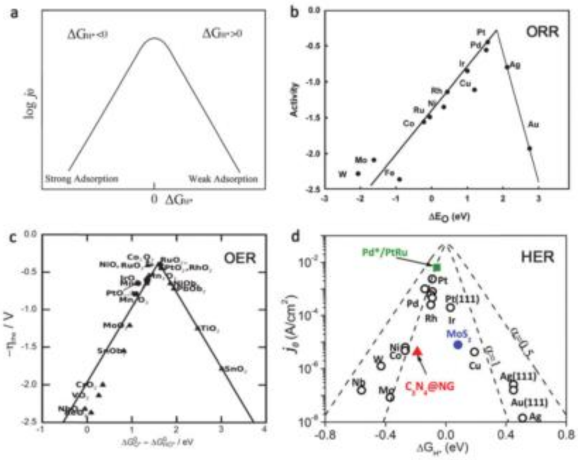

Figure 1.8. Volcano plots for different surfaces. (**a**) Relationship between j_0 and hydrogen adsorption free energy under the assumption of Langmuir adsorption model from ref. 14. (**b**) ORR activity for a range of pure metals plotted against O* adsorption energy from ref. 15 (**c**) Activity trends for OER as a function of ΔG_{O*} - ΔG_{OH*} for rutile and anatase oxides. The activity is expressed by the value of overpotential to achieve a certain value of current density from ref. 16. (**d**) HER j_0 versus hydrogen adsorption free energy for the surfaces of various metals, alloy compounds, and non-metallic materials from ref. 17.

1.5 Utilizations of hydrogen and oxygen related reactions

Depending on how the two reactions are used of the HER, HOR, ORR and OER, the utilization of hydrogen and oxygen related reactions is divided as follows.

1.5.1 ORR/OER – rechargeable metal-air (or O_2) cells

Metal-air batteries have the highest energy density, So it is considered as the most promising systems for portable devices, electrical vehicles, and smart grid applications. Metal-air (or O_2) batteries involve ORR during discharge and OER during charge. Performance of catalysts play a role in determining the overall performance of metal-air batteries, including charge-discharge rate, capacity retention, energy efficiency, and cycling life.[1]

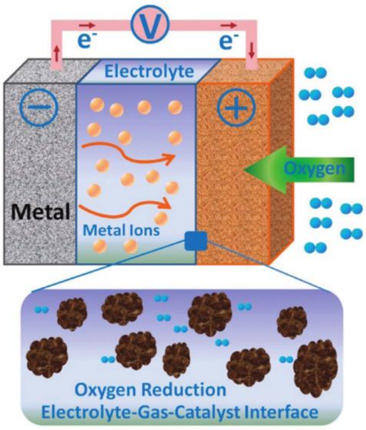

Figure 1.9. Schematic representation of the structure and operation principle of a metal–air battery and the liquid-gas-solid (catalyst) interface in the air electrode.

1.5.2 HOR/ORR: fuel cells (PEMFC, AEMFC)

Fuel cells are considered ideal power sources for fuel cell electric vehicle (FCEV) and stationary applications due to their high energy efficiency and high-power density. Also, advantages of fuel cells are that they produce zero emissions like CO_x and NO_x when using hydrogen as the fuel and air as the oxidant.[18] Fuel cells can be divided into PEMFC (proton exchange (or polymer electrolyte) membrane fuel cell) and AEMFC (anion exchange membrane fuel cell) following the electrolyte used in the electrolysis cells.

Potential of fuel cells drives chemical reactions including HOR and ORR which are take place in the anode and cathode, respectively, to produce electrons and protons. **Figure 1.10** shows schematic of an AEMFC as compared to a PEMFC.[19]

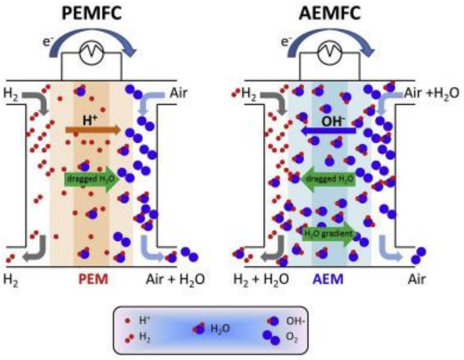

Figure 1.10. Schematic of an AEMFC as compared to a PEMFC.

1.5.3 HER/OER: water electrolyzer (PEMWE, AEMWE)

Water electrolysis is a promising technology for hydrogen production. Because it can produce hydrogen gases without greenhouse gases, if hydrogen is produced by renewable sources like solar and wind power.[20]

Water electrolysis is the decomposition of water into hydrogen and oxygen gas using HER and OER when current flows through the circuit. The reaction happens at 1.23 V ideally, extra energy is generally needed because of overpotentials. Therefore, minimizing the HER and OER overpotentials is the core of the research.

Water electrolysis can be divided into PEMWE (proton exchange membrane water electrolyzer) and AEMWE (anion exchange membrane water electrolyzer) following the electrolyte used in the electrolysis cells. **Figure 1.11** shows schematic of the operating principle of an alkaline and PEM water electrolysis cell.

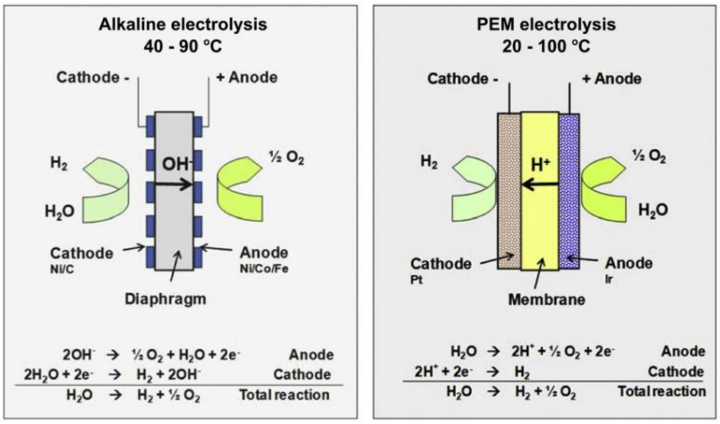

Figure 1.11. Schematic of the operating principle of an alkaline and PEM water electrolysis cell.

1.5.4 HER/OER & HOR/ORR: regenerative fuel cells (RFCs)

The RFC drives four different reactions in total and can divide two categories such as electrolyzer mode and fuel cell mode. When applied to RFCs by using output electricity, it produces hydrogen as electrolyzer mode using the HER and OER, and then produced hydrogen can make the electricity using HOR and ORR in fuel cell mode. **Figure 1.12** shows schematic representation of an AEM-URFC as an energy storage device.[21]

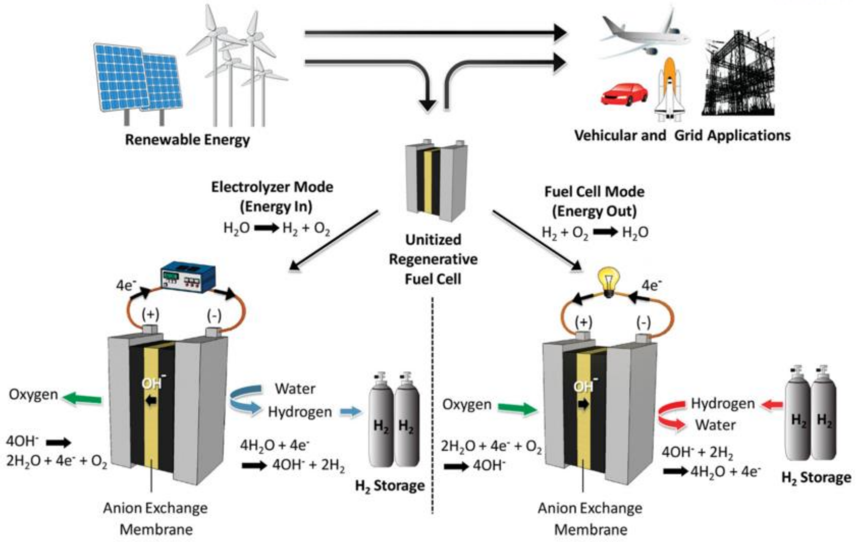

Figure 1.12. Schematic representation of an AEM-URFC as an energy storage device for vehicular and grid applications. The AEM-URFC stores renewable energy as H_2 while in electrolyzer mode and then uses that H_2 to produce electric energy on-demand when in fuel cell mode.

1.6 Scope

In this research, we suggest 4-in-1 catalyst of partially hydrated ruthenium oxide. We have confirmed that the HER, HOR, ORR and OER performance (i.e. onset potentials, stability and electron transfer numbers) of our partially hydrous ruthenium oxides nanocluster embedded in carbon matrix has only a good portion of the completely anhydrous and hydrous counterparts. Also, our partially hydrous ruthenium oxide nanocluster embedded in carbon matrix shows excellent performances at universal pH (pH 0, pH 14 and even pH 7).

Moreover, based on these excellent performances, we evaluated the performance of the water electrolyzer and rechargeable Zn-air (and O_2) batteries.

Although we cannot realize the regenerative fuel cells with 4-in-1 catalyst, it can issue the possibility of single-catalyst regenerative fuel cells.

Chapter 2. Bifunctional hydrous RuO_2 nanocluster electrocatalyst embedded in carbon matrix for efficient and durable operation of rechargeable zinc-air batteries

2.1 Introduction

Demands for high energy densities have growingly extended research interests from Li ion batteries to metal air batteries.[2, 21, 22] Zn as a choice for metal in the metal air batteries benefits from low cost, aqueous electrolytes and safety.[22, 23] There are various challenges that should be overcome before realizing rechargeable Zn-air battery cells, including non-uniform zinc dissolution from anodes, limited solubility of Zn ions in electrolytes and serious overpotential experienced during charge. Developing efficient and stable bifunctional catalysts for air electrodes is one of the most important issues for the rechargeable Zn-air batteries. The efficiency and cyclability of oxygen reduction reaction (ORR) and oxygen evolution reaction (OER) should be guaranteed.[2, 21]

Platinum and ruthenium oxide (RuO_2) have been known to be the best ORR and OER catalyst, respectively.[24, 25] However, they do not efficiently drive the reaction reverse to what they can do the best on. That is to say, the ORR electroactivity of RuO_2 is not as facile as its OER activity.[6] From the bifunctional viewpoint, the *ORR-active* RuO_2 is the best scenario because we are already sure of its superior OER activity. This work was motivated by the studies on supercapacitor applications of RuO_2.[26] It has been reported that hydrous RuO_2 ($x > 0$ in $RuO_2 \cdot xH_2O$ or h-RuO_2) of amorphous characteristics shows higher capacitance than its anhydrous form ($x = 0$ or ah-RuO_2, crystal phase).[27, 28] The higher capacitance is possibly interpreted as the more active interaction between the space charges on surface of the hydrous RuO_2 and the ions of electrolyte even if its values cannot be a direct measure of electroactivity. In electrocatalytic fields, however, there was no consideration for the hydrous form of RuO_2 as electrocatalysts and even no recognition of the hydration-dependent electroactivities. Therefore, it is meaningful to test the null hypothesis that partial or complete hydration of RuO_2 is ineffective in improving electroactivities of ORR and/or OER.

Another problem is met even in case that the null hypothesis is rejected. The *ah*-RuO_2 exhibits high metallic conductivity around 10^4 S cm^{-1} and high crystallinity.[29] However, the *h*-RuO_2 has low electric conductivity at ~1 S cm^{-1} with amorphous characteristics.[29] There is every possibility that the poor electric conductivity of catalyst particles of the hydrous RuO_2 limits electrocatalytic activities. Three conditions are required to achieve high activities of electrocatalyst: (1) facile charge transfer kinetics[30] defined by active sites of catalysts, (2) good accessibility of reactants to the active sites[31] and (3) highly developed electric pathways[32] to them. Coating cathode and/or anode materials with carbon has been widely used as a key strategy to improve electric conduction throughout electrodes.[33-35] Electroactive materials can be easily composited with carbon by reducing carbon precursors in a reductive gas environment at temperatures between higher than the thermal decomposition temperature of the precursors and lower than reduction temperature of the active materials. Therefore, the main concern in making oxide/carbon composites by the thermal method is to prevent the oxides from being reduced. For example, sucrose-coated Fe_2O_3 is converted to carbon-coated Fe_3O_4 at 500 ^oC in argon, with a third of iron atoms being reduced from Fe^{3+} to Fe^{2+}.[36]

Two points are emphasized in our strategy to guarantee bifunctional electroactivities of RuO_2 for ORR and OER simultaneously: (1) partially hydrated RuO_2 as catalysts and (2) carbon coating on the catalyst particles. We tuned electric conduction of the catalyst layers by embedding RuO_2 or more precisely *h*-RuO_2 nanoparticles in a carbon matrix phase (RuO_2@C). The RuO_2@C was synthesized by annealing micelles consisting of ruthenium oxide surrounded by double hydrophilic block copolymers of poly(ethylene oxide)-*block*-poly(acrylic acid) (PEO-*b*-PAA) as a template.[26, 37, 38] During the annealing process, hydrous ruthenium oxide core was crystallized and the shell of PEO-*b*-PAA was converted to a continuous carbon phase surrounding partially hydrous RuO_2. Both ORR and OER electroactivities were significantly improved by the incorporation of *hydrous* RuO_2 into the carbon phase. The Zn-air cells based on

RuO_2@C showed the smallest potential gap between ORR during discharge and OER during charge confirming its improved reversibility, when compared with Pt/C and *ah*-RuO_2 and Zn-air cell data reported in literatures.

2.2 Experimental Method & Materials

2.2.1 RuO_2@C Synthesis

PEO-*b*-PAA (PEO_{5000}-*b*-PAA_{6700} where the numbers indicate molecular weights of each block; Polymer Source), ruthenium (III) chloride hydrate ($RuCl_3 \cdot xH_2O$; Sigma-Aldrich) and hydrazine (N_2H_4; Sigma-Aldrich) and sodium hydroxide (NaOH; Junsei Chemical) were used as received. Hydrous ruthenium oxide nanoparticles templated by double hydrophilic block copolymer shell (*h*-RuO_2@PEO-*b*-PAA) were synthesized as reported previously.[26] Briefly, 25.1 mg PEO-*b*-PAA (equivalent to 0.20 mmol of carboxylic acid groups) was dissolved in 50.0 mL of deionized water under vigorous stirring until the solution was completely transparent. 0.10 mL of 4.0 M NaOH (0.40 mmol, 2 equivalents to carboxylic acid groups in PAA block) and then 17.8 mg (0.10 mmol) $RuCl_3 \cdot xH_2O$ were introduced to the solution. Subsequently, 0.10 mL of 10.0 M hydrazine (1.0 mmol) was added to the resulting suspensions under vigorous stirring. After a few seconds, the solution color became dark cyan. The resulting solution was dialyzed against deionized water using a dialysis membrane (MWCO 12000-14000; SpectraPore) to remove residuals. The prepared *h*-RuO_2@PEO-*b*-PAA solution exhibited fairly high colloidal stability, which lasted more than one year without any precipitation. Dry powder of *h*-RuO_2@PEO-*b*-PAA was obtained by using a rotary evaporator. RuO_2@C was obtained by heating the dried *h*-RuO_2@PEO-*b*-PAA at the rate of 10 ^oC min^{-1} to an annealing temperature and then annealing in air at 400 ^oC for 2 h.

2.2.2 Characterization

The morphology and size of RuO_2@C were investigated by using transmission electron microscopy (TEM; JEOL, JEM-2100F; accelerating voltage at 200 kV with Gatan CCD camera). The functional groups of RuO_2@C annealed at different temperatures were analysed by X-ray photoelectron spectroscopy (XPS; Thermo Fisher, K-alpha). The crystallography of RuO_2 was investigated by high power X-ray diffractometer (XRD; Rigaku, D/MAX 2500V/PC).

2.2.3 Catalyst inks

Catalyst inks were prepared by mixing 4 mg catalyst composite in a mixture of 50 µl of 0.05 % Nafion solution (Sigma-Aldrich) and 450 µl of ethanol by sonication for 30 min. 6 µl of the ink was transferred onto the 4 mm-diameter glassy carbon (GC) disk electrode of Pt/GC ring/disk electrode (ALS) and then dried at ambient temperature. Our RuO_2@C was compared with *ah*-RuO_2 (agglomerates of 30 ~ 50 nm primary particles, Sigma-Aldrich) as the more anhydrous control and *h*-RuO_2 (Alfa Aesar) as the more hydrous control. Both controls were used as received. The catalyst composites were prepared by mixing the catalysts with 20 wt. % Ketjen Black 600 as a conducting agent. Pt/C (20 wt % loading of Pt on carbon black, Alfa Aesar) was also used as the catalyst composite for comparison.

2.2.4 Electrochemistry

The electrocatalytic activity and stability of the catalysts were measured by using rotating ring disk electrode (RRDE; ALS) and potentiostat (Bio-Logic, VMP3). The catalyst-coated RRDE as a working electrode was immersed in a glass cell containing 0.1 M KOH. Hg/HgO (XR400, Radiometer Analytical) and Pt wire were used as reference and counter electrodes, respectively. All the potentials were reported in V_{RHE} (V versus RHE; RHE = reversible hydrogen electrode) in this work even if the potential values were read from potentiostats in $V_{Hg/HgO}$: $V_{RHE} = V_{Hg/HgO} + 0.93$ V in 0.1 M KOH (aq). The ORR polarization voltammograms at 10 mV s^{-1} were obtained in the O_2-saturated electrolyte between +0.2 $V_{Hg/HgO}$ and -0.8 $V_{Hg/HgO}$ at various rotation speed (400, 900, 1600 or 2500 rpm). At the same time, +0.4 $V_{Hg/HgO}$ was applied to the ring electrode of RRDE to detect peroxide formed from the disk electrode by oxidizing the peroxide completely. Pure faradaic currents were reported in this work by subtracting background capacitive currents obtained in N_2-saturated electrolyte from the overall reduction currents from disk electrodes. The collection efficiency (N) was estimated at 0.42 (the same as the theoretical value) in 10 mM potassium ferricyanide ($K_3Fe(CN)_6$) in 0.1 M KOH electrolyte under Ar atmosphere. The number of electrons transfer (n) of ORR was calculated by using: $n = 4 |I_d|/(|I_d|+I_r/N)$ where I_d and I_r are the disk and ring currents, respectively. The OER polarization voltammograms at 10 mV s^{-1} were obtained in the N_2-saturated electrolyte between +0.35 $V_{Hg/HgO}$ and +0.9 $V_{Hg/HgO}$ at 1600 rpm. Mass-transfer-corrected currents (i_K) were used for Tafel plots: $i_K = i\, i_L/(i_L - i)$ with i_L = limiting current.[39]

2.2.5 Zn-air battery

Zn-air cells were constructed in a previously reported configuration[40] based on: Zn plate (Alfa Aesar) as an anode, carbon on nickel mesh (MEET, Korea) as a gas diffusion layer (GDL) of an cathode, microporous membrane (Celgard 3501) as a separator and Ni mesh as current collectors with 6M KOH aqueous electrolyte. 100 μl catalyst ink was loaded on a carbon GDL electrode (geometric area = 2.834 cm^2) and the catalyst-loaded electrode was dried at 80 ^oC for > 1 h. Zn-air cells were galvanostatically discharged and charged at various currents by a potentiostat (Bio-Logic, VMP3).

2.3 Results and Discussion

2.3.1 RuO_2@C nanoclusters as catalyst

Ruthenium precursors templated by PEO-*b*-PAA were converted to RuO_2 nanoparticles (4 to 5 nm) embedded in a continuous carbon matrix phase in RuO_2@C nanoclusters (**Figure 2.1**). Electrostatic interaction between ruthenium precursor cations and the anionic PAA blocks in the double hydrophilic block copolymer PEO-*b*-PAA resulted in forming the RuO_2 spherical nanoparticles. The other hydrophilic PEO blocks decorating the nanoparticle surface and exposed to solution stabilized the nanoparticles in solution without aggregation.

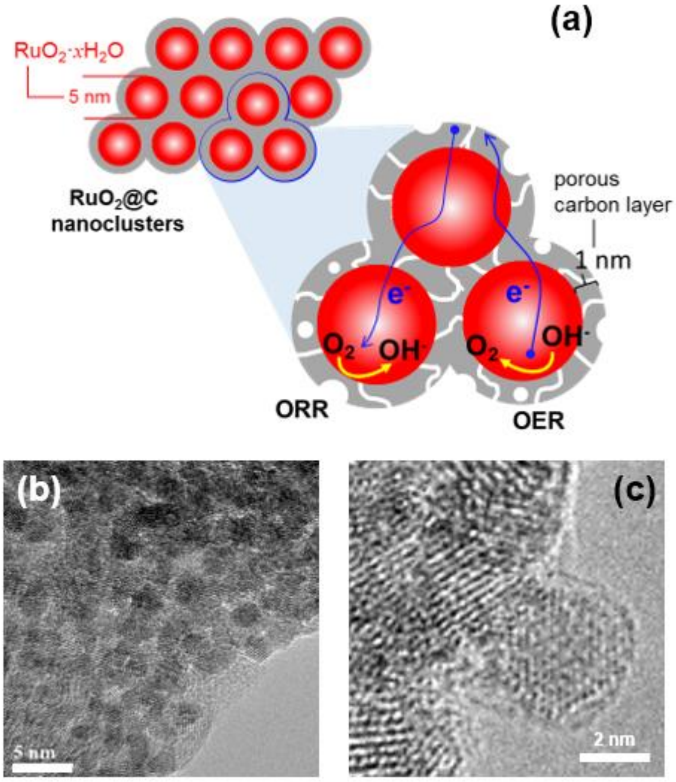

Figure 2.1. RuO_2@C nanoclusters. (**a**) Schematic. (**b** and **c**) TEM images.

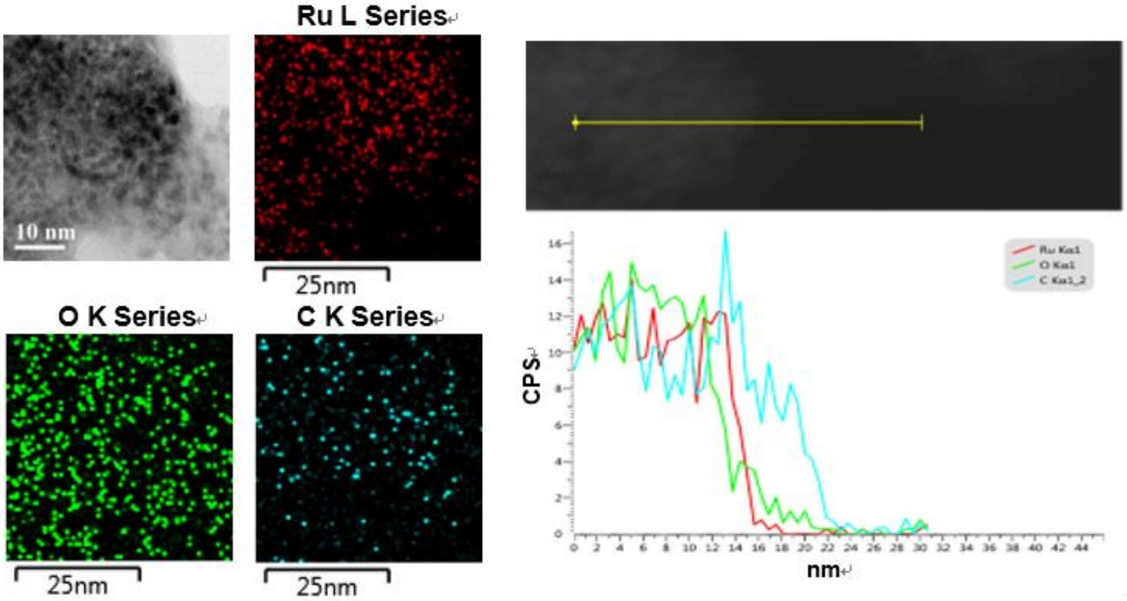

Figure 2.2. Scanning transmission electron microscopy (STEM) image, energy-dispersive X-ray spectroscopy (EDS) mapping of Ru, O and C and line mapping.

RuO_2@C showed the well-defined X-ray diffraction (XRD) patterns of RuO_2 when the annealing temperature was higher than 350 °C (**Figure 2.3a-f**). The amorphous characteristics of hydrous ruthenium oxide in RuO_2@PEO-*b*-PAA decreased with temperature as the oxide became dehydrated with x in $RuO_2 \cdot xH_2O$ decreasing. The same trend was obtained when hydrous RuO_2 (*h*-RuO_2) was thermally treated (**Figure 2.3g and h**). After being annealed at 400 °C, the temperature for preparing RuO_2@C, the *h*-RuO_2 (not identifiable by its characteristic peaks) showed the apparent crystallographic peaks (*x*-RuO_2) of its anhydrous counterpart (*ah*-RuO_2). The crystallite size increased with the annealing temperature: 12 nm at 350 °C < 17 nm at 400 °C (RuO_2@C) < 20 nm at 450 °C. The size of *x*-RuO_2 obtained by heating *h*-RuO_2 at 400 °C was estimated at 23 nm, which is larger than the crystallite size of RuO_2@C obtained by heating RuO_2@PEO-*b*-PAA at 400 °C. The *ah*-RuO_2 was largest in crystallite size at 27 nm.

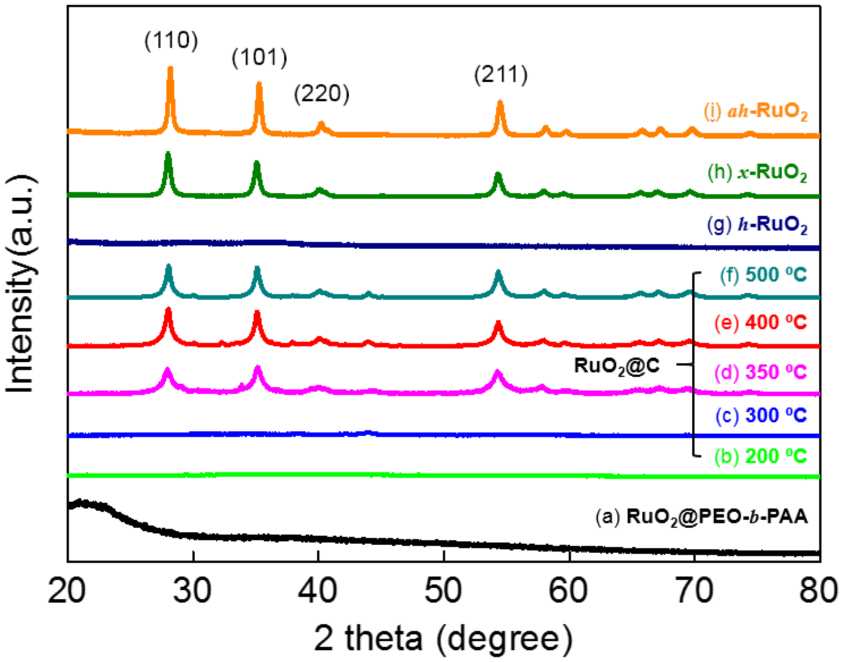

Figure 2.3. XRD patterns. (**a**) RuO_2@PEO-*b*-PAA. (**b** to **f**) RuO_2@C obtained after annealing RuO_2@PEO-*b*-PAA. The annealing temperatures were indicated. (**g**) *h*-RuO_2 = hydrous RuO_2 (x = high in $RuO_2 \cdot xH_2O$). (**h**) *x*-RuO_2 = *h*-RuO_2 thermally treated at 400 °C. (**i**) *ah*-RuO_2 = anhydrous RuO_2 (x approaching 0 in $RuO_2 \cdot xH_2O$). Note the hkl number in the bracket in represent the peak matching to *ah*-RuO_2.

X-ray photoelectron spectra (XPS) confirmed that RuO_2 crystallites in RuO_2@C as well as amorphous RuO_2 in RuO_2@PEO-*b*-PAA are in hydrous forms (**Figure 2.4a-d**). Significant amounts of surface-adsorbed H_2O and OH^- were detected in the O1s spectra of both samples: surface water was dominant in RuO_2@PEO-*b*-PAA while OH^- was dominant in RuO_2@C. In addition to lattice Ru(IV), Ru(III) originating from hydrous Ru(III)-OH was found in the Ru3d spectra of both samples even if the relative amount of Ru(III) to Ru(IV) significantly decreased after the thermal annealing.[41] When compared with the *h*-RuO_2 and the *ah*-RuO_2, our RuO_2@C was intermediate between the two extremes (**Figure 2.4e** and **f**). Its main peak in O1s spectra was found between the surface OH^--characteristic peak of *h*-RuO_2 and lattice O^{2-}-characteristic peak of *ah*-RuO_2. The area ratio of OH^- to O^{2-} or Ru(III) to Ru(IV) of RuO_2@C (1.1 or 1.8) was between those of *ah*-RuO_2 (0.4 or 1.3) and *h*-RuO_2 (2.4 or 2.6). The relative hydration degree (x) of RuO_2@C was estimated at 0.27 (quarter hydrous) by interpolating data of the peak ratio as a measure of hydration with the assumption that the x values of *ah*-RuO_2 and *h*-RuO_2 were assumed to be 0.0 and 1.0 respectively (**Figure 2.5**). The x values of RuO_2@PEO-*b*-PAA and x-RuO_2 were 0.81 (highly hydrated) and 0.08 (closer to anhydrous). Therefore, we view the RuO_2@C as a mixture of *hydrous* and *anhydrous* phases of ruthenium oxide.[42-44] The *anhydrous* characteristics is dominant in bulk properties (e.g., crystallography) but the *hydrous* characteristics is still significant in surface properties (e.g., XPS spectra).

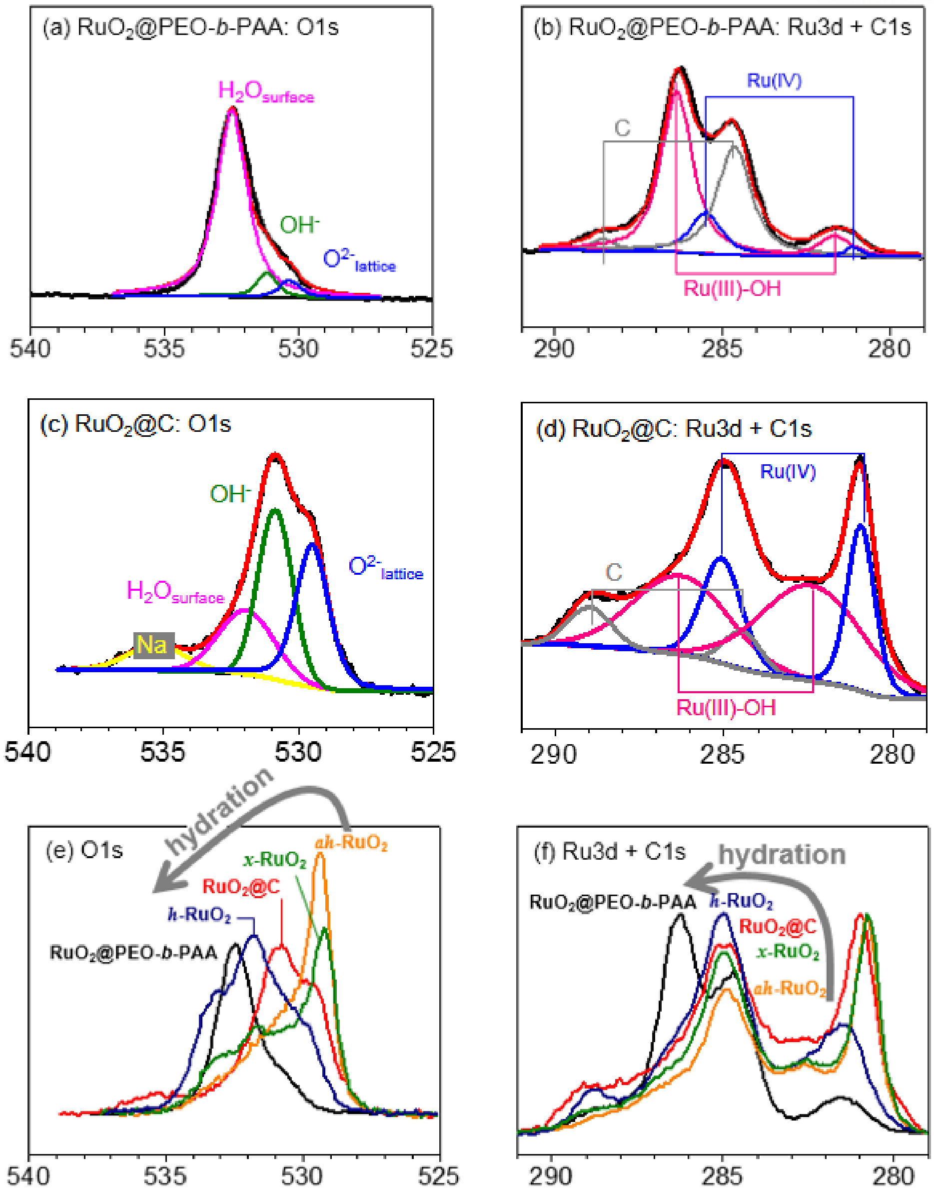

Figure 2.4. X-ray photoelectron spectra. Abscissa = binding energy (eV), ordinate = intensity in arbitrary unit. (**a** and **b**) O1s **(a)** and Ru3d + C1s (**b**) spectra of RuO_2@PEO-*b*-PAA after drying. (**c** and **d**) O1s (**c**) and Ru3d + C1s (**d**) spectra of RuO_2@C obtained by annealing RuO_2@PEO-*b*-PAA at 400 ºC. 3 component spectra were used for deconvoluting O1s spectra: lattice oxygen (O^{2-}) at 530.4 eV; hydroxyl group (OH^-) at 531.2 eV; and surface-bound water (H_2O) at 532.5 eV. 6 component spectra were used for deconvoluting Ru3d and C1s spectra: Ru (IV) indicating RuO_2 at 281.0 and 285.5 eV; Ru(III) of hydrous Ru(III)-OH at 281.7 and 286.4 eV; C 1s at 284.6 and 288.5 eV. (**e** and **f**) O1s **(e)** and Ru3d + C1s (**f**) spectra of RuO_2@PEO-*b*-PAA, RuO_2@C, *ah*-RuO_2, *h*-RuO_2 and *x*-RuO_2.

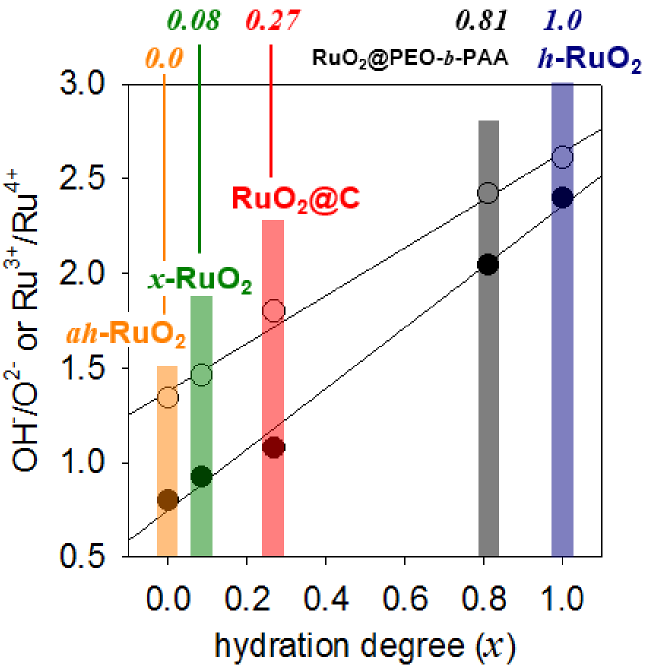

Figure 2.5. Hydration degree (*x*). The x values of *ah*-RuO$_2$ and *h*-RuO$_2$ were assumed to be 0.0 and 1.0, respectively. The peak area ratios of OH$^-$ to O^{2-} or Ru^{3+} to Ru^{4+} was used as a measure of the hydration degree. The *x* values of other ruthenium oxide samples were estimated from the ratios by interpolating the pre-fixed two points of the XPS peak ratio versus *x*.

Several benefits are expected from the structure of RuO$_2$@C nanoclusters when the nanoclusters are used as an electrocatalyst. First, the nanosize of catalysts provides large electrocatalytic surface area per mass, which is realized by the PEO-*b*-PAA template to restrict RuO$_2$ primary particle growth during synthesis. Second, electrons reach catalyst surface effectively through the continuous carbon phase of RuO$_2$@C nanoclusters. Third, non-carbon residues of PEO-*b*-PAA leave void and pore space after carbonization so that reactants are transferrable through the porous carbon matrix readily. Fourth, the carbon matrix surrounding RuO$_2$ possibly suppresses catalyst dissolution.

2.3.2 ORR

The ORR electroactivity of RuO$_2$ has been rarely reported while its OER and hydrogen evolution reaction (HER) have been widely investigated. Poor electroactivities characterized by low ORR currents and high overpotentials were reported with RuO_2 (**Table 2.1**).[21, 45-47] As an example, the potential at a half of the limiting current ($E_{2/L}$ at $i_L/2$) was +0.56 V_{RHE} at -1.2 mA cm^{-2} (cf. +0.9 V_{RHE} at -3 mA cm^{-2} for Pt/C).[45] The high overpotential indicates very sluggish ORR kinetics on RuO_2. More seriously, electron transfer number (n) was estimated at ~2 (4 is preferred for n; discussed below). In this work, interestingly, much higher ORR electroactivities were obtained even from commercially available *ah*-RuO_2 as the control (**Figure 2.6**). Our RuO_2@C nanoclusters in the help of 20 wt. % carbon black as a conducting agent (RuO_2@C in **Figure 2.6** and RuO_2@C+CB in **Figure 2.7**) showed the most facile kinetics ($E_{2/L}$ = +0.7 V_{RHE} at -3 mA cm^{-2}) among ruthenium oxide catalysts for ORR. Without carbon black, the onset potential was seriously shifted in the negative potential direction (RuO_2@C in **Figure 2.7**).

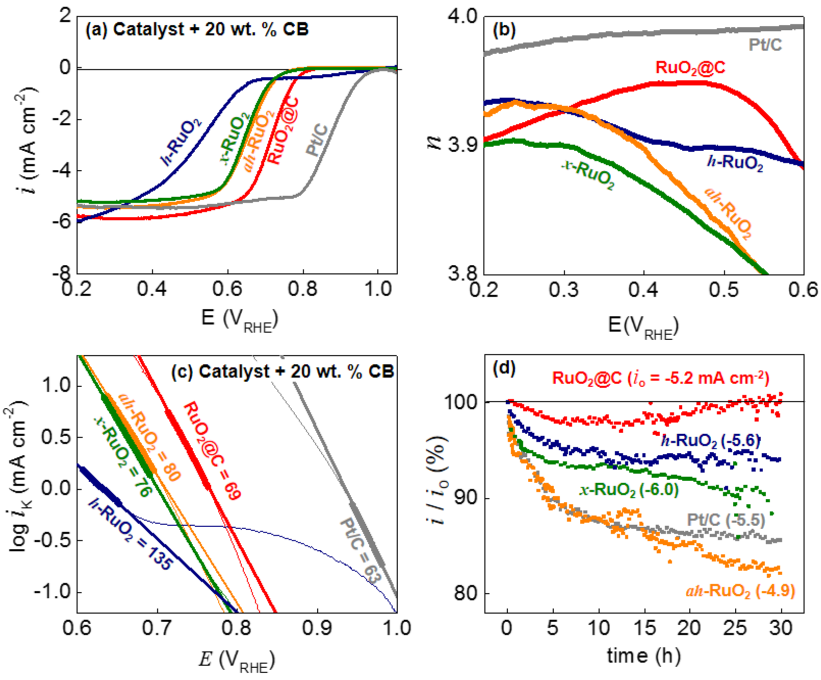

Figure 2.6. ORR in O_2-saturated 0.1 M KOH (aq). (a) ORR polarization curves at 1600 rpm and 10 mV s^{-1}. (b) Electron transfer number (n). (c) Tafel plots. Mass-transfer-corrected currents (i_K) were used. Tafel slopes (b) were indicated in mV dec^{-1}. (d) Chronoamperometric stability of ORR at +0.4 V_{RHE}. Initial currents were indicated next to catalyst names.

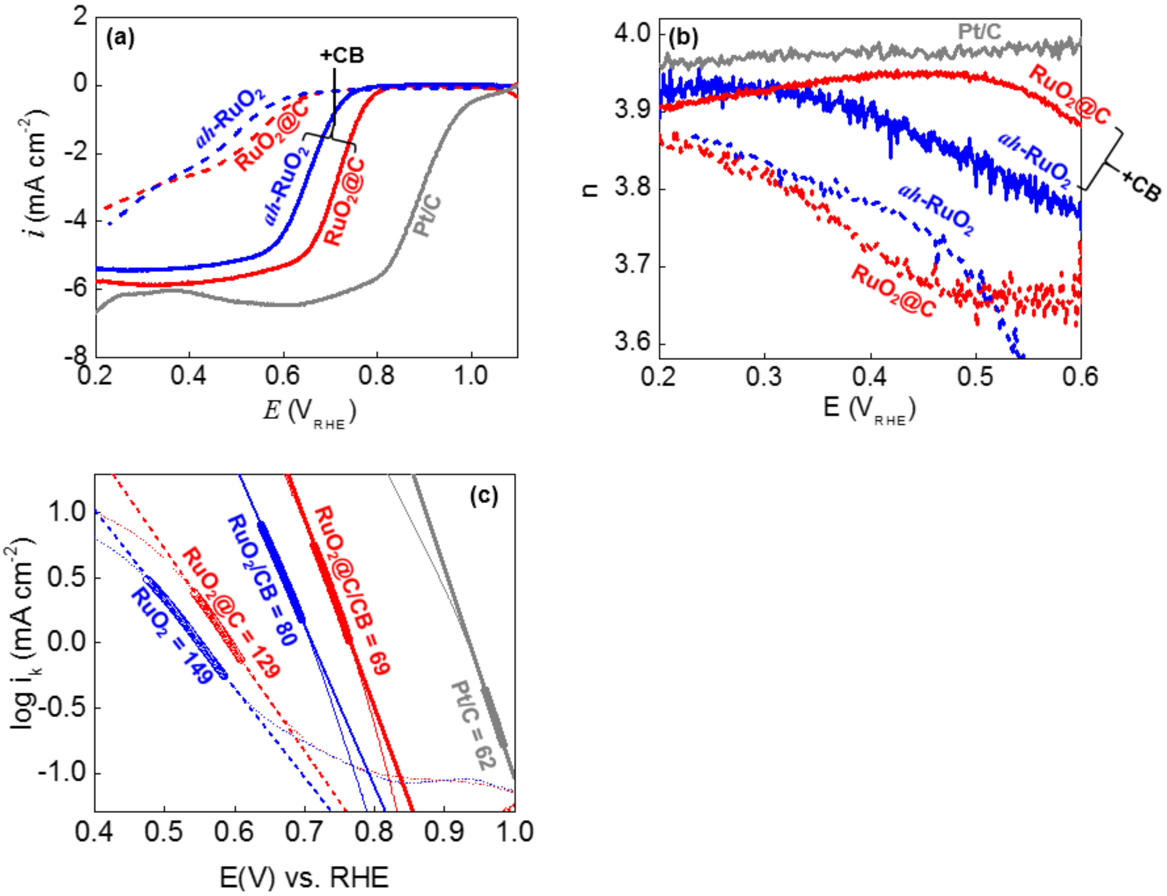

Figure 2.7. ORR in O_2-saturated 0.1 M KOH (aq). (a) ORR polarization curves at 1600 rpm and 10 mV s^{-1}. (b) Electron transfer number (*n*). (c) Tafel plots. Mass-transfer-corrected currents (i_K) were used. Tafel slopes (*b*) were indicated in mV dec^{-1}.

When compared with *h*-RuO_2 and *ah*-RuO_2, our RuO_2@C showed the merits of both forms of RuO_2. In the conductive environments achieved by 20 wt. % carbon black, the anhydrous form (*ah*-RuO_2) was favoured in terms of the onset potential in ORR polarization (**Figure 2.6a**). On the other hand, the hydrous form (*h*-RuO_2) was favored in terms of the number of electron transfer (*n*) especially at low overpotentials (**Figure 2.6b**). The thermal treatment at 400 °C (*x*-RuO_2 in **Figure 2.6**) improved the high overpotential of *h*-RuO_2, shifting the onset potential to that of *ah*-RuO_2. Due to the dehydration by the thermal annealing, however, the *n* values of *x*-RuO_2 decreased and followed those of *ah*-RuO_2. Our RuO_2@C showed the lowest overpotential smaller than the two extreme controls (*h*-RuO_2 and *ah*-RuO_2)

with the *n* values comparable to those of *h*-RuO_2. The hydration degree (x in $RuO_2{\cdot}xH_2O$) of the RuO_2@C is higher than that of *x*-RuO_2 (proved by XRD in **Figure 2.3** and XPS in **Figure 2.4**) so that the high *n* values (> 3.9) are obtained. The *n* values measured from disk and ring currents of RRDE coincided with the values estimated from Koutecky-Levich plots (**Figure 2.8**). The 4e ORR of RuO_2@C indicates the complete reduction of oxygen without producing hydrogen peroxide that is the intermediate 2e ORR product. Tafel slope of RuO_2@C at low overpotentials was 69 mV dec^{-1}, approaching the value of Pt/C (**Figure 2.6c**). Therefore, we conclude that the carbon matrix compensates the poor conductivity of the hydrous RuO_2, preventing ohmic potential shift (low overpotential like conductive *ah*-RuO_2) and enabling efficient utilization of active mass (high *n* value like *h*-RuO_2).

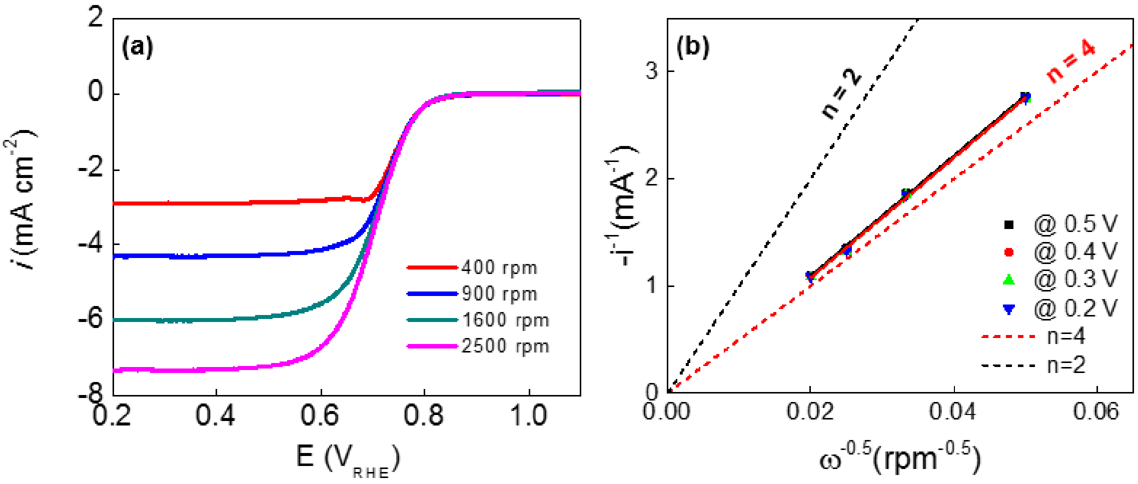

Figure 2.8. (a) ORR polarization curves of RuO_2@C/CB at various rotating speeds. **(b)** Koutecky-Levich plots of ORR on RuO_2@C/CB at various potentials. Dashed lines indicated the lines for two and four electron transfer cases (*n* = 2 and 4). The data for the dashed lines were calculated by Koutecky-Levich equation with the following values of parameters: bulk concentration of oxygen (C_O*) = 1.21 mol m^{-3}, diffusivity of oxygen (D_O) = 1.87×10^{-9} m^2·s^{-1} and kinematic viscosity (v) = 1 × 10^{-6} m^2 s^{-1}.

Chronoamperometric ORR stability was also improved by letting the carbon shell wrap ruthenium oxide nanoparticles in RuO_2@C (**Figure 2.7d**). The currents of *ah*-RuO_2 and Pt/C at

+0.4 V_{RHE} significantly decreased to the 80 % of the initial currents after 30 h. On the contrary, the RuO_2@C showed excellent stability without current decay. Even if Pt/C is the best ORR catalyst from the kinetic standpoint, Pt/C is well known to suffer from its instability caused by Pt aggregation via surface diffusion and dissolution/re-precipitation.

2.3.3 OER

The OER electroactivities were investigated with the full knowledge that ruthenium oxide is one of the best OER catalysts.[16] RuO_2@C, independent of the presence of carbon black, showed remarkably higher current densities than its non-carbon-matrix counterparts (*ah*-RuO_2) with clearly distinguished smaller overpotentials (**Figure 2.9a** and **Figure 2.10**): current at 1.8 V_{RHE} = 54 mA cm^{-2} (RuO_2@C with CB) > 31 mA cm^{-2} (RuO_2@C without CB) > 13 mA cm^{-2} (*ah*-RuO_2 with and without CB) > 5.4 mA cm^{-2} (Pt/C); potential at 10 mA cm^{-2} (E_{10}) = 1.52 V_{RHE} (RuO_2@C with CB) < 1.59 V_{RHE} (RuO_2@C without CB) < 1.75 V_{RHE} (RuO_2 with and without CB) < 1.87 V_{RHE} (Pt/C). The OER currents and the onset potential of our RuO_2@C were, in our best knowledge, superior to any previously reported values of ruthenium oxide (**Table 2.1**). It should be notified that all polarization data of this work were not IR-compensated unless specified. The IR compensation correction seriously affects the OER polarization (not the ORR) so that the percentage of compensation (f) should be selected carefully (**Figure 2.11**): $R_c = f\, R_u$ where R_c = the resistance for correction; R_u = uncompensated resistance between working and reference electrodes. The E_{10} of RuO_2@C significantly decreased from 1.55 V_{RHE} at f = 0 % to 1.48 V_{RHE} at f = 85 % or 1.47 V_{RHE} at f = 100 %. The nanosized catalyst particles well connected to electric and ionic pathways would be partly responsible for the improved OER electroactivity of RuO_2@C. Also, the improvement comes from the hydrated nature of its RuO_2. The OER onset potentials decreased as the catalysts became more hydrous (the inset of **Figure 2.9a**) along *ah*-RuO_2 < *x*-RuO_2 < RuO_2@C < *h*-RuO_2.

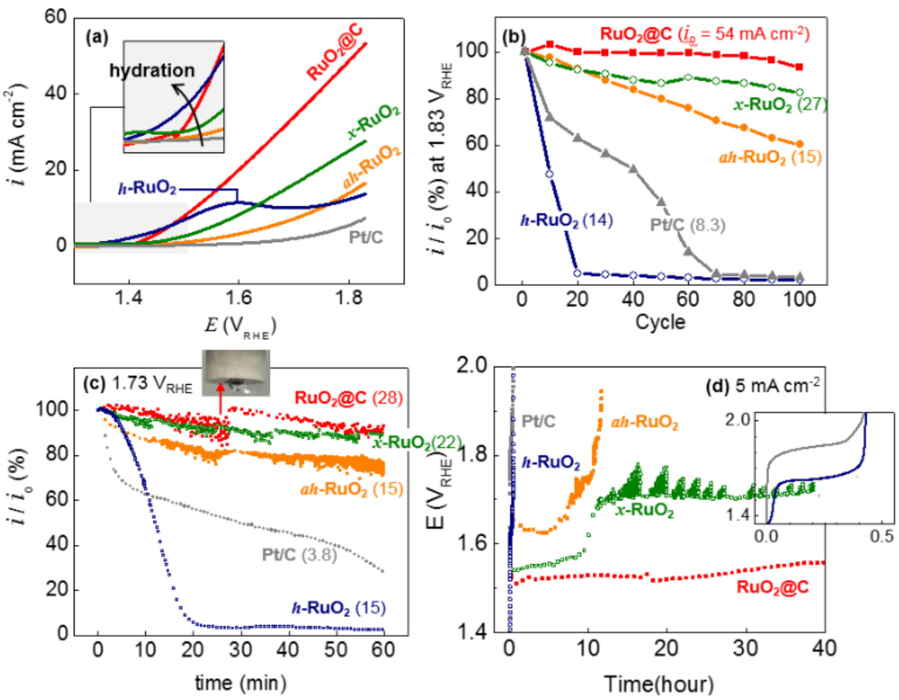

Figure 2.9. OER in N$_2$-saturated 0.1 M KOH (aq). (a) OER polarization curves at 1600 rpm in the first potential sweep cycles at 10 mV s^{-1}. (b) OER current retention at 1.83 V$_{RHE}$ during repeated cyclic voltammograms. (c) Chronoamperometric stability of OER at 1.73 V$_{RHE}$ for 60 min in 0.1 M KOH. Initial currents were indicated next to catalyst names. (d) Chronopotentiometric stability of OER at 5 mA cm^{-2} for 40 h.

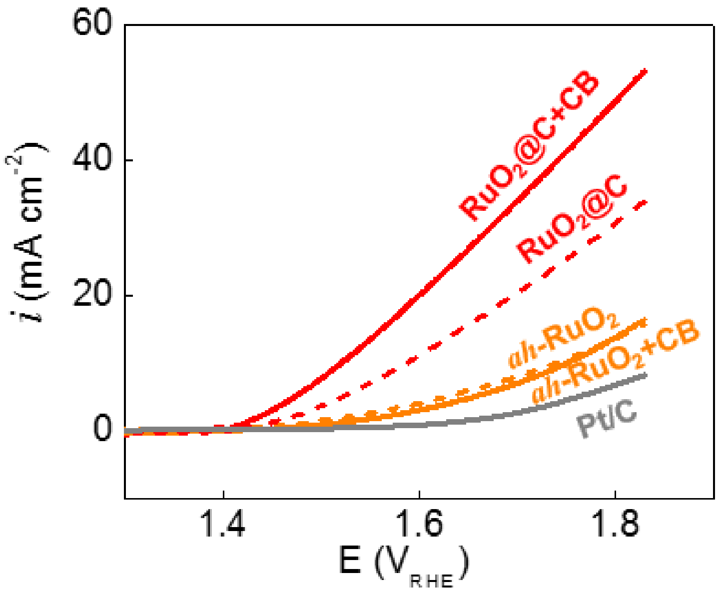

Figure 2.10. OER in N$_2$-saturated 0.1 M KOH (aq). OER polarization curves at 1600 rpm in the first potential sweep cycles at 10 mV s^{-1}.

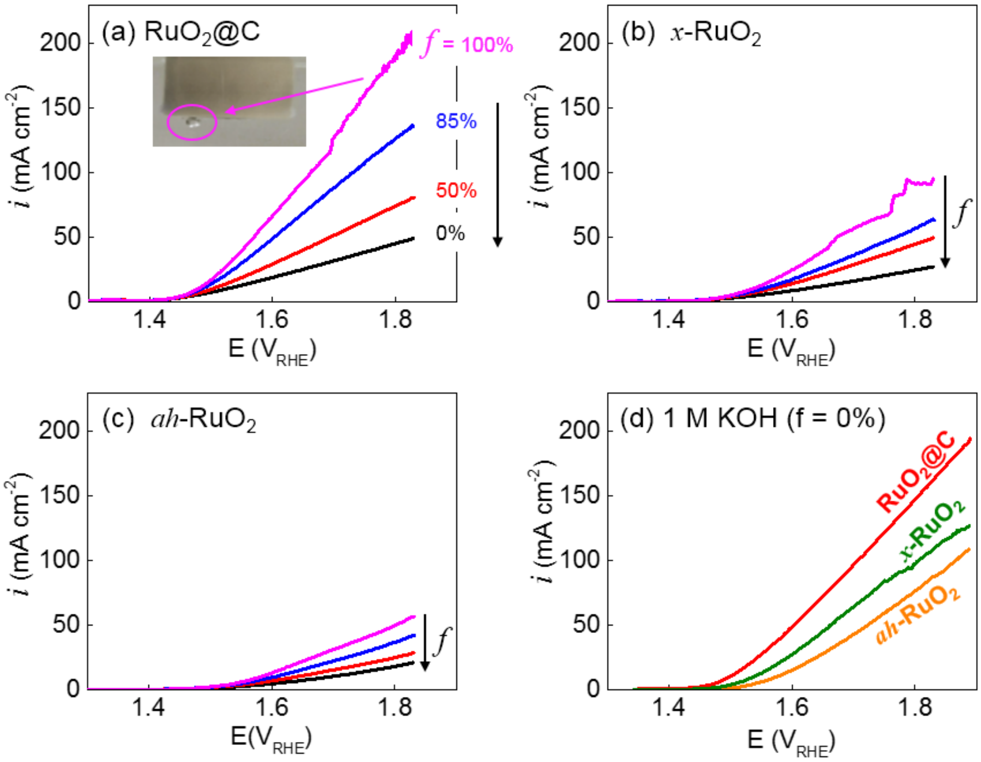

Figure 2.11. IR-compensated OER polarization at 10 mV s^{-1} on 1600 rpm. (**a** to **c**) 0.1 M KOH with various percentages of IR compensation *f*. (**d**) 1 M KOH at *f* = 0 %. The potential shift corrected by the IR compensation factor *f* affected the current values at a fixed potential and the onset potential seriously. Therefore, we should use the IR compensation function carefully and indicate the value of *f*.

Table 2.1. OER and ORR polarization.

Catalysts	ORR [a]			OER [b]	ΔE (V) [c]	Reference
	$E_{L/2}$ (V_{RHE})	$i_{L/2}$ (mA cm^{-2})	n	E_{10} (V_{RHE})		
Pt/C	0.90	-3.0	~4	-	-	This work
RuO_2@C	0.70	-3.0	3.8~3.9	1.55 1.48, 1.47*	0.85	This work
ah-RuO_2	0.65	-2.7	3.6~3.9	1.75 1.60, 1.58*	1.10	This work
RuO_2	0.56	-1.2	~2	1.76	1.20	[45]
RuO_2	0.40	-2.5	-	1.64	1.24	[46]
RuO_2	0.42	-1.5	-	1.60*	1.18	[47]
RuO_2	-	-	-	1.80	-	[21]

[a] $E_{L/2}$ = Half wave potential at the half of limiting current ($i_{L/2}$). [b] E_{10} = Potential obtained at +10 mA cm^{-2}. [c] $\Delta E = |E_{L/2} - E_{10}|$. * Uncompensated IR was corrected in potentials. 85 % and 100 % compensation (*f* = 85 and 100 %) were used for the values with the asterisks in our work while the value of *f* was not reported in reference 47.

In spite of its strength in the onset potential, the hydrous form *h*-RuO_2 showed the severe weakness in stability (**Figure 2.9b**). RuO_2 dissolution during OER is one of the possible reasons for the OER instability especially in *h*-RuO_2.[25, 48] A broad anodic peak was found at 1.6 V_{RHE} for *h*-RuO_2 in the initial anodic scan of potential (**Figure 2.9a**). The stability of the hydrous ruthenium oxide was improved by the carbon matrix (@C) in our RuO_2@C. Specific current density of RuO_2@C reached 54 mA cm^{-2} at 1.83 V_{RHE} and then decreased to 93 % of the initial value after repeating the potential sweep between 1.3 V_{RHE} and 1.83 V_{RHE} 100 times at 10 mV s^{-1} (**Figure 2.9b**). The carbon matrix (@C) of RuO_2@C is believed to protect its partially hydrous RuO_2 from dissolution. The RuO_2@C was most stable also in the chronoamperometric condition at 1.73 V_{RHE} for 60 min in 0.1M KOH (**Figure 2.9c**). The noise-like fluctuation in currents during OER is due to the O_2 bubbles generated on electrode surface. The catalyst size in carbon matrix of RuO_2@C did not significantly change after the chronoamperometric condition, which is in stark contrast to the particle agglomeration in Pt/C under the identical condition (**Figure 2.12**).

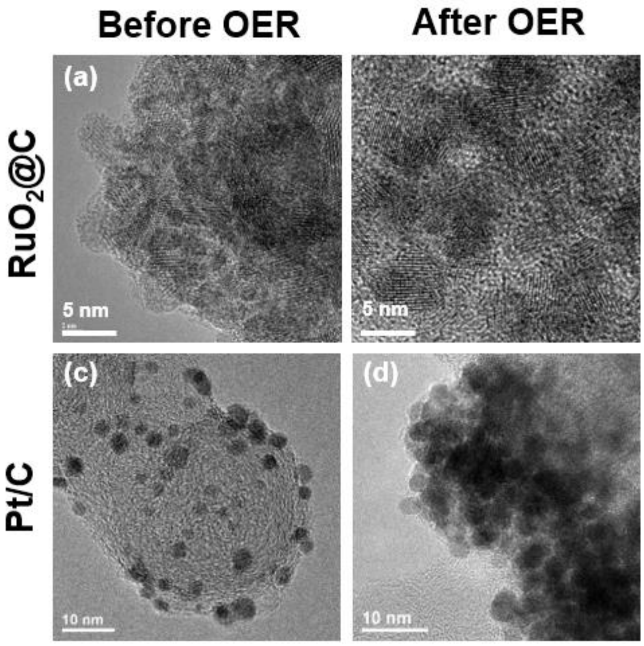

Figure 2.12. OER stability. (**a** to **d**) TEM images showing morphological changes of catalysts between before and after OER at 1.73 V_{RHE} for 1 h in 0.1 M KOH (aq).

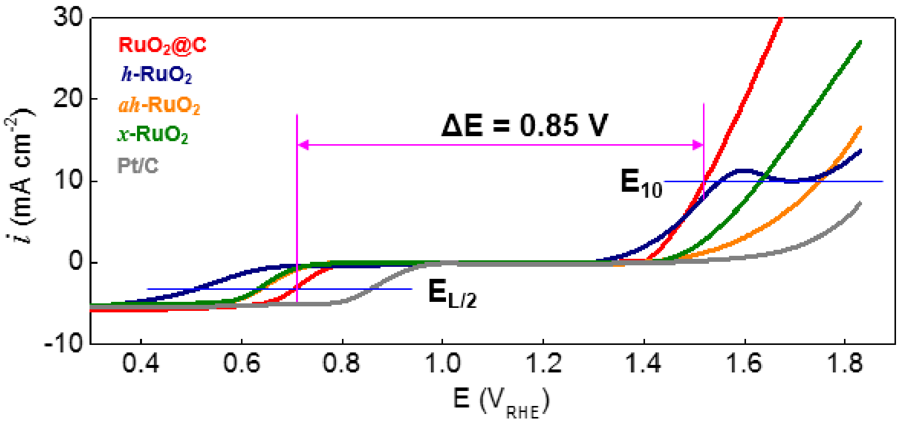

Figure 2.13. ORR and OER in 0.1 M KOH. The overall polarization curves of ORR and OER.

Carbon corrosion is one of the most serious problems in air electrodes of Zn-air batteries during rechargeable operations. The loss in solid carbon caused by the corrosion leads to catalyst loss and electrode leakage, resulting in performance decay.[49] Carbon corrosion proceeds along:[50, 51]

$$C + 2H_2O \rightarrow CO_2 + 4H^+ + 4e^- \qquad E = 1.034\ V_{RHE} \qquad (1)$$

$$C + H_2O \rightarrow CO + 2H^+ + 2e^- \qquad E = 1.345\ V_{RHE} \qquad (2)$$

$$CO + H_2O^- \rightarrow CO_2 + 2H^+ + 2e^- \qquad E = 0.724\ V_{RHE} \qquad (3)$$

When considering the reduction potentials, carbon corrosion is thermodynamically inevitable in the potential range of OER. Reducing the overpotential of OER might be the only way to compress the carbon corrosion. The overpotential benefit of RuO_2@C was evident in the OER stability: the potential maintained stable at < 1.6 V_{RHE} at 5 mA cm^{-2} over 40 h (**Figure 2.9d**). On the other hand, potentials of other RuO_2 counterparts were seriously developed into higher values along time at the same current density.

2.3.4 Rechargeable Zn-air battery

Reversible operation of Zn-air batteries (**Figure 2.14a**) was realized by using the bifunctionality of RuO_2@C (**Figure 2.15**). RuO_2@C, Pt/C or a carbon electrode was used as an air electrode while zinc is used as a metal electrode. The kinetics of ORR and OER was investigated from the discharge rate capability at a fixed slow charge (**Figure 2.15a**) and charge rate capability at a fixed slow discharge (**Figure 2.15b**), respectively. Pt/C showed the smallest ORR overpotential but severe OER overpotential development larger than even the non-catalytic carbon electrode especially at high current densities (>200 mA). RuO_2@C showed fairly good ORR polarization even if its overpotentials are larger than those of Pt/C. Interestingly, the overpotential difference between RuO_2@C and Pt/C in the Zn-air battery cells (~0.1 V) was smaller than the difference of half wave potential ($E_{L/2}$) between them in linear sweep voltammograms (~0.2 V in **Figure 2.6a**). The RuO_2@C-based battery was successfully charged at the potential lower than cells based on Pt/C and carbon electrode especially at high currents (**Figure 2.15b**). Stable potential profiles were obtained in the presence of RuO_2@C up to the fast charge at 200 mA. Potential difference between charge and discharge ($\Delta E_{OER\text{-}ORR}$) of RuO_2@C was critically superior to those of Pt/C and carbon air electrode (**Figure 2.14b**): 1.1 V for RuO_2@C versus 1.6 to 1.7 V for the others at 100 mA; 1.65 V for RuO_2@C versus ~5 V for the others at 200 mA. The smaller $\Delta E_{OER\text{-}ORR}$ of RuO_2@C indicates the higher degree of reversibility between ORR and OER.

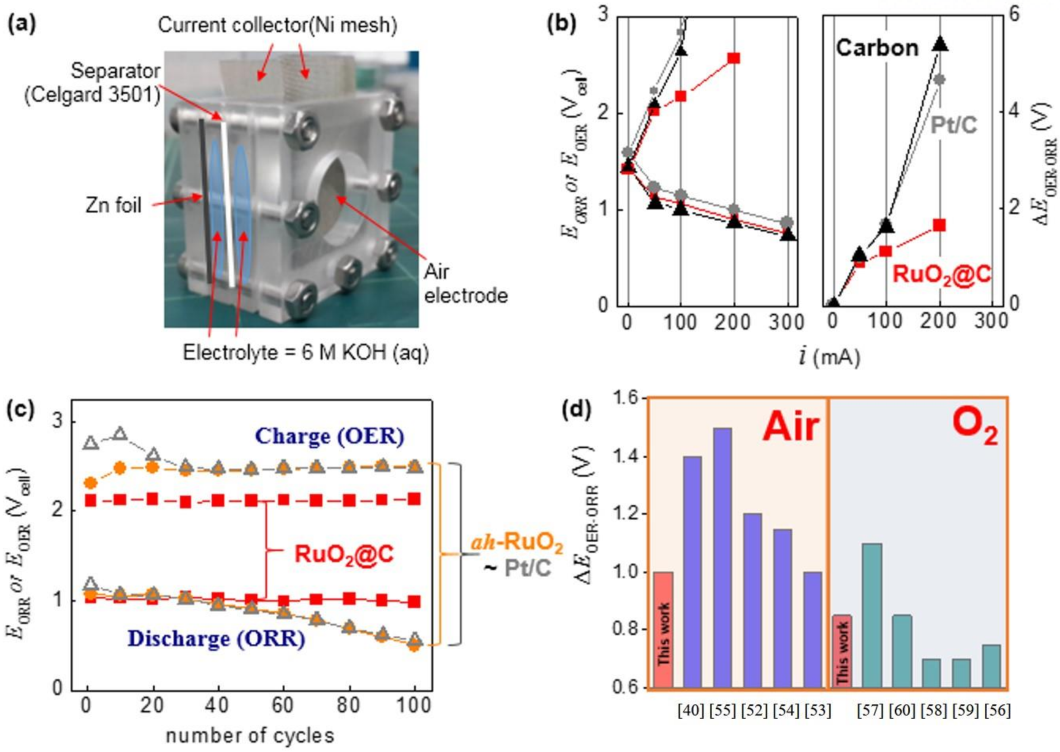

Figure 2.14. Zn-air battery cells. (a) The home-made Zn-air cell. Geometric area of air electrode = 2.2 cm^2. **(b)** The ORR and OER potentials (E_{ORR} or E_{OER} in the left panel) and the potential gaps between ORR and OER ($\Delta E_{\mathrm{OER\text{-}ORR}}$) calculated from E_{ORR} and E_{OER} as a function of current. Data were taken from Figure 4a and b. **(c)** Cell potentials during discharge and charge. Refer to Figure 4c and d for its full potential profiles. **(d)** Comparison of $\Delta E_{\mathrm{OER\text{-}ORR}}$ between RuO_2@C in this work and other electrocatalysts in other works. The details were given in Table S2. The cells were categorized to groups in terms of fuels. 20 % and 100 % of molecular oxygen were used for Zn-air cells and Zn-O_2 cells, respectively.

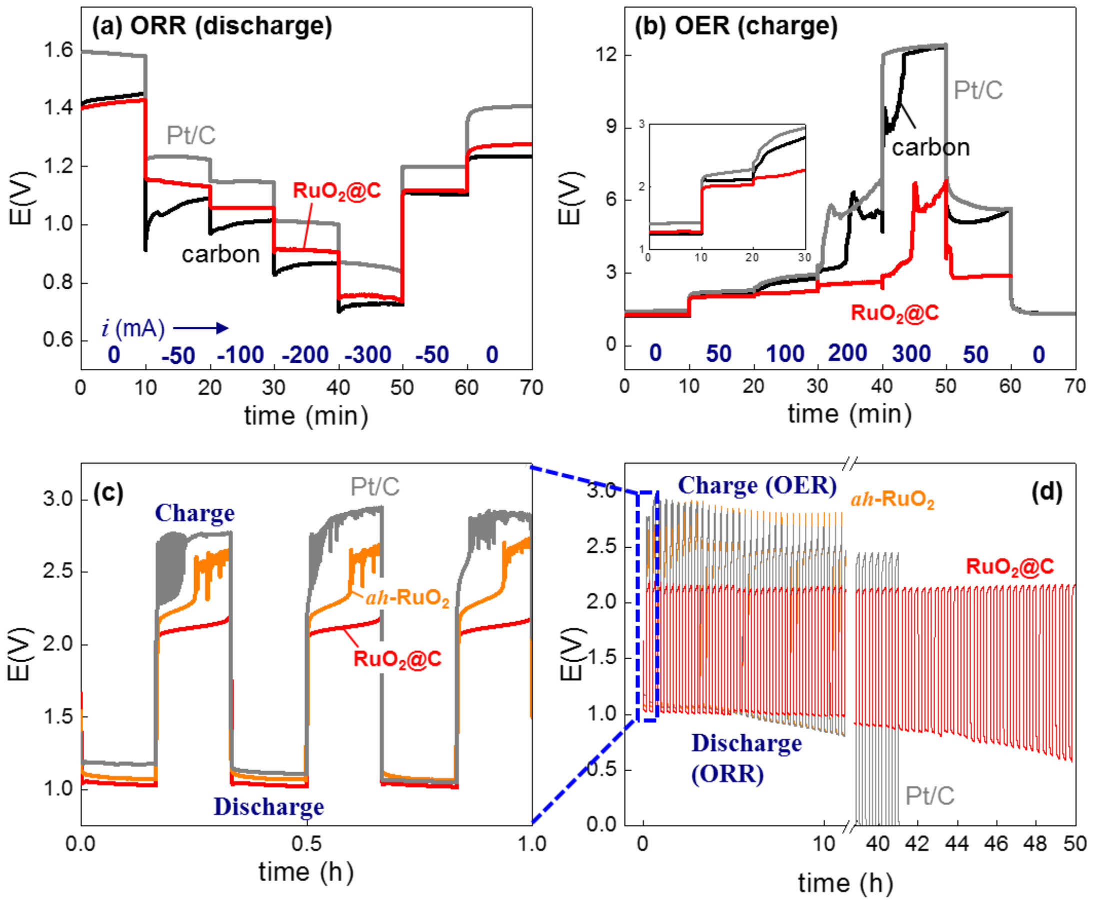

Figure 2.15. Zn-air batteries. 20 wt. % carbon black was used for RuO$_2$@C. Pt loading of Pt/C was 20 wt. %. (a) Discharge rate capability at 20 mA cm^{-2} charge. ORR proceeds on air electrodes. Currents used for discharge were indicated in mA (geometric electrode area = 2.8 cm^2). (b) Charge rate capability at 20 mA cm^{-2} discharge. OER proceeds on air electrodes. Currents used for charge were indicated in mA (geometric electrode area = 2.8 cm^2). (c and d) Galvanostatic charge/discharge cycles at 20 mA cm^{-2}.

To further confirm the rechargeability of RuO$_2$@C-based Zn-air batteries, the cells were repeatedly discharged and charged in the galvanostatic manner at 20 mA cm^{-2} with a 20-min cycle period for 50 h (**Figure 2.15c** and **d**). The potentials of RuO$_2$@C were stably maintained at 1.04 V during discharge and 2.11 V during charge over 40 h or 120 cycles (**Figure 2.14c**). The decrease in ORR potential during discharge after 40 h was caused *not* by the failure of catalysts *but* by leakage of electrolyte through the gas diffusion layer of air electrode (hindering oxygen supply). There was no problematic deterioration found in the Zn||RuO_2@C cell during OER. Different from RuO_2@C, however, performance loss of the Pt/C or carbon-based Zn-air cells was triggered by the catalyst failure during OER process. The OER overpotentials were seriously developed from the initial charge. When compared with the cell operation data reported from other literatures, the cells based on the RuO_2@C were confirmed to be the most reversible Zn-air cells.[40, 52-55] The potential gap between charge and discharge ($\Delta E_{\text{OER-ORR}}$) was 1.0 V, the value which is smaller than those of other works in air (**Figure 2.14d** and **Table 2.2**). The potential gap decreased to 0.85 V when the same cell was operated at the stationary atmosphere of 100 % oxygen (instead of air). The reversibility of our Zn-oxygen cell is believed to be top-tier in $\Delta E_{\text{OER-ORR}}$ even if smaller values of $\Delta E_{\text{OER-ORR}}$ were found in other works (**Figure 2.16** and **Table 2.2**).[56-60] In the Zn-oxygen cells showing higher reversibility than ours, oxygen was forced to be introduced through the cells or electrolytes.

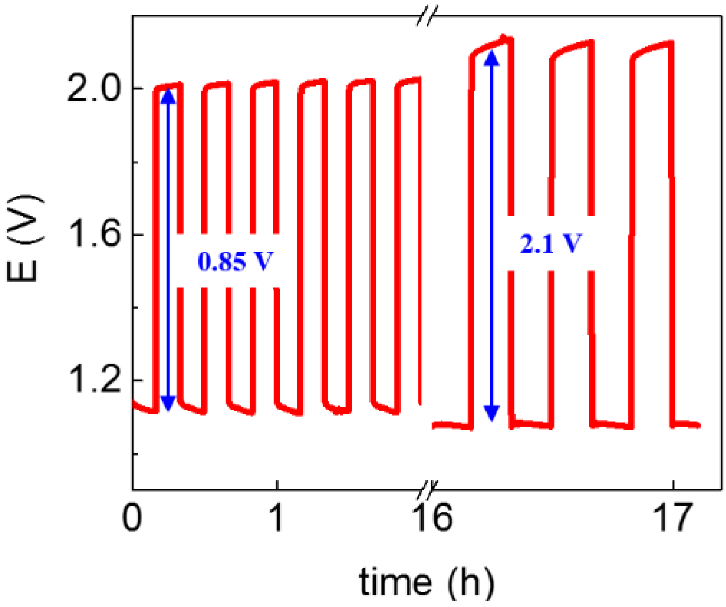

Figure 2.16. Galvanostatic charge/discharge cycles at 20 mA cm^{-2} in O_2 atmosphere at 1 atm.

Table 2.2. Performance of rechargeable zinc-air batteries of various electrocatalysts published in the literature.

Catalyst	Charge (V) @ 20 $mAcm^{-2}$	Discharge (V) @ 20 $mAcm^{-2}$	Gap (V)	Cycle test condition	Atmosphere	Reference
RuO_2 nanoclusters embedded in carbon matrix	2.05	1.05	1.0	20min per cycle, 150 cycles, @ 20 mA/cm^2	Air	This work
$LaNiO_3$ macrospheres / N-CNT N-CNT = nitrogen-doped carbon nanotube	2.4	1.0	1.4	10 min per cycle, 75 cycles @ 17.6 mA/cm^2	Air	[40]
MnO_2 nanotube / N-CNT	2.6	1.1	1.5	10 min per cycle, 50 cycles, @ 20 mA	Air	[55]
Co_3O_4 nanocrystals / N-CNT	2.2	1.0	1.2	10min per cycle, 240 cycles, @ 20 mA/cm^2	Air	[52]
Co_3O_4 nanoparticle / modified MnO_2 nanotubes	2.25	1.1	1.15	14 min per cycle, 60 cycles @ 15 mA/cm^2	Air	[54]
Co-doped TiO_2	2.1	1.1	1.0	20 h per cycle, 37 cycles @ 20 mA/cm^2	Not specified	[53]
RuO_2 nanoclusters embedded in carbon matrix	2.0	1.15	0.85	20min per cycle, 51 cycles, @ 20 mA/cm^2	O_2 atmosphere	This work
cobalt and nitrogen embedded carbon nanotubes	2.2	1.1	1.1	10 min per cycle, 16 cycles @ 15 mA/cm2	O_2 atmosphere	[57]
CoO / N-CNT + NiFe LDH LDH = layered double hydroxide	2.05	1.2	0.85	240 min (4 hr) per cycle, 10 cycles @ 50.0 mA/cm^2	O_2 purged	[60]
$CoMn_2O_4$ nanoparticles anchored on N-doped rGO nanosheets	1.8	1.1	0.7	10 min per cycle, 100 cycles @ 20 mA/cm^2	O_2 flow	[58]
1D-$NiCo_2O_4$ nanostructures	1.8	1.1	0.7	40 min per cycle, 50 cycles @ 20.0 mA/cm^2	O_2 flow	[59]
$Co(II)_{1-x}Co(0)_{x/3}Mn(III)_{2x/3}S$ Nanoparticles / B/N-co-doped Mesoporous Nanocarbon	2.0	1.25	0.75	4 hr per cycle, 5 cycles @ 20 mA/cm^2	O_2 purged	[56]

2.4 Conclusions

The merits of hydrous and anhydrous ruthenium oxides (*h*-RuO_2 and *ah*-RuO_2) were realized by embedding the partially hydrous RuO_2 nanoparticles in a carbon matrix (RuO_2@C). The degree of hydration (x) of RuO_2@C was 0.27 (quarter hydrous). The RuO_2@C was anhydrous-like in terms of smaller ORR onset overpotential and better OER stability; and hydrous-like due to its higher number of electron transfer in ORR and the smaller OER onset overpotential. We demonstrated the superiority of the RuO_2@C by operating zinc-air battery cells. The smallest overpotentials guaranteed the efficient operation of rechargeable zinc-air batteries.

Chapter 3. RuO_2 nanocluster as a 4-in-1 electrocatalyst for hydrogen and oxygen electrochemistry

3.1 Introduction

Hydrogen economy is one of the possible and potential alternatives to the present hydrocarbon economy even if the concept has been criticized in terms of its low conversion efficiencies and infeasible competitive edge over other energy sources. Hydrogen production and its conversion to electricity are the starting and ending points of hydrogen economy, respectively. Water electrolysis is one of the main production method that is more environmentally friendly than steam reformation of hydrocarbons. However, the electrolysis has the issues of high cost and low efficiencies. [5, 61-63] Electrocatalysts have been developed to improve water electrolysis efficiencies while renewable energy sources were combined with electrolyzers for cost reduction. [64, 65]. On the other hand, various types of fuel cells have been considered as candidates of hydrogen/electricity conversion.[66] As a more advanced type of hydrogen-based devices, regenerative fuel cells function as water electrolyzers to produce hydrogen in its regenerative or reverse mode and as fuel cells to generate electricity in its fuel cell mode.[67] The core element of electrolyzers and fuel cells is electrocatalyst to fasten kinetics of hydrogen evolution reaction (HER) and oxygen evolution reaction (OER) for water electrolysis; and hydrogen oxidation reaction (HOR) and oxygen reduction reaction (ORR) for fuel cells (**Figure 3.1**). HER and OER is the backward reactions of HOR and ORR, respectively. If we use a tetra-functional catalyst, we can make the regenerative fuel cell composed of mono catalyst more efficiently and inexpensively. In this work, we present a single catalyst for all four reactions, demonstrating successful operation of symmetric water electrolyzers using a commercial solar cell and 1.5 V battery.

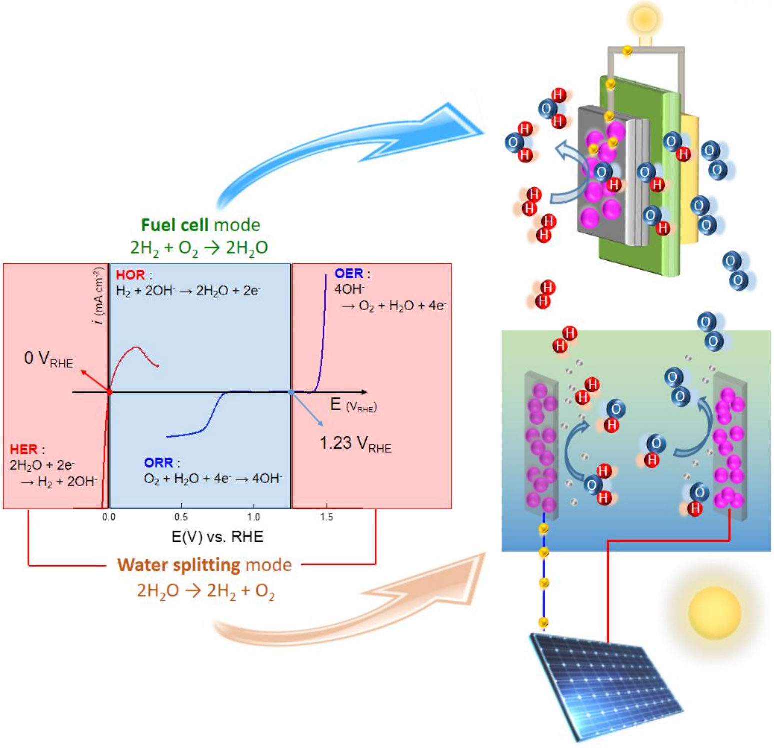

Figure 3.1. Regenerative fuel cells for hydrogen economy. Hydrogen is produced in the water splitting mode powered by renewable energy such as solar cells. The hydrogen is used to generate electricity in the fuel cell mode. The fuel cell mode is operated by the backward reactions of the water splitting mode.

The electrochemical water splitting is composed of two reactions: HER at $E^o = 0\ V_{RHE}$ (E^o = standard reduction potential, V_{RHE} = V versus RHE) and OER at 1.23 V_{RHE}.

Acid **Base**

HER: $2H^+ + 2e^- \rightarrow H_2$ $2H_2O + 2e^- \rightarrow H_2 + 2OH^-$ (1)

OER: $2H_2O \rightarrow O_2 + 4H^+ + 4e^-$ $2OH^- \rightarrow O_2 + 2H_2O + 4e^-$ (2)

Two issues are most challenging in the field of electrocatalysts for water electrolysis: (1) bifunctional catalysts covering both HER and OER; and (2) HER or OER catalysts working in a wide span of pH.[68-70]

First, high-performance monofunctional catalysts such as Pt for HER and Ir, Ru and their oxides for OER have been developed. However, HER/OER-bifunctional catalysts covering both reactions for water electrolysis have been limitedly reported.

Transition metal oxide, sulfide and phosphate were developed as the bifunctional catalysts for HER and OER. [71-75] Moreover, ORR in addition to HER and OER was covered by single-catalyst systems such as doped or defective graphenes and their composites with metal oxide. [76-79] However, their electroactivities were reported far below those of the well-known monofunctional catalysts. Ru-based catalysts are considered as the candidate for the HER/OER bifunctional catalysts, which is supported by two recent publications.[80, 81] Bifunctional catalysts possibly simplify water electrolysis systems and lower their development cost because a single catalyst covers both electrodes. [82] In conventional asymmetric electrolyzers, the HER catalysts are different from the OER catalysts. The OER electrode compartment is exposed to oxidative environments while the HER compartment experiences reductive potential. The long-term oxidative and reductive loads on electrodes possibly deteriorate or corrode the parts of electrolyzers. On the other hand, the symmetric electrolyzer based on the single bifunctional catalysts can be operated by switching electrodes periodically. More durable operation of water electrolysis is expected. [83]

Second, HER catalysts developed until now favors acid media while OER catalysts work efficiently in alkaline media. [5, 70, 84] Therefore, it is difficult to pair the best HER catalysts with the best OER catalysts at a fixed pH for water electrolysis. Alkaline electrolytes have been widely used for mass hydrogen production so that developing high-HER-electroactivity catalysts at high pH is of great importance. [71, 81, 85] Alternatively, catalysts guaranteeing high OER electroactivities and stability in acid media open extended opportunities of acid-electrolyzer. [56, 86, 87] On the other hand, electrolyte around pH 7 is the poorest media for water electrolysis because both H_2 and O_2 are generated from water molecules instead of H^+ and OH^-. The water electrolysis based on the neutral media, if possible, benefits from safety, cost and corrosion-free conditions. [70, 88, 89]

In our previous work (chapter 2)[90], we demonstrated ORR/OER bifunctionality of RuO_2-based catalysts in *alkaline* media. RuO_2 has been known as one of the best OER catalysts but its ORR activity was unexpected before. The key factor to control both ORR and OER activities was hydration degree of RuO_2 (n in $RuO_2 \cdot nH_2O$). Partial hydration improved OER kinetics on RuO_2: the current at 1.6 V_{RHE} of a partially hydrated RuO_2 was more than 10 times as high as that of totally anhydrous RuO_2. Moreover, the partial hydration significantly reduced overpotentials of ORR by ~200 mV at -3 mA cm^{-2}. Herein, we extended the OER/ORR electroactivity of RuO_2 to HER. Recently, a ruthenium-based electrocatalyst was reported to show platinum-level HER activities while its cost is only ~4 % of that of platinum. [80] The partially hydrated RuO_2 of this work showed both OER and HER electroactivities for water electrolysis over a wide range of pH including pH 0, pH 7 and pH 14. This catalyst of this work is the first bifunctional water splitting catalyst working *at all pH* and showing high electroactivities of both HER and OER. Xue et al. reported that the HER/OER bifunctional electroactivities of Co/CoP at universal pH, but its OER activities were seriously inferior to the reported values of OER activities of monofunctional catalysts. [91] A *symmetric* electrolyzer based on the single catalyst was realized, which is characterized by small overpotential superior to the *asymmetric* electrolyzer based on Pt and Ir considered as the best pair for water splitting. As an additional extension, we demonstrated that the HER/OER catalyst covered HOR and ORR. The tetrafunctional catalysts possibly simplify the regenerative fuel cell systems where two bifunctional catalysts are required [67] (one for HER and HOR while the other for OER and ORR). The 4-in-1 electrocatalysts have not been reported yet even if tri-functional catalysts for HER, OER and ORR are available.[76-79]

3.2 Experimental Method & Materials

3.2.1 Materials

Partially hydrated RuO_2 (x-RuO_2@C) was synthesized as described in our previous work.[90] Briefly, aqueous suspension of hydrous RuO_2 nanoparticles templated by PEO_{5000}-b-PAA_{6700} (numbers in subscript = molecular weights of each block; Polymer Source) were prepared from an aqueous mixture of the block copolymer, NaOH, $RuCl_3 \cdot xH_2O$ (Sigma-Aldrich) and hydrazine (N_2H_4; Sigma-Aldrich). The dried suspension was annealed at 400 ^{o}C for 2 h to form x-RuO_2@C. Totally anhydrous RuO_2 (*ah*-RuO_2; 30 to 50 nm primary particles from Sigma-Aldrich) and totally hydrous RuO_2 (*h*-RuO_2; 100 to 200 nm primary particles from Alfa Aesar) were used as received for comparison (Figure S2). Pt/C (20 wt. % Pt on carbon black, Alfa Aesar) and Ir/C (20 wt % Ir on carbon black, Premetek) were also used for comparison.

3.2.2 Characterization.

Catalysts were characterized by transmission and scanning electron microscopes (JEOL JEM-2100F for TEM and Hitach S-4800 for SEM) and X-ray diffraction (XRD; Rigaku D/MAX 2500V/PC with Cu–Kα radiation (λ = 1.5418 Å) at 35 kV and 20 mA).

3.2.3 Catalyst inks

Homogeneous catalyst inks were prepared by dispersing 8 mg catalyst composite and 2 mg Ketjen Black 600 in a mixture of 450 μl of ethanol and 50 μl of 5 wt. % Nafion solution (Sigma-Aldrich, 274704) by using sonication for 30 min. 6 ml of the catalyst ink was dropped onto a polished glassy carbon (GC, 0.1256 cm^2) disk of rotating ring disk electrodes (RRDE with Pt ring/GC disk; ALS, A-011162) and then fully dried at ambient temperature. In addition to the synthesized x-RuO_2@C, anhydrous (Sigma-Aldrich, 238058) and hydrous (Alfa Aesar, 43403) ruthenium oxides (*ah*- and *h*-RuO_2) were used as control catalysts. Also, 20 wt. % Pt on carbon black (Alpha Aesar, 35849, HiSPEC 3000) and 20 wt % Ir on Vulcan XC72 (Premetek, P40A200) were used as control catalyst composites for HER and OER, respectively.

3.2.4 Electrochemistry

The polarization curves were obtained in 3-electrode configuration including RRDEs by a potentiostat (Bio-Logic VMP3). Catalyst-loaded RRDE as working electrode was immersed in a glass cell containing 1 N H_2SO_4 (pH 0), 1 N phosphate buffer solution (pH 7), 0.1 N KOH (pH 13) and 1 N KOH (pH 14). Ag/AgCl (RE-1B, ALS; pH 0 and 7)) and Hg/HgO (XR400, Radiometer Analytical; pH 13 and 14) were used as reference electrodes, and Pt wire was used as counter electrodes. The HER and OER polarization voltammograms at 10 mV s^{-1} were obtained in N_2-purged electrolytes at 1600 rpm. The HOR and ORR polarization curves were recorded in the H_2- and O_2-saturated electrolytes at 1600 rpm with a scan rate of 10 mV s^{-1}. Unless otherwise noted, all polarization curves were iR (f = 85 %) corrected by using the EC-Lab software. Potentials were reported as the values versus reversible hydrogen electrode (RHE) in V_{RHE} (V versus RHE). Exchange currents (i_o), as a kinetics descriptor, were estimated by using Tafel equation. All electrochemical data were obtained at room temperature.

3.2.5 Water splitting

Lab-made water electrolyzer was constructed. 100 μl catalyst ink was loaded on 1 cm^2 carbon papers (Toray TGP-H-0930) for acidic electrolytes or porous nickel foams (MTI EQ-bcnf-16m) for alkaline electrolytes. Catalyst loading density was fixed at 0.8 mg_{cat} cm^{-2}. The catalyst-loaded electrodes were dried at 80 ^{o}C for > 1 h. Two catalyst-loaded electrodes were immersed in an electrolyte-containing acrylic container equipped with 20 mL graduated gas collectors. 1 N KOH (aq) or 1 N H_2SO_4 (aq) was used as electrolyte. Water was electrolyzed potentiostatically by using 1.5 V AA batteries or galvanostatically by using a galvanostat (Bio-Logic, VMP3).

3.2.6 Alkaline anion exchange membrane water electrolyzer (AEMWE)

AEMWEs were made by sandwiching an alkaline anion exchange membrane between two identical electrodes. Graphite blocks designed for allowing serpentine flows of electrolytes backed up the electrodes, which were contacted to aluminum end plates. *0.27*-RuO_2@C was loaded at 1.0 mg cm^{-2} on carbon papers (TGP-H-120, Toray) in the presence of 20 wt. ionomer (fumion® FAA-3 solution, Fumatech). The electrodes and an anion exchange membrane (fumasep® FAA-3-PK-75, Fumatech) were stored in 1.0 N KOH solution for 24 h to exchange bromide anions of ionomers to hydroxide ions, followed by washing with distilled water to remove excess KOH solution. The AEMWEs were operated at room temperature with 0.5 N KOH solution as the feed solutions for both anode and cathode. Linear sweep voltammograms were obtained between 1.4 V_{cell} to 2.0 V_{cell} at 20 mV s^{-1} before potentiostatic operations at 1.6 V_{cell}. Electrochemical impedance spectra (EIS) were obtained at 1.6 V_{cell} in 30 kHz to 30 mHz with a sinusoidal amplitude at 10 mV.

3.3 Results and Discussion

3.3.1 *x*-RuO_2@C as catalyst

The partially hydrated RuO_2 was synthesized as a form of nanoclusters consisting of 5 nm RuO_2 nanoparticles embedded in a continuous carbon matrix phase (*x*-RuO_2@C in **Figure 3.2a**). Electroactivities of *x*-RuO_2@C were compared with those of totally anhydrous and hydrous RuO_2 in this work (*ah*-RuO_2 in **Figure 3.2b** and *h*-RuO_2 in **Figure 3.2c**, respectively). Hydrated phase (*h*-RuO_2) was amorphous while anhydrous or partially hydrous RuO_2 showed crystal phases (**Figure 3.2d**). The relative hydration degree (*x*) of *x*-RuO_2@C prepared at 400 °C was estimated at 0.27 when the hydration degrees of *ah*-RuO_2 and *h*-RuO_2 were taken as 0 and 1, respectively (**Figure 3.2e**). Annealing temperatures determined hydration degrees and then electroactivities. The most optimized sample showing the well balanced multi-functionality in this work was

0.27-RuO_2@C that was annealed at 400 ^{o}C. The samples synthesized from five different batches at the same annealing temperature showed hydration degrees between 0.25 and 0.29: average = 0.266 with standard deviation = 0.0167. Their electroactivities were estimated very close to each other. Hydration numbers decreased with increasing temperature (**Figure 3.4**). *0.5*-RuO_2@C and *0.14*-RuO_2@C, more and less highly hydrous catalysts than *0.27*-RuO_2@C, were obtained at 350 ^{o}C and 450 ^{o}C, respectively. Higher hydration degree supported more improved HER and OER activities (**Figure 3.5**). However, the stability of OER activities of too hydrous samples (*0.5*-RuO_2@C) was not guaranteed (0.5@C of **Figure 3.5b**).

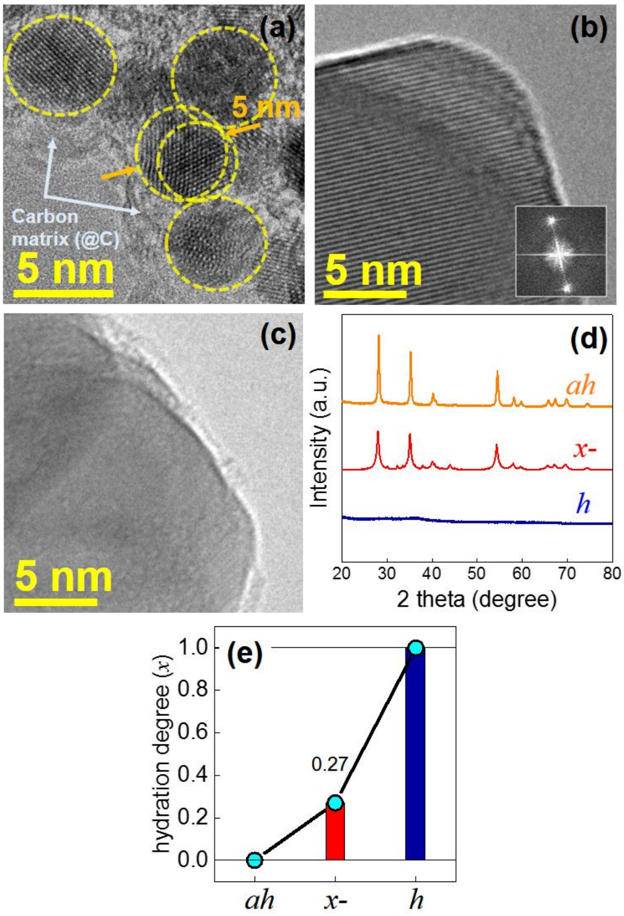

Figure 3.2. Partially hydrous ruthenium oxide embedded in carbon (*x*-RuO_2@C). (**a** to **c**) TEM images: **a** = *x*-RuO_2@C; **b** = anhydrous RuO_2 (*ah*-RuO_2); **c** = hydrous RuO_2 (*h*-RuO_2). (**d**) Relative hydration number of RuO_2-based catalysts. (**e**) XRD patterns of *x*-, *ah*- and *h*-RuO_2.

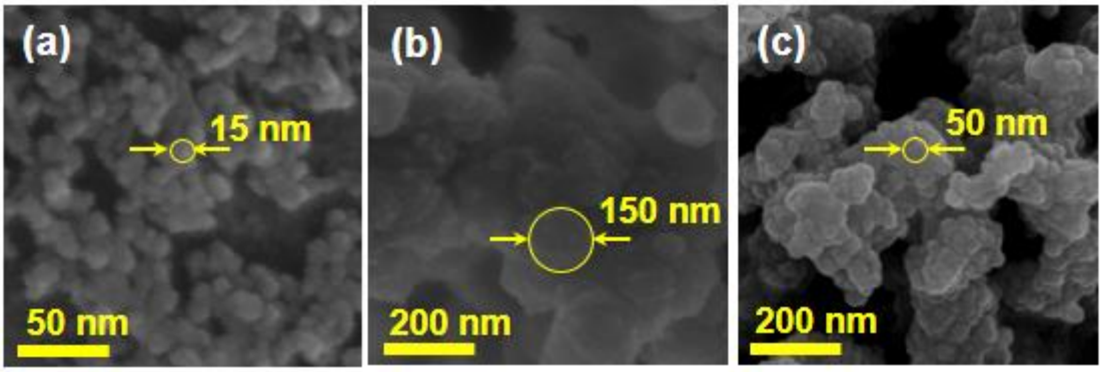

Figure 3.3. Partially hydrous ruthenium oxide embedded in carbon(x-RuO_2@C). (**a** to **c**) SEM images: **a** = *0.27*-RuO_2@C; **b** = anhydrous RuO_2 (*ah*-RuO_2); **c** = hydrous RuO_2 (*h*-RuO_2).

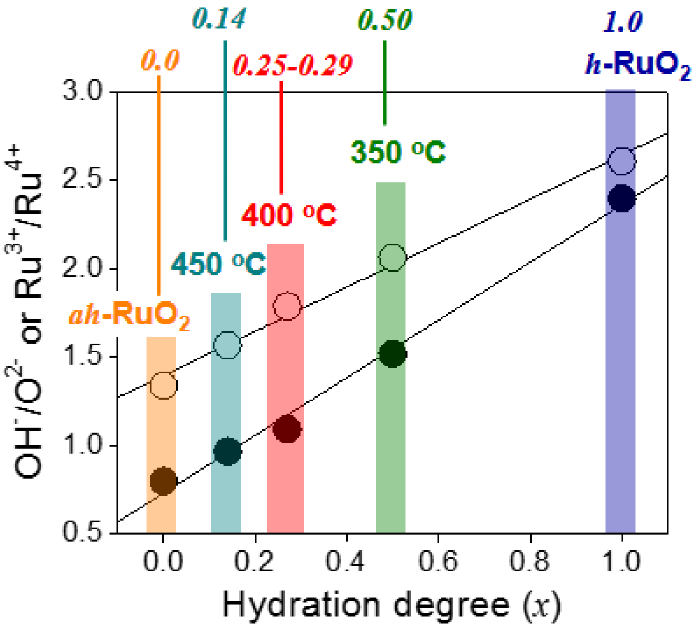

Figure 3.4. Dependency of hydration degree (x) of x-RuO_2@C on annealing temperature. The value of x was determined by X-ray photoelectron spectra.

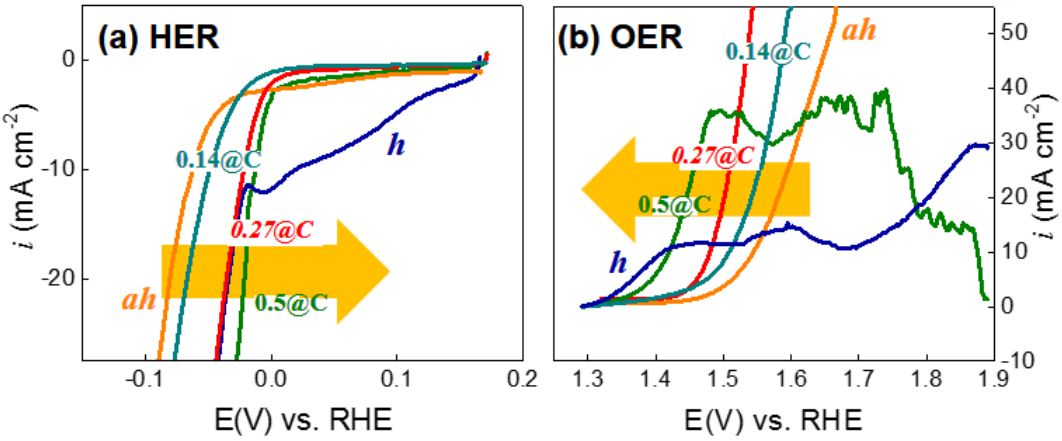

Figure 3.5. HER and OER polarization at pH 14. Refer to the caption of Figure 3.4 for detailed information. #@C = RuO_2@C with hydration degree indicated by #. Large arrows indicate the direction of overpotential reduction.

3.3.2 HER

The HER electroactivity of *0.27*-RuO_2@C (or shortly *0.27*@C) in 1 N KOH at pH 14 was comparable to or even better than that of Pt/C that is known as the best HER catalyst (**Figure 3.6a** and **Figure S2a**). The onset potentials of *0.27*-RuO_2@C and Pt/C were identical while higher HER current was obtained by *0.27*-RuO_2@C at high overpotentials. Hydrated phase was considered beneficial for HER electroactivity because partially or totally hydrous RuO_2 (*0.27*-RuO_2@C and *h*-RuO_2) was superior to *ah*-RuO_2 in terms of the HER onset potentials. The kinetics of *0.27*-RuO_2@C was superior to that of *h*-RuO_2 specifically at high overpotentials probably due to the carbon matrix (@C) providing conductive environments to *0.27*-RuO_2. The HER activity of *0.27*-RuO_2@C became more inferior to that of Pt/C as electrolyte was changed from alkaline to acid (1 N sulfuric acid at pH 0) to neutral (1 N phosphate buffer solution at pH 7) (**Figure 3.6c, e** and **Figure 3.7c, e**; **Figure 3.8c** for Tafel plots). It should be emphasized that the HER activities of *0.27*-RuO_2@C were superior to those of any other *multi-functional* catalysts ever reported throughout all pH covering base, acid and neutral media (**Figure 3.9** and **Table 3.1**). For example, less than 100 mV overpotential was required by *0.27*-RuO_2@C for HER to extract -10 mA cm^{-2} in neutral media that was the poorest media for water splitting. Much higher overpotentials were required at the same current density by previously reported catalysts: 140 mV by Co/CoP nanoparticles [91]; 337 mV by CoO/$CoSe_2$ nanobelts [92]; 480 mV by N or S co-doped graphitic sheets [78]. Even more improved electroactivities of *0.27*-RuO_2@C were observed up to 1500 potential sweeps between +0.2 V_{RHE} and -0.2 V_{RHE} in 1 N KOH (aq) (**Figure 3.10**). The current density at -0.2 V_{RHE} at the 1500th cycle was 1.5 times as high as that at the 1st cycle. Insignificant current changes in polarization curves were found after the 1500th cycle. The HER durability is contrasted with that of Pt/C showing electroactivity decay during long-term cycle tests [80].

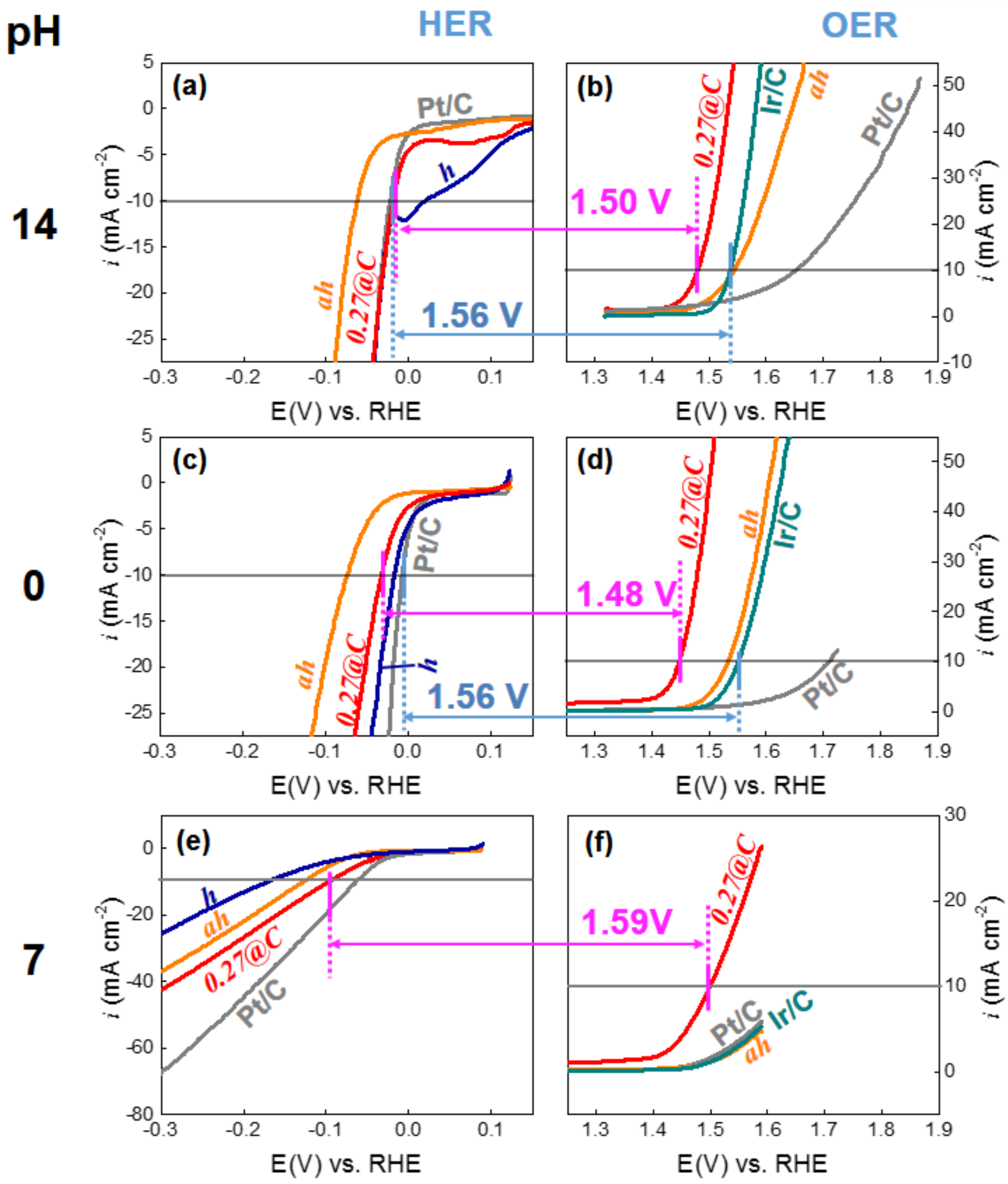

Figure 3.6. HER and OER polarization. The plots in the left and right columns are for HER and OER, respectively. Three different electrolytes were used: 1 N KOH at pH 14 (**a** and **b**); 1 N H_2SO_4 at pH 0 (**c** and **d**); and 1 N phosphate buffer solution (PBS) at pH 7 (**e** and **f**). Rotating disk electrodes of glassy carbon in 0.1256 cm^2 were used at 1600 rpm. 20 wt. % carbon black was used for ruthenium-oxide-based catalysts. ***h*** = *h*-RuO_2; ***ah*** = *ah*-RuO_2; ***0.27*@C** = 0.27-RuO_2@C.

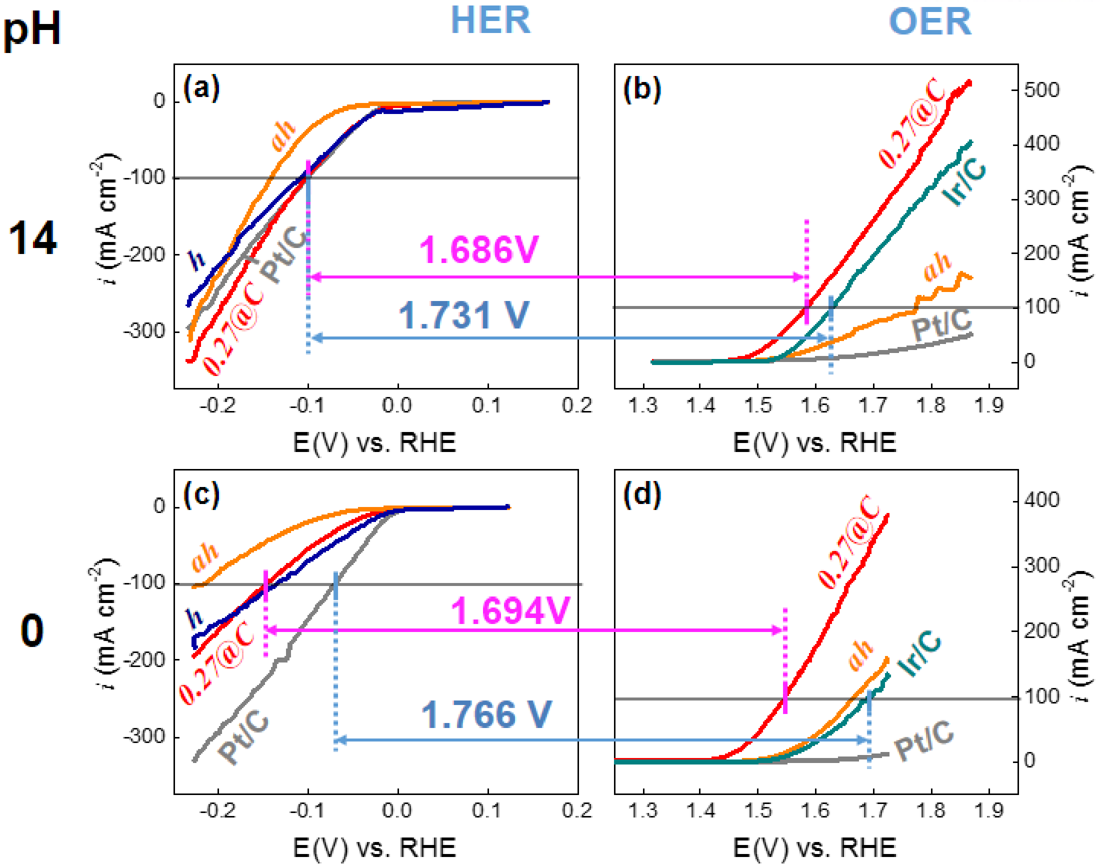

Figure 3.7. HER and OER polarization. The plots in the left and right columns are for HER and OER, respectively. Two different electrolytes were used: 1 N KOH at pH 14 (**a** and **b**); 1 N H_2SO_4 at pH 0 (**c** and **d**). Rotating disk electrodes of glassy carbon in 0.1256 cm^2 were used at 1600 rpm. 20 wt. % carbon black was used for ruthenium-oxide-based catalysts. ***h*** = *h*-RuO_2; ***ah*** = *ah*-RuO_2; ***0.27*@C** = *0.27*-RuO_2@C.

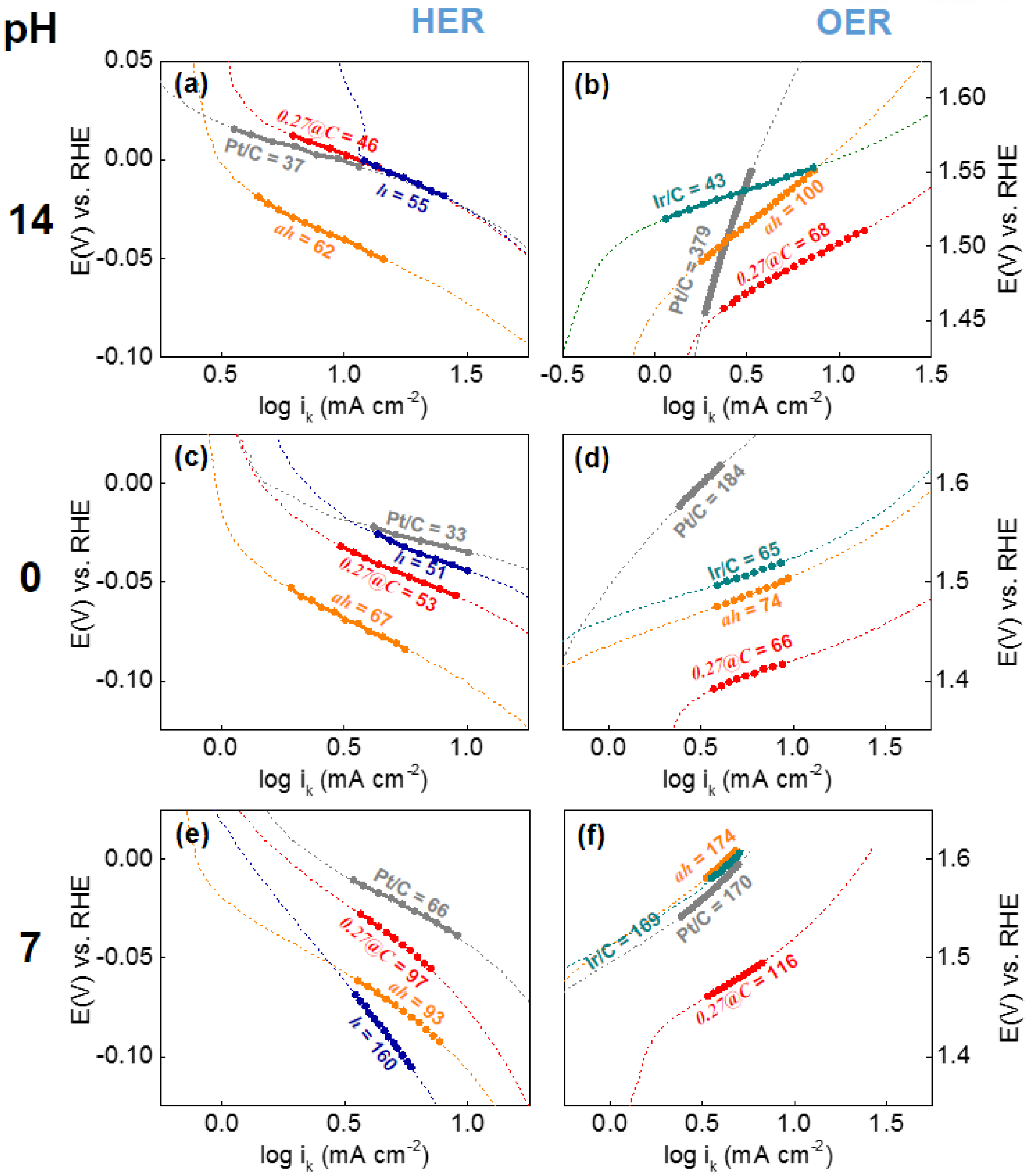

Figure 3.8. Tafel plot from HER and OER polarizations. The plots in the left and right columns are for HER and OER, respectively. Three different electrolytes were used: 1 N KOH at pH 14 (**a** and **b**); 1 N H_2SO_4 at pH 0 (**c** and **d**); and 1 N phosphate buffer solution (PBS) at pH 7 (**e** and **f**). Rotating disk electrodes of glassy carbon in 0.1256 cm^2 were used at 1600 rpm. 20 wt. % carbon black was used for ruthenium-oxide-based catalysts. ***h*** = *h*-RuO_2; ***ah*** = *nh*-RuO_2; ***0.27*@C** = *0.27*-RuO_2@C.

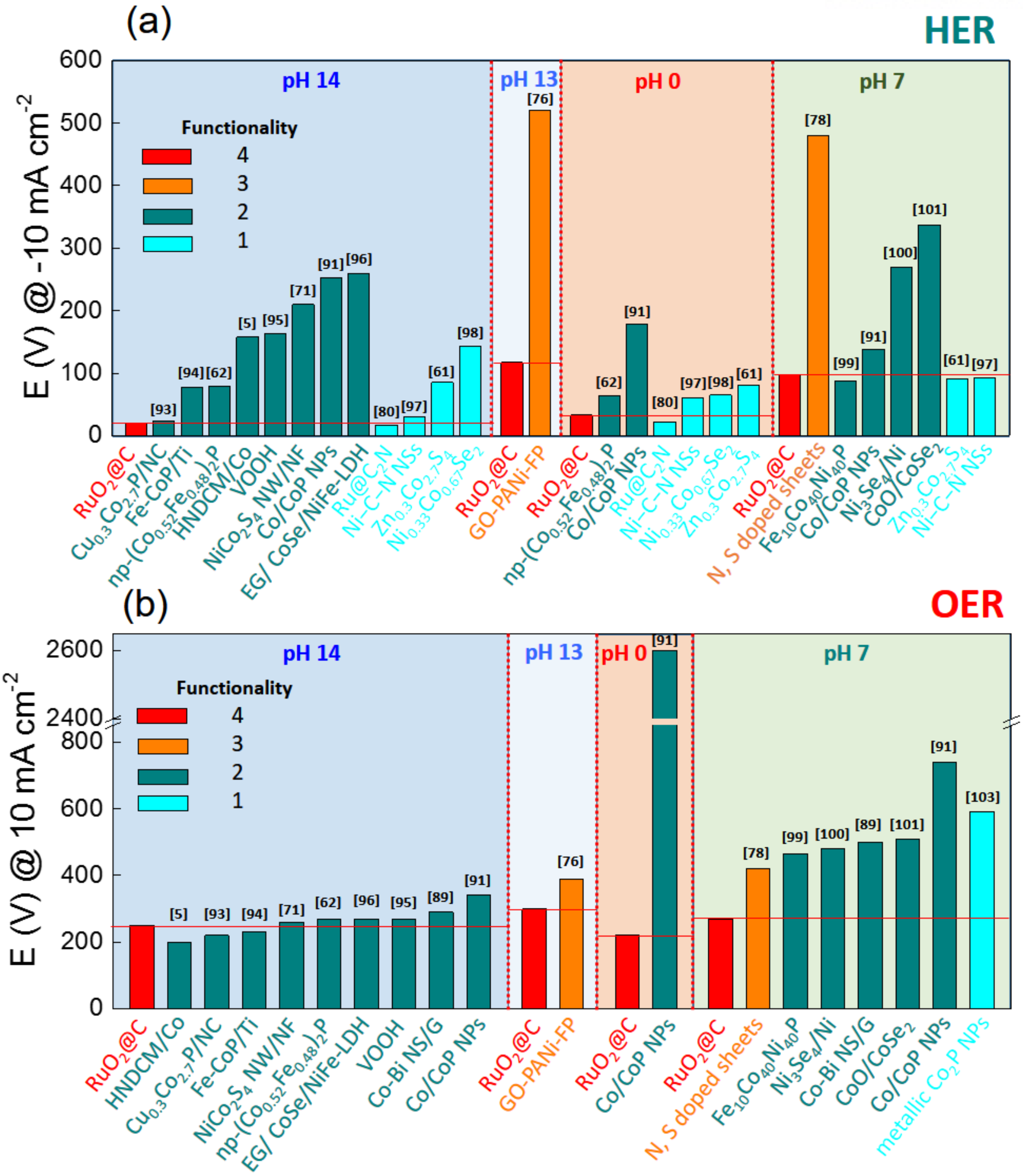

Fig 3.9. Over potentials of HER and OER at ± 10. Four different electrolytes were used: 1 N KOH at pH 14; 0.1 N KOH at pH 13; 1 N H_2SO_4 at pH 0; and 1 N phosphate buffer solution (PBS) at pH 7. HER (**a**) and OER (**b**) over potentials of this work in comparison with reported multifunctional catalysts.

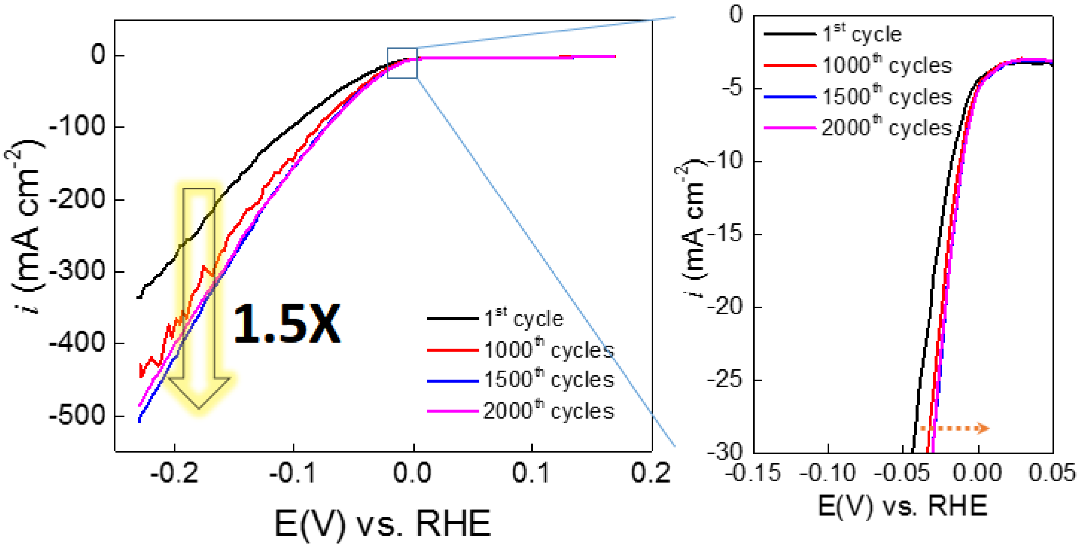

Figure 3.10. HER Durability test of *0.27*-RuO$_2$@C. Catalysts were polarized repeatedly from 0.2 V_{RHE} to -0.2 V_{RHE} in 1 N KOH (aq). The potential was swept in 50 mV s^{-1}. Polarization curves at the 1st, 1000th, 1500th and 2000th cycle were selectively demonstrated.

Table 3.1. HER overpotentials and Tafel slopes of multi-functional catalysts in basic, acid and neutral electrolytes.

Basic media

catalysts	functionality	electrolyte	current (mA cm^{-2})	Overpotential (mV)	Tafel slope (mV dec^{-1})	References
RuO_2@C	4	1 M KOH	-10 / -20	20 / 35	46	This work
		0.1 M KOH	-10	117	137	
GO-PANi-FP	3	0.1 M KOH	-10	520	141	[76]
$Cu_{0.3}Co_{2.7}P$/NC	2	1 M KOH	-10	23	122	[93]
Fe-CoP/Ti	2	1 M KOH	-10	78	75	[94]
np-$(Co_{0.52}Fe_{0.48})_2P$	2	1 M KOH	-10	79	40	[62]
HNDCM/Co	2	1 M KOH	-10	158	93.4	[5]
VOOH	2	1 M KOH	-10	164	104	[95]
$NiCo_2S_4$ NW/NF	2	1 M KOH	-10	210	58.9	[71]
Co/CoP Nanoparticles	2	1 M KOH	-10	253	73.8	[91]
EG/ $Co_{0.85}Se$/NiFe-LDH	2	1 M KOH	-10	260	160	[96]
Ru@C_2N	1	1 M KOH	-10 / -20	17 / 35.5	38	[80]
Ni−C−N Nanosheets	1	1 M KOH	-10	30.8	40	[97]
$Zn_{0.3}Co_{2.7}S_4$	1	1 M KOH	-10 / -100	85 / 136	-	[61]
$Ni_{0.33}Co_{0.67}Se_2$	1	1 M KOH	-10	143	60	[98]

Acidic media

Catalysts	functionality	electrolyte	current (mA cm^{-2})	Overpotential (mV)	Tafel slope (mV dec^{-1})	References
RuO_2@C	4	0.5 M H_2SO_4	-10 / -20	33 / 52	53	This work
np-$(Co_{0.52}Fe_{0.48})_2P$	2	0.5 M H_2SO_4	-10	64	45	[62]
Co/CoP Nanoparticles	2	0.5 M H_2SO_4	-10	178	-	[91]
Ru@C_2N	1	0.5 M H_2SO_4	-10 / -20	22 / 34.8	30	[80]
Ni−C−N Nanosheets	1	0.5 M H_2SO_4	-10	60.9	32	[97]
$Ni_{0.33}Co_{0.67}Se_2$	1	0.5 M H_2SO_4	-10	65	35	[98]
$Zn_{0.3}Co_{2.7}S_4$	1	0.5 M H_2SO_4	-10	80	47.5	[61]

Neutral media

Catalysts	functionality	electrolyte	current (mA cm^{-2})	Overpotential (mV)	Tafel slope (mV dec^{-1})	References
RuO_2@C	4	1 M PBS	-10	98	97	This work
N, S co-doped graphitic sheets	3	1 M PBS	-10	480	-	[78]
$Fe_{10}Co_{40}Ni_{40}P$	2	1 M PBS	-10	88	62	[99]
Co/CoP Nanoparticles	2	1 M PBS	-10	138	-	[91]
Ni_3Se_4/Ni	2	PBS	-10	269	101	[100]
CoO/$CoSe_2$	2	0.5 M PBS	-10	337	131	[92]
$Zn_{0.3}Co_{2.7}S_4$	1	0.1 M PBS	-10	90	-	[61]
Ni−C−N Nanosheets	1	1 M PBS	-10	92.1	38	[97]

3.3.3 OER

RuO_2 has been reported as one of the best OER electrocatalysts in acid as well as in base electrolytes. [6] In Pourbaix diagram of Ru, dissolved phases as RuO_4^-, RuO_4^{2-} and $HRuO_5^-$ are thermodynamically favored at high pH and over 1.1 V_{RHE}. [101] However, it was reported that ruthenium oxide generated after the first anodic and cathodic potential sweep of Ru metal showed stable OER current during the following repeated scans. [48] *h*-RuO_2 (not shown) was most superior in terms of the onset potential, which was followed by *0.27*-RuO_2@C and then *ah*-RuO_2 for all pH conditions (**Figure 3.6b**, **d**, **f** and **Figure 3.7b**, **d**). However, the totally hydrated form was unstable in alkaline media so that no OER current was obtained after the initial anodic scan. The *0.27*-RuO_2@C was superior to any other catalysts including Pt/C and even Ir/C (known as one of the best OER catalysts) for OER over the full range of pH. Tafel slopes (***b***) of *0.*27-RuO_2@C were more similar to those of Ir/C rather than those of *ah*-RuO_2 and Pt/C (**Figure 3.8b**, **d**, **f**). OER in neutral media began to be reported very recently even if activities in neutral is much lower than those in acid and base. Low ionic conductivities of neutral media are partially responsible for large overpotentials of electrochemical reactions. In spite of the demerits, the neutral media have eco-friendly and economic merits over non-neutral media. [102] *0.27*-RuO_2@C showed incomparably low overpotentials than recently reported catalysts in neutral media (**Figure 3.11**). [78, 102]

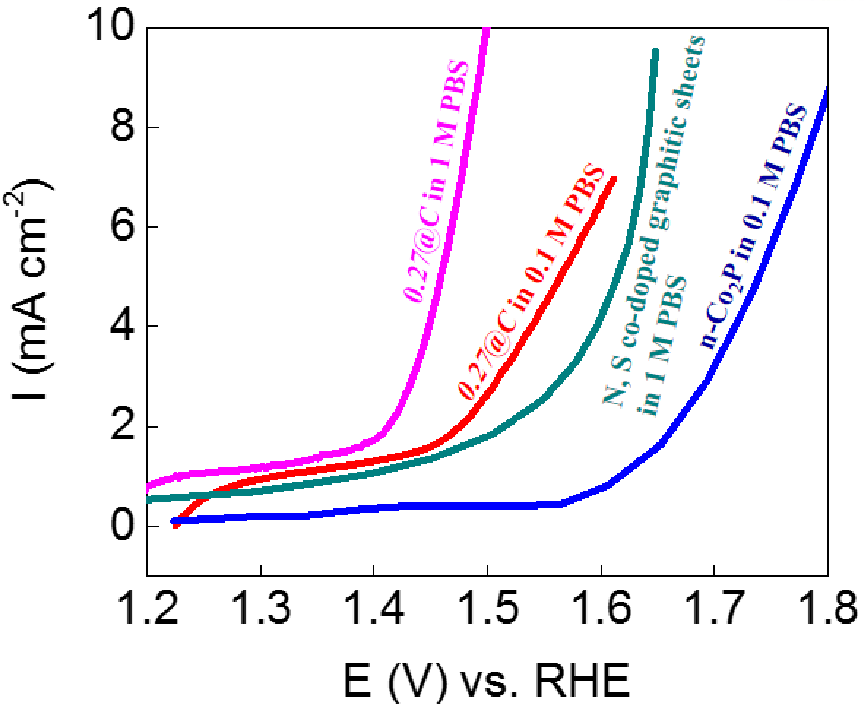

Figure 3.11. In-neutral-media OER polarization comparison of *0.27*-RuO$_2$@C with reported works. Phosphate buffer solution (PBS) at pH 7 was used for all electrodes. Data for polarization curves of N, S co-doped graphitic sheets and n-Co$_2$P were read respectively from ref. [78, 102]

The OER electrocatalytic superiority of *0.27*-RuO$_2$@C was considered to come partly from its appropriate hydration degree. The hydrous form was highly OER-active but unstable while the anhydrous form was stable but inferior OER-kinetically. Electrically conductive environment by carbon matrix (@C) surrounding RuO$_2$ would be helpful in improving kinetics. It was difficult to find catalysts showing higher OER electroactivities than that of *0.27*-RuO$_2$@C in acidic and neutral media in literature (**Figure 3.6** and **Table 3.2**). A single work [91] (Co/CoP) was found as multi-functional catalysts in all pH, showing the OER overpotential at 340 mV at 10 mA cm^{-2} in alkaline media, 570 mV at 1.3 mA cm^{-2} in acid and 570 mV at 2.64 mA cm^{-2} in neutral media. Much smaller overpotentials were obtained by *0.27*-RuO$_2$@C: 250 mV at 10 mA cm^{-2} in the same alkaline media, 170 mV at 1.3 mA cm^{-2} in the same acid and ~220 mV at 2.77 mA cm^{-2} in the same neutral media.

Table 3.2. OER overpotentials and Tafel slopes of multi-functional catalysts in basic, acid and neutral electrolytes.

Basic media

catalysts	functionality	electrolyte	current (mA cm^{-2})	Overpotential (mV)	Tafel slope (mV dec^{-1})	References
RuO_2@C	4	1 M KOH	10 / 20	250 / 270	68	**This work**
		0.1 M KOH	10	300	116	
GO-PANi-FP	3	0.1 M KOH	10	390	136	[76]
HNDCM/Co	2	1 M KOH	10	199	66.8	[5]
$Cu_{0.3}Co_{2.7}P$/NC	2	1 M KOH	10	220	44	[93]
Fe-CoP/Ti	2	1 M KOH	10	230	67	[94]
$NiCo_2S_4$ NW/NF	2	1 M KOH	10	260	40.1	[71]
np-$(Co_{0.52}Fe_{0.48})_2P$	2	1 M KOH	10	270	30	[62]
EG/ $Co_{0.85}Se$/NiFe-LDH	2	1 M KOH	10	270	57	[96]
VOOH	2	1 M KOH	10	270	68	[95]
Co-Bi NS/G	2	1 M KOH	10	290	53	[89]
Co/CoP Nanoparticles	2	1 M KOH	10	340	79.5	[91]

Acidic media

Catalysts	functionality	electrolyte	current (mA cm^{-2})	Overpotential (mV)	Tafel slope (mV dec^{-1})	References
RuO_2@C	4	0.5 M H_2SO_4	10 / 20	220 / 239	66	**This work**
Co/CoP Nanoparticles	2	0.5 M H_2SO_4	1.3 (10)	570 (2600)	-	[91]

Neutral media

Catalysts	functionality	electrolyte	current (mA cm^{-2})	Overpotential (mV)	Tafel slope (mV dec^{-1})	References
RuO_2@C	4	1 M PBS	10	269	116	This work
		0.1 M PBS	7	380	-	
N, S co-doped graphitic sheets	3	1 M PBS	10	420	-	[78]
$Fe_{10}Co_{40}Ni_{40}P$	2	1 M PBS	10	466	246	[99]
Ni_3Se_4/Ni	2	PBS	10	480	116	[100]
Co-Bi NS/G	2	1 M PBS	10	500	160	[89]
CoO/$CoSe_2$	2	0.5 M PBS	10	510	137	[92]
Co/CoP Nanoparticles	2	1 M PBS	2.64 (10)	570 (740)	-	[91]
metallic Co_2P nanoparticles	1	0.1 M PBS	10 (7)	592 (540)	134	[102]

3.3.4 Water splitting

Water electrolysis performances were expected from the HER and OER polarizations (**Figure 3.6**). The overpotential gap between HER and OER required to extract 10 or 100 mA cm^{-2} ($\Delta E_{\pm 10}$ and $\Delta E_{\pm 100}$) was estimated as a measure of the performances (**Figure 3.12a** and **Figure 3.13**). The smallest overpotential gaps $\Delta E_{\pm 10}$ were obtained in alkaline media by *0.27*-RuO_2@C, which is superior to that of a pair of Pt for HER and Ir for OER: $\Delta E_{\pm 10}$ ($\Delta E_{\pm 100}$) = 1.50 (1.69) V for *0.27*-RuO_2@C||*0.27*-RuO_2@C versus 1.56 (1.79) V for Pt/C||Ir/C (**Figure 3.6a** and **b**). The electrolysis performance of *0.27*-RuO_2@C is surprising when considering that Pt/C||Ir/C is the best combination of catalysts that have ever been reported and the value of $\Delta E_{\pm 10}$ of *0.27*-RuO_2@C is very close to the theoretical potential gap at 1.23 V for water splitting. When compared with reported symmetric electrolyzers based on a single catalyst, the *0.27*-RuO_2@C showed topmost level performances (**Figure 3.12b**; **Table 3.3**). [62, 74, 96, 103] The polarization curve of our cell (solid line in pink) was well matched with the difference between OER and ORR half-cell polarization data (circles in pink).

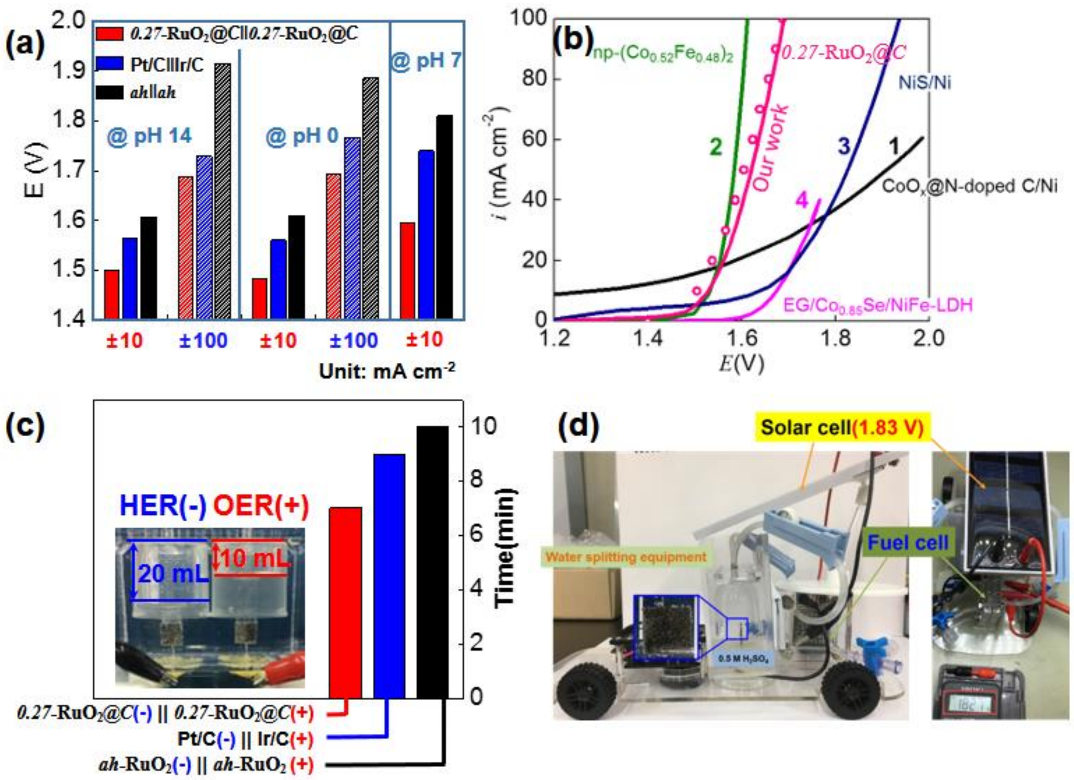

Figure 3.12. Symmetric water electrolyzer. The catalyst was loaded on nickel electrodes in 1 cm^2. (**a**) Overpotential gap between HER and OER ($\Delta E_{OER\text{-}HER}$) at 10 or 100 mA cm^{-2}. (**b**) Polarization curves of this work in comparison with reported symmetric electrolyzers. 1 = ref. 74; 2 = ref. 62; 3 = ref. 103; 4 = ref. 96. (**c**) Electrolysis time required to obtain 20 ml H_2. Inset photo = the symmetric electrolyzer. (**d**) A miniaturized fuel cell car driven by hydrogen generated by the *0.27*-RuO_2@C||*0.27*-RuO_2@C electrolyzer powered by a solar cell at 1.83 V. Electrolyte = 1 N KOH for **b** and **c** and 1 N H_2SO_4 for **d**.

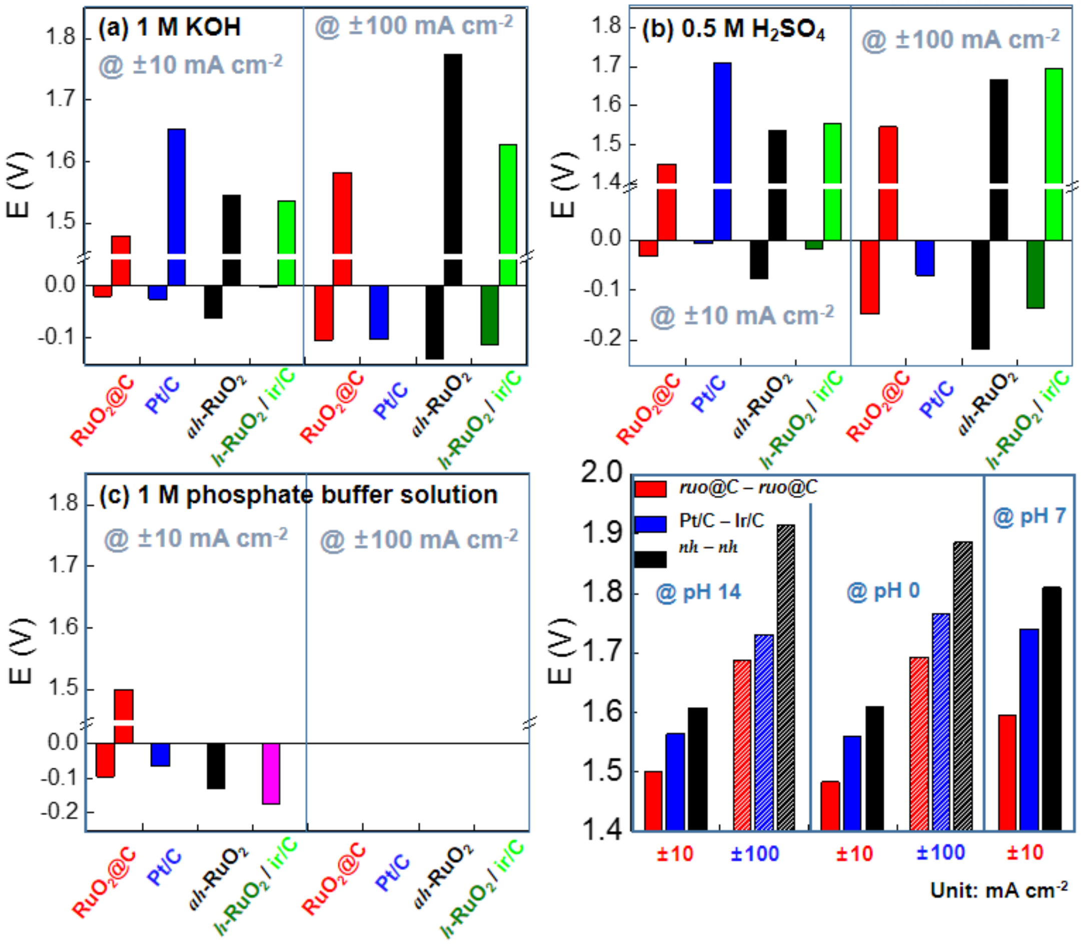

Figure 3.13. Over potentials of HER and OER at ± 10 and ± 100 mA cm^{-2}. Three different electrolytes were used: (**a**) 1 N KOH at pH 14 ; (**b**) 1 N H_2SO_4 at pH 0; (**c**) and 1 N phosphate buffer solution (PBS) at pH 7. (**d**) Overpotential gap between HER and OER ($\Delta E_{OER\text{-}HER}$) at 10 or 100 mA cm^{-2}. 20 wt. % carbon black was used for ruthenium-oxide-based catalysts. ***h*** = *h*-RuO_2; ***ah*** = *ah*-RuO_2; ***0.27@C*** = *0.27*-RuO_2@C.

Table 3.3. Working potentials and operation times of symmetric water electrolyzers.

catalysts	functionality	electrolyte	current density (mA cm^{-2})	Potential (V)	Operating time (h)	References
RuO_2@C	4	1 M KOH	10 / 20	1.51/1.56	110	this work
Co/CoP	2	1 M KOH	10	1.45	11	[91]
NiFe LDH-NS@DG10	2	1 M KOH	20	1.50	-	[104]
Cu@CoSx/CF	2	1 M KOH	10	1.50	200	[105]
np-$(Co_{0.52}Fe_{0.48})_2P$	2	1 M KOH	10	1.53	50	[62]
Fe-CoP/Ti	2	1 M KOH	10	1.60	40	[94]
Ni@NC-800	2	1 M KOH	10	1.60	50	[106]
Co9S8@NOSC-900	2	1 M KOH	10 / 20	1.60/1.74	10	[107]
EG/ $Co_{0.85}Se$/NiFe-LDH	2	1 M KOH	20	1.71	10	[96]
VOOH	2	1 M KOH	10	1.62	50	[95]
$NiCo_2S_4$ NW/NF	2	1 M KOH	10	1.63	50	[71]
$Cu_{0.3}Co_{2.7}P$/NC	2	1 M KOH	10	1.65	50	[93]

Water was electrolyzed into oxygen and hydrogen in electrolyzers with alkaline media at 3 V by two 1.5 V commercially available AA batteries in series (inset of **Figure 3.12c**; Water was split even by one 1.5 V AA batteries as shown in **Figure 3.14a**). Hydrogen and oxygen gases were generated vigorously (**Figure 3.14a, b**) at the expected stoichiometric ratio (H_2:O_2 = 2:1) for all tested pairs of catalysts. The electrolysis time to obtain 20 ml H_2 was shortest in the *0.27*-RuO_2@C||*0.27*-RuO_2@C electrolyzer (**Figure 3.12c**). Water splitting was very stable in the presence of *0.27*-RuO_2@C for >110 h without any obvious voltage changes at 10 and 20 mA cm^{-2} in 1 N KOH (**Figure 3.15)**, confirming that *0.27*-RuO_2@C electrolyzed water into hydrogen and oxygen without any side reactions for long-term operations.

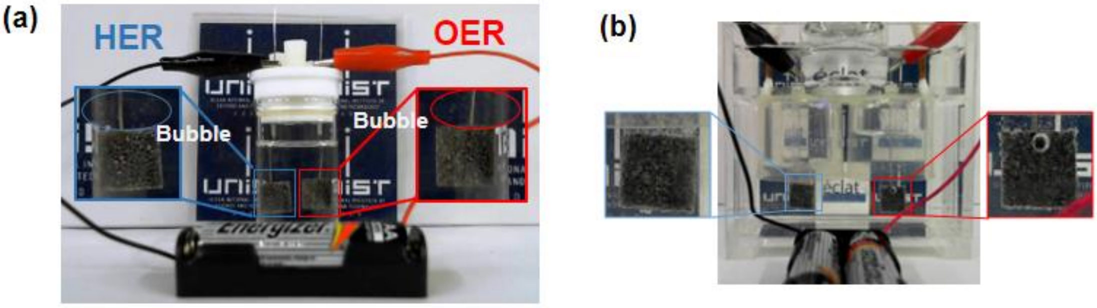

Figure 3.14. Photograph of water splitting cells connected with commercial batteries. *0.27*-RuO_2@C loaded Ni foams used in 1 cm^2 as anode and cathode at 1 N KOH electrolyte. Electrolyzers connected with one (a) and two (b) 1.5 V commercial AA batteries in series

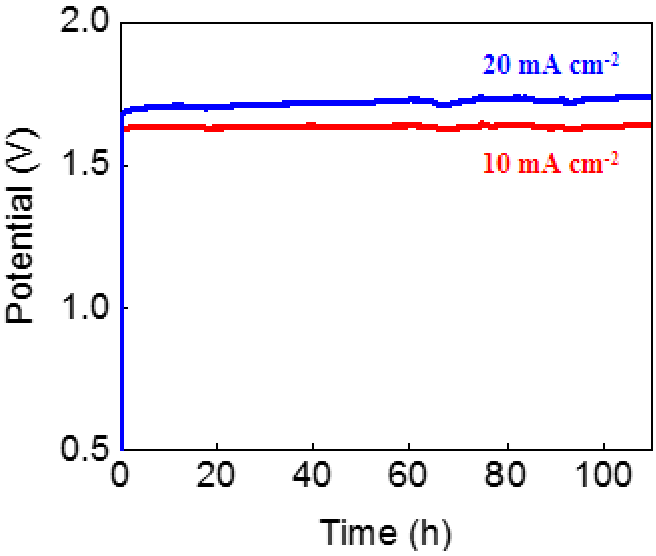

Figure 3.15. Stability test of water splitting in 1 N KOH by a beaker-type water electrolyzer. *0.27*-RuO_2@C-loaded Ni foams in 1 cm^2 were used as both electrodes. Small potential fluctuation was caused by atmospheric temperature change (e.g. day and night). Internal resistances (iR) were not corrected.

Following the successful operation of the symmetric electrolyzers in beaker-type configurations, anion exchange membrane water electrolyzers (AEMWE) were constructed for confirming more practical operations. *0.27*-RuO_2@C were used for both electrodes in 0.5 N KOH at room temperature (**Figure 3.16a**). The onset potential of water splitting was estimated at ~1.4 V on a potential sweep (**Figure 3.16b**), the value of which coincided with that of the beaker-type symmetric electrolyzers (**Figure 3.12b**). The polarization curve of AEMWE approximated that of the beaker-type electrolyzer. Electroactivities of *0.27*-RuO_2@C were significantly improved during the initial 4 h period on the potentiostatic operation at 1.6 V, showing a current increase from 16 mA cm^{-2} to 40 mA cm^{-2} (**Figure 3.16c**). Then, the current was saturated up to 8 h. The initial electrochemical aging was beneficial in kinetics, which was confirmed by decrease in semi-circle size of impedance spectra (**Figure 3.16d**). Therefore, the AEMWE was superior to the beaker-type cells even if more dilute electrolyte was used (0.5 N KOH for AEMWE versus 1.0 N KOH for beaker-type).

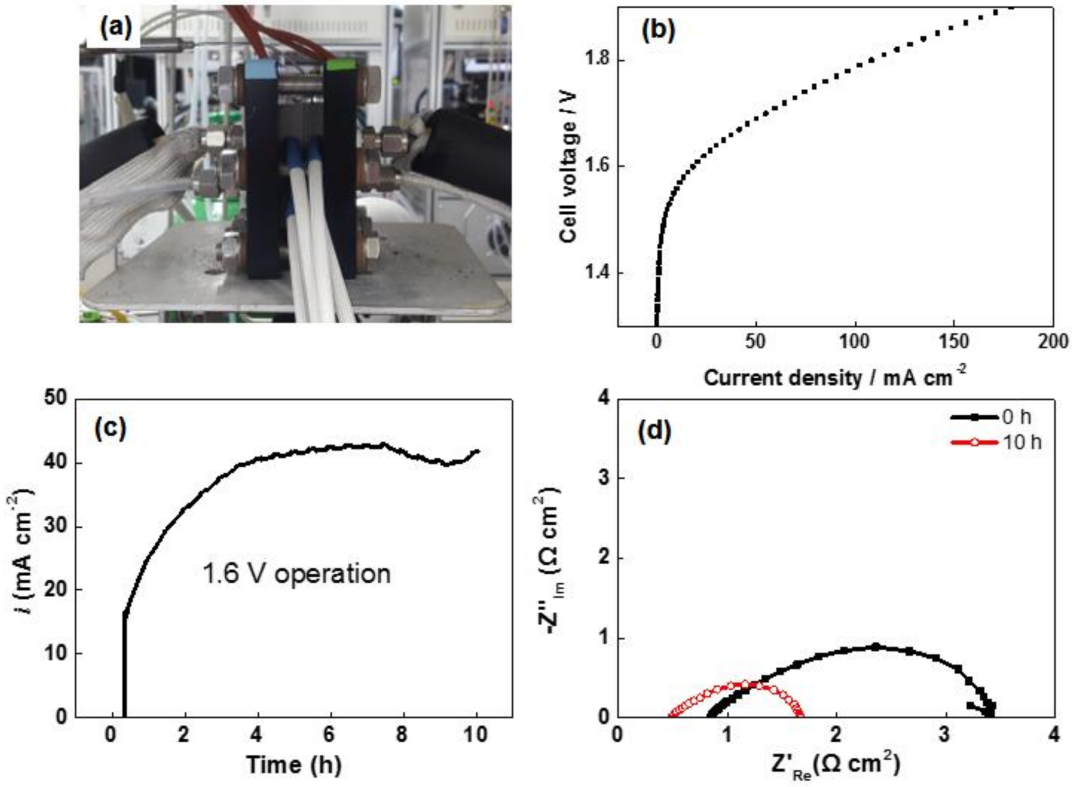

Figure 3.16. Alkaline anion exchange membrane water electrolyzers (AEMWE). 1.0 mg cm^{-2} of *0.27*-RuO_2@C was loaded on both electrodes. 0.5 N KOH (aq) was used as electrolyte. Cells were operated at room temperature. (**a**) AEMWE. (**b**) Potentiodynamic operation on a potential sweep at 20 mV s^{-1}. (**c**) Potentiostatic operation at 1.6 V for 10 h. (**d**) Electrochemical impedance spectra obtained before and after the previous operation for 10 h. Frequencies varied from 30 kHz to 30 mHz.

In addition to alkaline electrolysis, acid electrolysis was investigated at 1 N H_2SO_4 at pH 0. HER overpotentials in acid were similar to or a little bit larger than those in alkaline (**Figure 3.6c** and **Figure 3.7c**). Even if *h*-RuO_2 was superior to *0.27*-RuO_2@C in HER, it was very unstable in OER. The best OER polarization was obtained by *0.27*-RuO_2@C while the HER of *0.27*-RuO_2@C was inferior to that of Pt/C (**Figure 3.6d** and **Figure 3.7d**). The resultant overpotential gaps were similar to those obtained in the alkaline media: $\Delta E_{\pm 10}$ ($\Delta E_{\pm 100}$) = 1.48 (1.69) V for *0.27*-RuO_2@C||*0.27*-RuO_2@C versus 1.56 (1.77) V for Pt/C||Ir/C (**Figure 3.12a)**. Real operation of the symmetric electrolyzer based on *0.27*-RuO_2@C as catalysts of both electrodes in acid was confirmed by demonstrating that a miniaturized fuel cell car was successfully driven by using hydrogen generated by our electrolyzer powered by a silicon solar cell at 1.83 V (**Figure 3.12d**).

Recently, OER electrocatalysts working in neutral media have been reported. (**Figure 3.9, Table 3.1** and **3.2**). [89, 102, 108, 109] Unlike in acid and alkaline media, large overpotentials were required to extract meaningful currents of electrolysis. In phosphate buffer solution (PBS) at pH 7 (**Figure 3.6e** and **f**), the *0.27*-RuO_2@C was uncompetitive with that of Pt/C in HER. However, its OER superiority was more prominent over other catalysts in the neutral media than in other non-neutral media. The OER currents at 10 mA cm^{-2} were read only for the *0.27*-RuO_2@C when the potential was anodically scanned up to 1.6 V_{RHE}. The $\Delta E_{\pm 10}$ of *0.27*-RuO_2@C||*0.27*-RuO_2@C was estimated at 1.59 V, which is similar to those of acid and alkaline media of the same catalysts and much smaller than that of Pt/C||Ir/C at 1.74 V. The OER superiority of the *0.27*-RuO_2@C in neutral media was confirmed by the comparison with other works (**Figure 3.11, Figure 3.9.** and **Table 3.2**).

3.3.5 Tetra-functionality: ORR & HOR in addition to HER & OER

Oxygen reduction reaction (ORR) and hydrogen oxidation reaction (HOR) are the basic principle reactions for hydrogen fuel cells. In hydrogen economy, the fuel cells generate electricity by using hydrogen generated by water electrolyzers. The ORR and HOR is the reversed reactions of OER and HER, respectively. In addition to its OER and HER activities, the ruthenium oxide catalysts were investigated in terms of ORR and HOR. Our final goal is to develop a single catalyst for hydrogen economy. Reversible operation between fuel cells and electrolyzers would be possible with the single tetra-functional catalyst. In this work, the feasibility of *0.27*-RuO_2@C as ORR and HOR catalysts was tested.

The ORR electroactivity of RuO_2 has been rarely reported while its OER activity has been widely investigated. Poor electroactivities characterized by low ORR currents and high overpotentials were reported with RuO_2. [45, 46, 110] As an example, the potential at a half of the limiting current ($E_{2/L}$ at $i_L/2$) was +0.56 V_{RHE} at -1.2 mA cm^{-2} (cf. +0.9 V_{RHE} at -3 mA cm^{-2} for Pt/C). [45] The high overpotential indicates very sluggish ORR kinetics on RuO_2. More seriously, electron transfer number (n) was estimated at ~2 (4 is preferred for n; discussed below). In our previous work,[90] interestingly, much higher ORR electroactivities in alkaline media were obtained even from *ah*-RuO_2 as the control (**Figure 3.17**).

When compared with *h*-RuO_2 and *ah*-RuO_2, our *0.27*-RuO_2@C showed the merits of both forms of RuO_2. In the conductive environments achieved by 20 wt. % carbon black, the anhydrous form (*ah*-RuO_2) was favored in terms of the onset potential in ORR polarization (**Figure 3.17b**). On the other hand, the hydrous form (*h*-RuO_2) was favored in terms of the number of electron transfer (n) especially at low overpotentials. The thermal treatment at 400 °C (*0.08*-RuO_2 in **Figure 3.17**) improved the high overpotential of *h*-RuO_2, shifting the onset potential to that of *ah*-RuO_2.

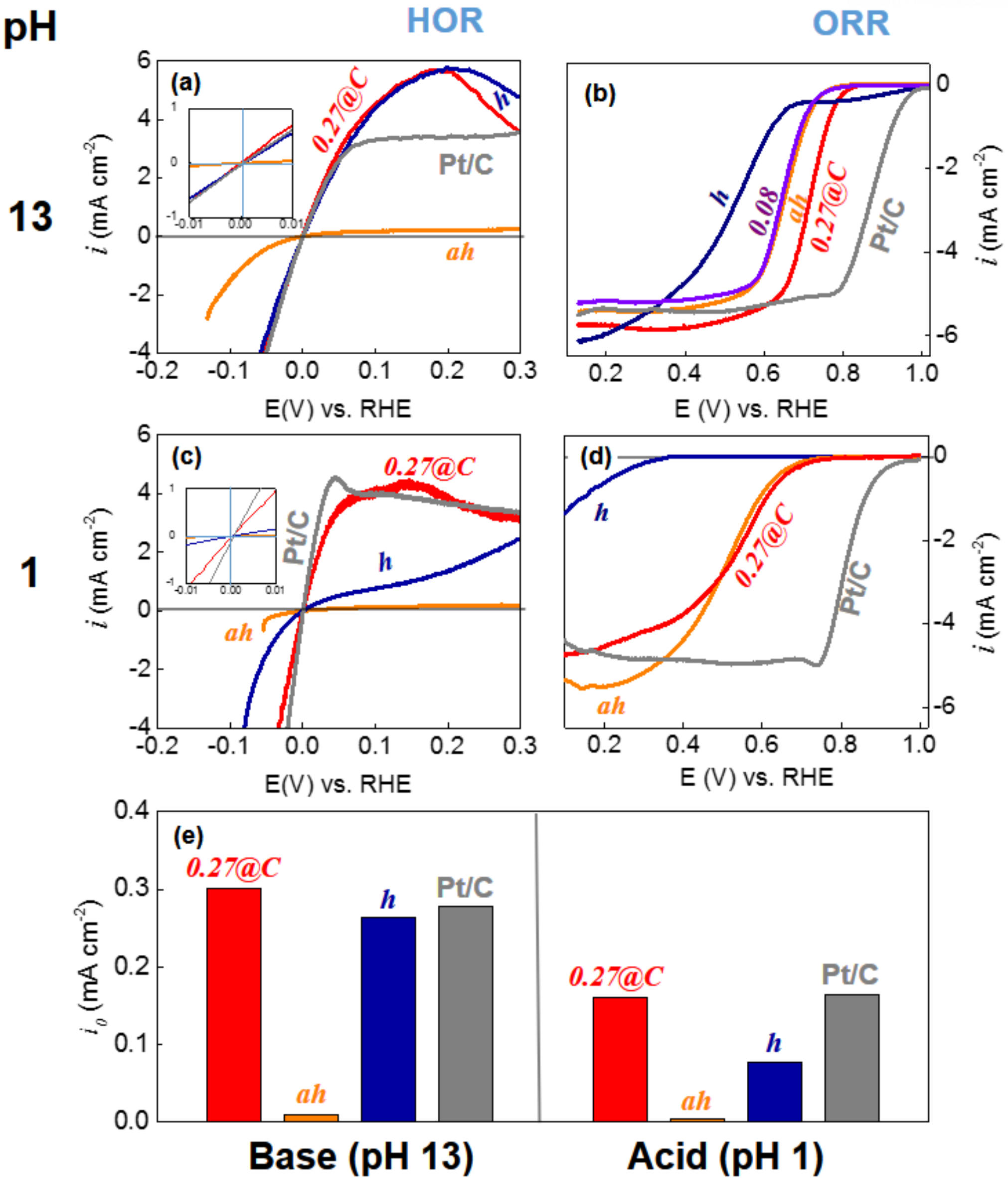

Figure 3.17. HOR and ORR polarization. The plots in the left and right columns are for HOR and ORR, respectively. Two different electrolytes were used: 0.1 N KOH at pH 13 (**a** and **b**); 0.1 N $HClO_4$ at pH 1 (**c** and **d**). Rotating disk electrodes of glassy carbon in 0.1256 cm^2 were used at 1600 rpm. 20 wt. % carbon black was used for ruthenium-oxide-based catalysts. ***h*** = *h*-RuO_2; ***nh*** = *nh*-RuO_2; ***0.27@C*** = 0.27-RuO_2@C.

Following the investigation on ORR activity, the HOR electroactivity of *0.27*-RuO_2@C was confirmed. *h*-RuO_2 showed good HOR electroactivity comparable to Pt/C while *ah*-RuO_2 was not HOR-active in both acid and alkaline media (**Figure 3.17a** to **d**). Correspondingly, exchange currents (i_o) of HOR by *0.27*-RuO_2@C were estimated comparable to those of Pt/C in basic and acidic media (**Figure 3.17e**). In hydrogen-related reactions such as HER and HOR, hydrated form (*h*-RuO_2) was more active than its anhydrous counterpart (*ah*-RuO_2). Naser et al., insisted that multivalent $Ru(OH)_x$ surface species act as a metastable cyclic redox mediator system in the hydrogen evolution reaction. Namely, high activity of hydrogen evolution reaction may be due to switching proton between hydroxy ions and water molecules, when central metal ion is reduced from Ru(III) oxyspecies to Ru(I) oxyspecies gradually. And the mediator is returned to its initial state (Ru(III) oxyspecies) so that it makes the redox cycle. Hydrous RuO_2(or $Ru(OH)_x$) in our catalyst acts as a mediator, HER performances of RuO_2@C catalyst are more active than anhydrous RuO_2 catalyst. The surface functional groups of *h*-RuO_2 or $Ru(OH)_x$ are possibly redox-active so that they could work as a mediator in the hydrogen-related reactions. [111] However, it was difficult to say that its HOR activity in acidic media resulted only from the hydration benefit because totally hydrous RuO_2 did not show such a fast kinetics. The Pt-level HOR activities of *0.27*-RuO_2@C were higher than those of Ru/Ir alloy nanoparticles and Ru/C. [112]

3.4 Conclusions

A single electrocatalyst was presented, which was able to electrocatalyze four different electrochemical reactions related to hydrogen and oxygen. Partially hydrous ruthenium oxide (*0.27*-RuO_2@C) as the 4-in-1 catalyst showed incomparable OER activity and Pt-level HER/HOR activities with significantly improved ORR activity superior to pristine ruthenium oxide. Also, it should be emphasized that the catalyst kept its catalytic superiority over a full range of pH even including neutral media. We demonstrated the usefulness of the multifunctional catalyst by showing the successful operation of symmetric water electrolyzers and suggesting the possibility of regenerative fuel cells based on 4-in-1 catalysts.

Chapter 4. References

1. Cheng, F.; Chen, J. Chemical Society reviews 2012, 41, 2172.
2. Rahman, M. a.; Wang, X.; Wen, C. J. Electrochem. Soc. 2013, 160, A1759.
3. Girishkumar, G.; McCloskey, B.; Luntz, A. C.; Swanson, S.; Wilcke, W. J. Phys. Chem. Lett. 2010, 1, 2193.
4. Zeng, K.; Zhang, D. Prog. Energy Combust. Sci. 2010, 36, 307.
5. Wang, J.; Xu, F.; Jin, H.; Chen, Y.; Wang, Y. Adv. Mater. 2017, 29, 1605838.
6. Jiao, Y.; Zheng, Y.; Jaroniec, M.; Qiao, S. Z. Chem. Soc. Rev. 2015, 44, 2060.
7. Huang, Z. F.; Wang, J.; Peng, Y.; Jung, C. Y.; Fisher, A.; Wang, X. Adv. Energy Mater. 2017, 1700544, 1.
8. Shinozaki, K.; Zack, J. W.; Richards, R. M.; Pivovar, B. S.; Kocha, S. S. J. Electrochem. Soc. 2015, 162, F1144.
9. Scholz, J.; Risch, M.; Stoerzinger, K. A.; Wartner, G.; Shao-Horn, Y.; Jooss, C. J. Phys. Chem. C 2016, 120, 27746.
10. Liang, Y.; Wang, H.; Zhou, J.; Li, Y.; Wang, J.; Regier, T.; Dai, H. Journal of the American Chemical Society 2012, 134, 3517.
11. Yelena Gorlin, T. F. J. J. Am. Chem. Soc. 2010, 132, 13612.
12. Cao, R.; Lee, J.-S.; Liu, M.; Cho, J. Adv. Energy Mater. 2012, 2, 816.
13. Meier, J. C.; Galeano, C.; Katsounaros, I.; Witte, J.; Bongard, H. J.; Topalov, A. a.; Baldizzone, C.; Mezzavilla, S.; Schüth, F.; Mayrhofer, K. J. J. Beilstein Journal of Nanotechnology 2014, 5, 44.
14. Otani, M.; Sugino, O. Phys. Rev. B 2006, 73, 115407.
15. Nørskov, J. K.; Rossmeisl, J.; Logadottir, A.; Lindqvist, L.; Kitchin, J. R.; Bligaard, T.; Jónsson, H. J. Phys. Chem. B 2004, 108, 17886.
16. Man, I. C.; Su, H.-Y.; Calle-Vallejo, F.; Hansen, H. A.; Martínez, J. I.; Inoglu, N. G.; Kitchin, J.; Jaramillo, T. F.; Nørskov, J. K.; Rossmeisl, J. ChemCatChem 2011, 3, 1159.
17. Zheng, Y.; Jiao, Y.; Zhu, Y.; Li, L. H.; Han, Y.; Chen, Y.; Du, A.; Jaroniec, M.; Qiao, S. Z. Nat. Commun. 2014, 5, 3783.
18. Chen, Z.; Higgins, D.; Yu, A.; Zhang, L.; Zhang, J. Energy Environ. Sci. 2011, 4, 3167.
19. Varcoe, J. R.; Atanassov, P.; Dekel, D. R.; Herring, A. M.; Hickner, M. A.; Kohl, P. A.; Kucernak, A. R.; Mustain, W. E.; Nijmeijer, K.; Scott, K.; Xu, T.; Zhuang, L. Energy Environ. Sci. 2014, 7, 3135.
20. Rashid, M. M.; Mesfer, M. K. A.; Naseem, H.; Danish, M. International Journal of Engineering and Advanced Technology 2015, 2249.

21. Zhang, J.; Zhao, Z.; Xia, Z.; Dai, L. Nat. Nanotechnol. 2015, 10, 444.
22. Lee, J. S.; Kim, S. T.; Cao, R.; Choi, N. S.; Liu, M.; Lee, K. T.; Cho, J. Adv. Energy Mater. 2011, 1, 34.
23. Li, Y.; Dai, H. Chemical Society reviews 2014, 43, 5257.
24. Nie, Y.; Li, L.; Wei, Z. Chem. Soc. Rev. 2015, 44, 2168.
25. Cherevko, S.; Geiger, S.; Kasian, O.; Kulyk, N.; Grote, J.-P.; Savan, A.; Shrestha, B. R.; Merzlikin, S.; Breitbach, B.; Ludwig, A.; Mayrhofer, K. J. J. Catal. Today 2015, 262, 170.
26. Seo, E.; Lee, T.; Lee, K. T.; Song, H.-K.; Kim, B.-S. J. Mater. Chem. 2012, 22, 11598.
27. Zheng, J. P. J. Electrochem. Soc. 1995, 142, 2699.
28. Kim, I.-H.; Kim, K.-B. J. Electrochem. Soc. 2006, 153, A383.
29. Adeyemo, A.; Hunter, G.; Dutta, P. K. Sens. Actuators, B 2011, 152, 307.
30. Jahan, M.; Liu, Z.; Loh, K. P. Adv. Funct. Mater. 2013, 23, 5363.
31. Wu, G.; Johnston, C. M.; Mack, N. H.; Artyushkova, K.; Ferrandon, M.; Nelson, M.; Lezama-Pacheco, J. S.; Conradson, S. D.; More, K. L.; Myers, D. J.; Zelenay, P. J. Mater. Chem. 2011, 21, 11392.
32. Chung, D. Y.; Jun, S. W.; Yoon, G.; Kwon, S. G.; Shin, D. Y.; Seo, P.; Yoo, J. M.; Shin, H.; Chung, Y. H.; Kim, H.; Mun, B. S.; Lee, K. S.; Lee, N. S.; Yoo, S. J.; Lim, D. H.; Kang, K.; Sung, Y. E.; Hyeon, T. J. Am. Chem. Soc. 2015, 137, 15478.
33. Lee, S.; Cho, Y.; Song, H.-K.; Lee, K. T.; Cho, J. Angew. Chem. Int. Ed. 2012, 51, 8748.
34. Park, H.-S.; Kim, T.-H.; Lee, M.-H.; Song, H.-K. J. Mater. Chem. 2012, 22, 20305.
35. Kim, T.-H.; Park, H.-S.; Lee, M.-H.; Lee, S.-Y.; Song, H.-K. J. Power Sources 2012, 210, 1.
36. Kim, T.-H.; Song, H.-K. Electrochim. Acta 2013, 105, 47.
37. Leong, W. L.; Lee, P. S.; Lohani, A.; Lam, Y. M.; Chen, T.; Zhang, S.; Dodabalapur, A.; Mhaisalkar, S. G. Adv. Mater. 2008, 20, 2325.
38. Sun, Y.; Wu, J.; Tian, J.; Jin, C.; Yang, R. Electrochim. Acta 2015, 178, 806.
39. Park, S.; Ho, S.; Aruliah, S.; Weber, M.; Ward, C. J. Electrochem. Soc. 1986, 133, 1641.
40. Chen, Z.; Yu, A.; Higgins, D.; Li, H.; Wang, H.; Chen, Z. Nano Lett. 2012, 12, 1946.
41. Zhang, J.; Ma, J.; Zhang, L. L.; Guo, P.; Jiang, J.; Zhao, X. S. J. Phys. Chem. C 2010, 114, 13608.
42. Dmowski, W.; Egami, T.; Swider-Lyons, K. E.; Love, C. T.; Rolison, D. R. J. Phys. Chem. B 2002, 106, 12677.
43. Sugimoto, W.; Iwata, H.; Yokoshima, K.; Murakami, Y.; Takasu, Y. J. Phys. Chem. B 2005, 109, 7330.
44. McKeown, D. a.; Hagans, P. L.; Carette, L. P. L.; Russell, A. E.; Swider, K. E.; Rolison, D.

R. J. Phys. Chem. B 1999, 103, 4825.

45. Sunarso, J.; Glushenkov, a. M.; Torriero, a. a. J.; Howlett, P. C.; Chen, Y.; MacFarlane, D. R.; Forsyth, M. J. Electrochem. Soc. 2012, 160, H74.
46. Masa, J.; Xia, W.; Sinev, I.; Zhao, A.; Sun, Z.; Grützke, S.; Weide, P.; Muhler, M.; Schuhmann, W. Angew. Chem. Int. Ed. 2014, 53, 8508.
47. Jiang, H.; Yao, Y.; Zhu, Y.; Liu, Y.; Su, Y.; Yang, X.; Li, C. ACS Appl. Mater. Interfaces 2015, 7, 21511.
48. Kötz, R. J. Electrochem. Soc. 1983, 130, 825.
49. Pei, P.; Wang, K.; Ma, Z. Appl. Energy 2014, 128, 315.
50. Maass, S.; Finsterwalder, F.; Frank, G.; Hartmann, R.; Merten, C. J. Power Sources 2008, 176, 444.
51. Gallagher, K. G.; Darling, R. M.; Fuller, T. F. In Handbook of Fuel Cells; Vielstich, W.,Gasteiger, H. A.,Lamm, A.,Yokokawa, H., Eds.; John Wiley & Sons: 2010.
52. Lee, D. U.; Park, M. G.; Park, H. W.; Seo, M. H.; Wang, X. L.; Chen, Z. W. Chemsuschem 2015, 8, 3129.
53. Han, L.-N.; Lv, L.-B.; Zhu, Q.-C.; Wei, X.; Li, X.-H.; Chen, J.-S. J. Mater. Chem. A 2016, 4, 7841.
54. Du, G.; Liu, X.; Zong, Y.; Hor, T. S. A.; Yu, A.; Liu, Z. Nanoscale 2013, 5, 4657.
55. Chen, Z.; Yu, A. P.; Ahmed, R.; Wang, H. J.; Li, H.; Chen, Z. W. Electrochim. Acta 2012, 69, 295.
56. Wang, Z.; Xiao, S.; An, Y.; Long, X.; Zheng, X.; Lu, X.; Tong, Y.; Yang, S. ACS Appl. Mater. Interfaces 2016, 8, 13348.
57. Song, J.; Zhu, C.; Fu, S.; Song, Y.; Du, D.; Lin, Y. J. Mater. Chem. A 2016, 4, 4864.
58. Prabu, M.; Ramakrishnan, P.; Shanmugam, S. Electrochem. Commun. 2014, 41, 59.
59. Prabu, M.; Ketpang, K.; Shanmugam, S. Nanoscale 2014, 6, 3173.
60. Li, Y.; Gong, M.; Liang, Y.; Feng, J.; Kim, J.-E.; Wang, H.; Hong, G.; Zhang, B.; Dai, H. Nat. Commun. 2013, 4, 1805.
61. Huang, Z.-F.; Song, J.; Li, K.; Tahir, M.; Wang, Y.-T.; Pan, L.; Wang, L.; Zhang, X.; Zou, J.-J. J. Am. Chem. Soc. 2016, 138, 1359.
62. Tan, Y.; Wang, H.; Liu, P.; Shen, Y.; Cheng, C.; Hirata, A.; Fujita, T.; Tang, Z.; Chen, M. Energy Environ. Sci. 2016, 9, 2257.
63. Durst, J.; Siebel, A.; Simon, C.; Hasche, F.; Herranz, J.; Gasteiger, H. a. Energy & Environmental Science 2014, 7, 2255.
64. McCrory, C. C. L.; Jung, S.; Ferrer, I. M.; Chatman, S. M.; Peters, J. C.; Jaramillo, T. F. Journal of the American Chemical Society 2015, 137, 4347.

65. Jia, J.; Seitz, L. C.; Benck, J. D.; Huo, Y.; Chen, Y.; Ng, J. W. D.; Bilir, T.; Harris, J. S.; Jaramillo, T. F. Nature Communications 2016, 7, 13237.
66. Brian C. H. Steele, A. H. Nature 2001, 414, 345.
67. Desmond Ng, J. W.; Gorlin, Y.; Hatsukade, T.; Jaramillo, T. F. Advanced Energy Materials 2013, 3, 1545.
68. Jingshan, L.; Jeong-Hyeok, I.; Mayer, M. T.; Schreier, M.; Nazeeruddfn, M. K.; Nam-Gyu, P.; Tilley, S. D.; Hong Jin, F.; Gratzel, M. Science 2014, 345, 1593.
69. Tian, J.; Liu, Q.; Asiri, A. M.; Sun, X. J. Am. Chem. Soc. 2014, 136, 7587−7590.
70. Liu, D.; Lu, Q.; Luo, Y.; Sun, X.; Asiri, A. M. Nanoscale 2015, 7, 15122.
71. Sivanantham, A.; Ganesan, P.; Shanmugam, S. Adv. Funct. Mater. 2016, 26, 4661.
72. Yang, Y.; Fei, H.; Ruan, G.; Tour, J. M. Adv. Mater. 2015, 27, 3175.
73. Wang, H.; Lee, H.-W.; Deng, Y.; Lu, Z.; Hsu, P.-C.; Liu, Y.; Lin, D.; Cui, Y. Nat. Commun. 2015, 6, 7261.
74. Jin, H.; Wang, J.; Su, D.; Wei, Z.; Pang, Z.; Wang, Y. J. Am. Chem. Soc. 2015, 137, 2688.
75. Zhu, H.; Gu, L.; Yu, D.; Sun, Y.; Wan, M.; Zhang, M.; Wang, L.; Wang, L.; Wu, W.; Yao, J.; Du, M.; Guo, S. Energy Environ. Sci. 2017, 10, 321.
76. Zhang, J.; Dai, L. Angew. Chem. Int. Ed. 2016, 55, 13296.
77. Jia, Y.; Zhang, L.; Du, A.; Gao, G.; Chen, J.; Yan, X.; Brown, C. L.; Yao, X. Adv. Mater. 2016, 28, 9532.
78. Hu, C.; Dai, L. Adv. Mater. 2016, 29, 1604942.
79. Liu, X.; Liu, W.; Ko, M.; Park, M.; Kim, M. G.; Oh, P.; Chae, S.; Park, S.; Casimir, A.; Wu, G.; Cho, J. Adv. Funct. Mater. 2015, 25, 5799.
80. Mahmood, J.; Li, F.; Jung, S.-M.; Okyay, M. S.; Ahmad, I.; Kim, S.-J.; Park, N.; Jeong, H. Y.; Baek, J.-B. Nat. Nanotechnol. 2017, 1.
81. Zheng, Y.; Jiao, Y.; Zhu, Y.; Li, L. H.; Han, Y.; Chen, Y.; Jaroniec, M.; Qiao, S.-Z. Journal of the American Chemical Society 2016, 138, 16174.
82. Wang, J.; Cui, W.; Liu, Q.; Xing, Z.; Asiri, A. M.; Sun, X. Advanced Materials 2016, 28, 215.
83. Martindale, B. C. M.; Reisner, E. Advanced Energy Materials 2016, 6, 1502095.
84. Zou, X.; Huang, X.; Goswami, A.; Silva, R.; Sathe, B. R.; Mikmeková, E.; Asefa, T. Angew. Chem. 2014, 126, 4461.
85. Lyons, M. E. G.; Doyle, R. L.; Brandon, M. P. Physical Chemistry Chemical Physics 2011, 13, 21530.
86. Kwon, T.; Hwang, H.; Sa, Y. J.; Park, J.; Baik, H.; Joo, S. H.; Lee, K. Advanced Functional Materials 2017, 27, 1604688.

87. Reier, T.; Oezaslan, M.; Strasser, P. ACS Catalysis 2012, 2, 1765.

88. Elias, X.; Liu, Q.; Gimbert-Suriñach, C.; Matheu, R.; Mantilla-Perez, P.; Martinez-Otero, A.; Sala, X.; Martorell, J.; Llobet, A. ACS Catalysis 2016, 6, 3310.

89. Chen, P.; Xu, K.; Zhou, T.; Tong, Y.; Wu, J.; Cheng, H.; Lu, X.; Ding, H.; Wu, C.; Xie, Y. Angew. Chem. Int. Ed. 2016, 55, 2488.

90. Park, H.-S.; Seo, E.; Yang, J.; Lee, Y.; Kim, B.-S.; Song, H.-K. Scientific Reports 2017, 7, 7150.

91. Xue, Z.-H.; Su, H.; Yu, Q.-Y.; Zhang, B.; Wang, H.-H.; Li, X.-H.; Chen, J.-S. Adv. Energy Mater. 2017, 1602355.

92. Li, K.; Zhang, J.; Wu, R.; Yu, Y.; Zhang, B. Advanced Science 2016, 3, 1500426.

93. Song, J.; Zhu, C.; Xu, B. Z.; Fu, S.; Engelhard, M. H.; Ye, R.; Du, D.; Beckman, S. P.; Lin, Y. Adv. Energy Mater. 2017, 7, 1601555.

94. Tang, C.; Zhang, R.; Lu, W.; He, L.; Jiang, X.; Asiri, A. M.; Sun, X. Adv. Mater. 2017, 29, 1602441.

95. Shi, H.; Liang, H.; Ming, F.; Wang, Z. Angew. Chem. Int. Ed. 2017, 56, 573.

96. Hou, Y.; Lohe, M. R.; Zhang, J.; Liu, S.; Zhuang, X.; Feng, X. Energy Environ. Sci. 2016, 9, 478.

97. Yin, J.; Fan, Q.; Li, Y.; Cheng, F.; Zhou, P.; Xi, P.; Sun, S. J. Am. Chem. Soc. 2016, 138, 14546.

98. Xia, C.; Liang, H.; Zhu, J.; Schwingenschl??gl, U.; Alshareef, H. N. Adv. Energy Mater. 2017, 1602089.

99. Zhang, Z.; Hao, J.; Yang, W.; Tang, J. RSC Adv. 2016, 6, 9647.

100. Anantharaj, S.; Kennedy, J.; Kundu, S. ACS Appl. Mater. Interfaces 2017, 9, 8714.

101. Povar, I.; Spinu, O. J. Electrochem. Sci. Eng. 2016, 6, 145.

102. Xu, K.; Cheng, H.; Liu, L.; Lv, H.; Wu, X.; Wu, C.; Xie, Y. Nano Lett 2017, 17, 578.

103. Zhu, W.; Yue, X.; Zhang, W.; Yu, S.; Zhang, Y.; Wang, J.; Wang, J. Chem. Commun. 2016, 1, 3.

104. Jia, Y.; Zhang, L.; Gao, G.; Chen, H.; Wang, B.; Zhou, J.; Soo, M. T.; Hong, M.; Yan, X.; Qian, G.; Zou, J.; Du, A.; Yao, X. Adv. Mater. 2017, 29, 1700017.

105. Liu, Y.; Li, Q.; Si, R.; Li, G. D.; Li, W.; Liu, D. P.; Wang, D.; Sun, L.; Zhang, Y.; Zou, X. Adv. Mater. 2017, 29, 1606200.

106. Xu, Y.; Tu, W.; Zhang, B.; Yin, S.; Huang, Y.; Kraft, M.; Xu, R. Adv. Mater. 2017, 29, 1605957.

107. Huang, S.; Meng, Y.; He, S.; Goswami, A.; Wu, Q.; Li, J.; Tong, S.; Asefa, T.; Wu, M. Adv. Funct. Mater. 2017, 27, 1606585.

108. Liu, Y.; Xiao, C.; Lyu, M.; Lin, Y.; Cai, W.; Huang, P.; Tong, W.; Zou, Y.; Xie, Y. Angew. Chem. Int. Ed. 2015, 54, 11231.
109. Jin, K.; Park, J.; Lee, J.; Yang, K. D.; Pradhan, G. K.; Sim, U.; Jeong, D.; Jang, H. L.; Park, S.; Kim, D.; Sung, N.-E.; Kim, S. H.; Han, S.; Nam, K. T. Journal of the American Chemical Society 2014, 136, 7435.
110. Jiang, H.; Yao, Y.; Zhu, Y.; Liu, Y.; Su, Y.; Yang, X.; Li, C. ACS Appl. Mater. Interfaces 2015, 7, 21511.
111. Burke, L. D.; Naser, N. S. J. Appl. Electrochem. 2005, 35, 931.
112. Ohyama, J.; Kumada, D.; Satsuma, A. J. Mater. Chem. A 2016, 4, 15980.

Chapter 5. Acknowledgement

“하나님으로 시작하여라. 지식의 첫걸음은 하나님께 엎드리는 것이다. 어리석은 자들만이 지혜와 지식을 업신여긴다.” (잠언 1:7, 메시지 성경)

하나님, 감사합니다. 되돌아보면 우둔한 저의 지식과 능력을 의지하는 저를 일깨워 모든 지식의 근원 되신 하나님께 엎드리게 했던 시간이었음을 고백할 수밖에 없습니다. 저의 모든 발자취에 함께하시고 인도하신 당신이 있기에 지금의 제가 존재합니다.

7 년이라는 기나긴 시간 동안 함께 해준 송현곤 교수님과 eclat 멤버들에게 감사의 말을 전합니다. 그 어떤 연구실보다 편리한 환경을 만들어 주신 송현곤 지도교수님 감사합니다. 전공도 다른 저를 선택해주신 기대에 부응하지 못해 죄송합니다. 교수님께 배운 지식과 삶의 교훈은 사회에서 귀하게 쓰일 것이라 확신합니다. 가장 오랜 시간 동안 함께 하고 졸업 후에도 마음만은 함께 해줬던 태희 씨, 태희 씨가 아니었으면 군대보다도 힘들었던 이 시간을 버티지 못했을지도 모르겠습니다. 당신의 격려와 조언이 저의 버팀목이었습니다. 뒤늦게 랩에 합류했지만 같은 연구를 하면서 많은 의지가 되었던 주찬 씨, 앞으로의 서로의 길이 어떻게 될지는 모르겠지만 서로 힘이 되어가요. 언제나 따뜻함으로 다가와 많은 것들을 조언해 주신 김영수 박사님, 실험의 기초를 다지게 해 주신 명희 누나, 약간의 다툼으로 더욱더 가까워진 영훈 씨, 양반으로 기억되는 근기 형, 동기로 함께 입학했지만 저보다 많은 부분에서 선배의 삶을 살고 있는 정석이, 누구보다 어른스러웠던 지은이, 많은 이야기를 함께 나누지는 못해 아쉬웠던 Delimon 박사님, 그 외 함께 했던 eclat 멤버들에게도 감사의 마음을 전합니다. 여러분과 함께했던 즐거운 추억뿐 아니라 좋지 않았던 시간들도 저에게는 의미 있는 시간이었습니다.

유니스트에서 만났던 많은 분들은 제 삶의 자양분이자 재산입니다. 부족한 저의 심사위원이 되어 주시고 따끔한 충고와 격려를 아끼지 않으신 백종범 교수님, 주상훈 교수님, 김영식 교수님과 신경희 박사님께 고개 숙여 감사드립니다. 주신 가르침대로 더 노력하는 사람이 되도록 하겠습니다. 그리고 저와 함께 했던 많은 친구들과 선, 후배들에게도 감사의 말을 전합니다. 룸메이트로 함께하며 정들었던 인찬이, 예의 바르고

정이 많은 강민이, 누구보다 서로의 마음을 깊이 이해하고 함께 기뻐하고 슬퍼했던 지훈이, 마음이 따뜻한 한돈 씨, 입학과 졸업 동기 태효 씨, 함께 공동 연구를 했던 은용 씨와 주명이, 마지막까지 함께 하지 못해 못내 아쉬운 장훈 씨, 지친 삶의 비타민 같았던 성애순 차장님 외 네오사이언스 직원분들, 연구지원본부의 김영기 선생님을 비롯한 많은 선생님들께 감사합니다.

저의 영혼의 안식처였던 시민교회에 감사합니다. 복음의 진정한 의미를 깨닫도록 도와주신 최수혁 목사님과 박지혜 사모님, 덕분에 하나님 한 분 만으로 기뻐할 수 있는 이유를 깨닫게 되었습니다. 함께 사역했던 시민교회 목자들과 많은 구성원, 특히 김승태 목자에게 감사의 말을 전합니다. 여러분의 기도가 저에게는 힘과 능력이었습니다.

저의 무모한 선택과 도전에도 믿음으로 함께 해 주신 가족에게도 감사의 마음을 전합니다. 언제나 기도로 함께 해주시고 힘든 상황에서도 용기를 주신 어머니의 사랑 잊지 않겠습니다. 어머니께서 쏟으신 눈물이 지금의 저를 만들었습니다. 물질적, 정신적으로 함께 해준 누나들과 저의 든든한 정신적 지주이자 후원자였던 외삼촌 분들에게도 감사드립니다. 몸은 떨어져 있지만 항상 함께 한다는 것을 알게 해주시고 언제나 따스함으로 다가와 주신 일본 어머니 이치가와(市川) 상, 항상 기도로 함께 해주셔서 감사합니다. 그리고 어려운 상황에도 묵묵히 제 곁에서 저를 믿어주고 사랑과 용기를 주며 기도로 함께 했던 평생의 동역자 곽혜진에게도 감사와 사랑의 말을 전합니다.

미처 지면에 표현하지 못했던 많은 분들께도 감사의 인사를 드립니다. 되돌아보니 저의 공보다 주변의 도움으로 성장한 것임을, 많은 분들이 함께 해주지 않았다면 지금의 저는 없었음을 깨닫습니다. 많은 분들의 사랑과 그 무엇보다 크신 하나님의 사랑을 기억하며 그 사랑을 이제 제가 나눌 것을 약속합니다. 감사합니다.

CURRICULUM VITAE

Han-Saem Park

School of Energy and Chemical Engineering
Ulsan National Institute of Science
and Technology (UNIST)
UNIST-gil 50, Ulsan, Korea 44919
T) +82-52-271-2962
M) +82-10-8542-7061

E-mail: hanseam79@gmail.com

EDUCATION

Ph.D., Energy Engineering (02/2018)

Ulsan National Institute of Science and Technology (UNIST), Republic of Korea

"RuO_2 nanocluster as a 4-in-1 electrocatalyst for hydrogen and oxygen electrochemistry"

Prof. Hyun-Kon Song, Advisor

B.S., Mechanical Engineering (02/2010)

Kyungpook National University, Republic of Korea

Prof. Chang Hyun Sohn, Advisor

EXPERIENCE

- **Research Assistant (09/2012 - 08/2017)**
  Department of Energy Engineering, UNIST, Ulsan, Republic of Korea
- **Teaching Assistant (03/2011 - 08/2012)**
  Department of Energy Engineering, UNIST, Ulsan, Republic of Korea

PROFESSIONAL SKILLS

- **Electrochemistry**
  - Electrochemical impedance spectroscopy (EIS)
  - in situ electrochemical impedance spectroscopy (EIS)
  - Cyclic voltammetry, chronoamperometry, linear sweep voltammetry, galvanostatic

cycling
- Scanning electrochemical microscopy (SECM)
- Rotating ring disk electrode (RRDE)

- **Material Characterization**
  - Structural characterization technique: scanning electron microscope (SEM), transmission electron microscope (TEM)
  - Spectroscopic technique: UV/visible spectroscopy, Fourier transform infrared spectroscopy (FT-IR)
  - Brunauer–Emmett–Teller (BET)
  - Thermal analysis technique: thermal gravimetric analyzer (TGA), differential scanning calorimetry (DSC)
  - X-ray analysis: X-ray diffractometer (XRD)
  - Dilatometer

- **Cell fabrication**
  - LIB (Lithium Ion Battery) 2016/2032 coin-type cell
  - Zn-air and Li-O2 (non-aqueous and hybrid (non-aqueous/aqueous)) cell

AWARDS

- **Best Poster Award**

  Spring Meeting of the Korean Electrochemical Society, 2013

PUBLICATIONS

[1] **Han-Saem Park**, Juchan Yang, Yeongdae Lee, Byeong-Su Kim and Hyun-Kon Song*
Under revision
“RuO_2 nanocluster as a 4-in-1 electrocatalyst for hydrogen and oxygen electrochemistry”

[2] **Han-Saem Park**, Eunyong Seo, Juchan Yang, Yeongdae Lee, Byeong-Su Kim* and Hyun-Kon Song*
Scientific Reports 2017, 7, 7150
“Bifunctional hydrous RuO_2 nanocluster electrocatalyst embedded in carbon matrix for efficient and durable operation of rechargeable zinc–air batteries”

[3] Dong-Gyu Lee, Ohhun Gwon, **Han-Saem Park**, Su Hwan Kim, Juchan Yang, Sang Kyu Kwak, Guntae Kim* and Hyun-Kon Song*
Angewandte Chemie International Edition 2015, 54, 15730
"Conductivity-Dependent Completion of Oxygen Reduction on Oxide Catalysts"

[4] Ju-Myung Kim‡, **Han-Saem Park**‡, Jang-Hoon Park, Tae-Hee Kim, Hyun-Kon Song* and Sang-Young Lee*
ACS Applied Materials & Interface 2014, 6, 12789
"Conducting polymer-skinned electroactive materials of lithium ion batteries: Ready for mono-component electrodes without additional binders and conductive agents"
‡ Authors contributed equally

[5] Hyun Kuk Noh*, **Han-Saem Park**, Hu Young Jeong, Sang Uck Lee and Hyun-Kon Song*
Angewandte Chemie International Edition 2014, 53, 5059
"Doubling Capacity of Lithium Manganese Oxide Spinel via Flexible Skinny Graphitic Layer"

[6] Jieun Kim, **Han-Saem Park**, Tae-Hee Kim, Sung Yeol Kim and Hyun-Kon Song*
Physical Chemistry Chemical Physics 2014,16, 5295
"An inter-tangled network of redox-active and conducting polymers as a cathode for ultrafast rechargeable batteries"

[7] **Han-Saem Park**, Myeong-Hee Lee, Ryeo Yun Hwang, Ok-Kyung Park, Kiyoung Jo, Taemin Lee, Byeong-Su Kim* and Hyun-Kon Song*
Nano Energy 2014, 3, 1
"Kinetically enhanced pseudocapacitance of conducting polymer doped with reduced graphene oxide through a miscible electron transfer interface"

[8] **Han-Saem Park**, Seo-Jin Ko, Jeong-Seok Park, Jin Young Kim and Hyun-Kon Song*
Scientific Reports 2013, 3, 2454
"Redox-active charge carriers of conducting polymers as a tuner of conductivity and its potential window"

[9] Jeong-Seok Park, Myeong-Hee Lee, In-Yup Jeon, **Han-Saem Park**, Jong-Beom Baek* and Hyun-Kon Song*
ACS nano 2012, 6, 10770

"Edge-Exfoliated Graphites for Facile Kinetics of Delithiation"

[10] **Han-Saem Park**, Tae-Hee Kim, Myeong-Hee Lee and Hyun-Kon Song*
Journal of Materials Chemistry 2012, 22, 20305
"Catalytic carbonization of an uncarbonizable precursor by transition metals in olivine cathode materials of lithium ion batteries"

[11] Tae-Hee Kim, **Han-Saem Park**, Myeong-Hee Lee, Sang-Young Lee* and Hyun-Kon Song*
Journal of Power Sources 2012, 210, 1
"Restricted Growth of $LiMnPO_4$ Nanoparticles Evolved from a Precursor Seed"

CONFERENCE PRESENTATIONS

[1] **Han-Saem Park**, Juchan Yang and Hyun-Kon Song*
9th Asian Conference on Electrochemical Power Sources, Gyeongju, Korea (August 20~23, 2017).
"RuO_2 nanocluster as a 4-in-1 electrocatalyst for hydrogen and oxygen electrochemistry"

[2] **Han-Saem Park** and Hyun-kon Song*
18th Topical ISE meeting, Gwangju, Korea (March 8 - 11, 2016).
"Ruthenium oxide nanoparticles embedded in carbon matrix as a durable bifunctional catalyst for Zn-air batteries"

[3] **Han-Saem Park**, Seo-Jin Ko, Jin Young Kim, Hyun-Kon Song*
13th International Conference on Electrified Interfaces. Chateau Liblice, Czech Republic (June 30~ July 5, 2013).
"Widening the conductive potential windows of conducting polymers by solvent annealing"

[4] **Han-Saem Park**, Jeong-Seok Park, Hyun-Kon Song*
Spring Meeting of the Korean Electrochemical Society, Changwon, Korea (April 11~13, 2013).
"Widening the conductive potential windows of a conducting polymer by solvent annealing"
Selected Best Poster Awards

[5] **Han-Saem Park**, Myeong-Hee Lee, Guntae Kim, Jin Young Kim, Hyun-Kon Song*
XXI International Materials Research Congress (IMRC), Cancun, Mexico (August 12~17, 2012).
"Tuning the conductive potential windows of conducting polymers by solvent annealing"